Superoscillating Acoustic Apertures

Thesis submitted to the University of Nottingham for the degree of
Doctor of Philosophy, July 2025.

Monty Clark

14314851

Supervised by

Mark Fromhold
Keith Benedict
Tony Kent

Signature ____________________

Date ______ / ______ / ______

Abstract

This thesis is a summary of work conducted in the course of investigation of superoscillating acoustic aperture arrays. In it we show that superoscillating acoustic apertures arrays are possible, give conditions and new design techniques for the implementation of such aperture arrays; show that in isotropic conditions diffraction gratings can superoscillate, and show by counter-example that not all diffraction gratings superoscillate. Consecutively we demonstrate previous detection methods for superoscillations and where some of the issues with them arise, before proposing a new detection method for superoscillations based on work performed by Aharonov. This work shows the efficacy of the new method, retrieving a result that Aharonov superoscillations occur in roughly 0.3% of $50,000$ random fields and show the problem with windowing with Berry's method. In the conclusion we discuss possible uses for these new techniques of design and detection, as well as future work that could be performed, such as expanding the aperture geometry basis sets and optimising detection methods so that they can be more easily implemented in real world scenarios.

Acknowledgements

I would like to acknowledge the hard work, insightful feedback, and suffering of my proofreaders. Sarita Mizin; Christopher Morley; Alister Davis; and Nathalie Kreeft, thank you dearly.

I would also like to acknowledge the time, dedication and insight that my supervisors have given me. Keith, Tony and Mark, without your guidance, persistence and expertise, this project would not have been possible.

Stephen Powell, your clear and articulate criticism and feedback on my work was invaluable as a tool for improving my skills as a physicist. Thank you for the time you took to read and understand my work.

I would like to thank anyone who decides to read this thesis. Your time and interest are greatly appreciated, and I hope that you find the content of interest or utility.

Contents

Abstract **i**

Acknowledgements **ii**

List of Tables **v**

List of Figures **vi**

Abbreviations **xiii**

Chapter 1 Introduction **1**

1.1 Thesis Overview 2

1.2 Acoustics 3

1.3 Superoscillations 8

Chapter 2 Foundational Theory **15**

2.1 Experimental Set up 15

2.2 Acoustics 18

2.3 Superoscillations 20

2.4 Aharonov Superoscillations 31

Chapter 3 Apertures **39**

3.1 Slit Apertures 39

3.2 Superoscillations in Slit Apertures 45

3.3 Proof of Superoscillations in Diffraction Gratings 52

3.4 Designing Superoscillatory Arrays 60

Chapter 4 Results **66**

4.1 Results 66

4.2 Discussion 77

Chapter 5 Detection **80**

5.1 Previous Methods 80

5.2 Reproducing Berry 83

5.3 Analysis Methods 89

5.4 The Aharonov Transform 94

Chapter 6 Conclusions **102**

6.1 Design and Detection Results 102

6.2 Future Work 104

6.3 Conclusion 108

Appendices **112**

Bibliography **121**

List of Tables

List of Figures

1.1 Superposition of two waves to create a superoscillatory wave. It is shown that a part of the combined wave has a smaller wavelength than that of the smallest wavelength that constitutes it. 8

2.1 A graphic showing the experiment that is being considered in the theory for this thesis. It shows a incoming laser beam being spatially modulated by a gold shadow mask in the form of an annular design. The spatially modulated light then illuminates an opto-acoustic transducer, a GaAs/GaAsAl superlattice approximately $10\mu m$ thick, that generates coherent phonons of wavelength $\lambda_{mat} = 1\mu m$ that then propagate through a medium of GaAs $450\mu m$ thick. These phonons are then measured as a diffraction pattern by a rasterising probe beam that takes advantage of interferometry to measure the deformities in a 100nm polystyrene detector that was deposited on the reverse of the GaAs substrate using spin-coating technique 16

2.2 (a.)Illustrates the gold shadowmask created by Khouloud Sellami by optical lithography for a design based off Toraldo di Francia's designs [1] (b.) the measured strain field at the other side of the substrate. Here can be clearly seen a spot of FWHM $\approx 10\mu m$. This design is detailed in table 6.3 as EDD1. This figure was a part of a private communication from Kholoud Sellami and Tony Kent providing experimental feedback for the designs. 17

2.3 (a) A graph of $\cos(x)$, (b) A graph of $\cos(2x)$ and (c) A graph of $(\cos(x) - s)^2$ with $s = 0.5$ illustrated to demonstrate superoscillatory behaviour. The top two panels show the individual frequency components of the bottom panel. The black vertical lines occur at the first spatial period of each graph and are to aid in showing the superoscillatory region around 0. In (a) the smallest local spatial period is 2π, in (b) the smallest spatial period is π and in (c) the smallest spatial period is $2\arccos(s) = \frac{2}{3}\pi$. It can therefore both be seen and demonstrated that there is a superoscillatory region in panel (c) . . . 24

2.4 Energy Quotient plots with respect to (a) the superoscillating variable s and (b) the superoscillating frequency f. Plot (b) has an origin at $f = 2$ as below this value it would not correspond to valid values of s and as such there is a divergence beyond $f = 2$ 28

2.5 A plot of $f_{\frac{\sqrt{2}}{2}}(x)$ which corresponds to a superoscillating frequency double that of the Fourier limit. Here $f_{max} = 4$ 29

2.6 Amplitude Quotient plots with respect to (a) the superoscillating variable s and (b) the superoscillating frequency f. Plot (b) has an origin at $f = 2$ as below this it would not correspond to valid values of s and as such there is a divergence beyond $f = 2$ 30

2.7 An energy quotient curve showing the relationship between the superoscillating variable a and E_Q for $n = 1$ 35

2.8 A figure showing the amplitude curves for different bandwidths ω_0 for the $n = 1$ Aharonov superoscillations. 36

3.1 A figure showing the system for approximation by Fourier optics. A plane wave of wavelength λ illuminates an aperture array in the plane $\{z_0, x\}$ and is then diffracted across a distance L, (which is large compared with the wavelength and shown by the white space and the grey area bounded by blue dashed lines between the planes), and is measured at the diffraction plane at $\{z_1, y\}$. In this the β_j and c_j are as defined in equation 3.1, and x and y are parallel but separated by $z_1 - z_0 = L$. 40

3.2 A diagram depicting a set of $\{c_j\}_j$ and $\{\beta_j\}_j$ as an example and demonstration of the constraint requirements detailed in equation 3.3 and below 41

3.3 A figure depicting the definition of ϵ_k (green line) and how it relates to c_j (red cross) and β_j (red line) 44

3.4 This figure depicts a Heaviside step function as described in equation 3.27. 47

3.5 An illustration of a basic convolution as described in equation 3.29 this is the convolution of two equal width slits with $\beta = \{1, 1\}$ and $c = \{-1, 1\}$ with both β and c are in arbitrary units 48

3.6 A function $\Psi_{j',m'}(k)$ with $c_{j'} - c_{m'} = -1.5$ and $\beta_{j'} = 1$, $\beta_{m'} = 2$ . . . 49

3.7 The intensity profile of a single slit aperture with the zeroes highlighted. This was generated by using equation 3.42 with $a = 2$, $\lambda = 1$, $L = 10$, and $c_j = c_m = 0$ 55

3.8 The intensity profile for double slit diffraction. This was generated by using equation 3.42 with $a = 2$, $\lambda = 1$, $L = 10$, and $c_0 = -3$, $c_1 = 3$ 56

3.9 The zoomed in intensity profile for double slit diffraction, focused on the site of fastest oscillation. This was generated by using equation 3.42 with $a = 2$, $\lambda = 1$, $L = 10$, and $c_0 = -3$, $c_1 = 3$ and focuses on the interval $[3.5, 6.5]$ 57

4.1 A figure illustrating the design used for annular aperture array, adapted from Toraldo di Francia [1] and detailed in table 6.3 67

4.2 A figure depicting the simulated diffraction pattern (a.) and the design (b.) of a slit aperture array that was produced for tests by optical lithography. It can be seen that there are features that are on the order of the wavelength of the phonons in GaAs $\approx 1\mu m$ 68

4.3 A graphic showing a circular aperture based design for superoscillatory diffraction. The red apertures represent an aperture diameter of $4\mu m$ and the blue apertures are of diameter $5\mu m$. The offset blue apertures are at an angle of $(2n+1)\frac{\pi}{4}$ from the plane of the red apertures 69

4.4 Design and simulated diffraction pattern of the SDD1 aperture array. This is a full design with multiple slit widths: red$= 3.375\mu m$, purple$= 3.5\mu m$, blue$= 3.75\mu m$, green$= 4.0\mu m$. The diffraction pattern graph is intensity in $\frac{W}{m^2}$ vs position along the y-axis in m. This is one of the designs that was used in experimental validation via DMD experiment 71

4.5 Design and simulated diffraction pattern of the SDD2 aperture array used to verify that Fourier optics is a valid method. This is a double slit design with a single width: green$= 4.0\mu m$. The diffraction pattern graph is intensity in $\frac{W}{m^2}$ vs position along the y-axis in m. This is one of the designs that was used in experimental validation via DMD experiment 72

4.6 Design and simulated diffraction pattern of the SDD3 aperture array used to verify the highest frequency component within the aperture array diffraction pattern. This is a double slit design with a single width: red$= 3.375\mu m$. The diffraction pattern graph is intensity in $\frac{W}{m^2}$ vs position along the y-axis in m. This is one of the designs that was used in experimental validation via DMD experiment 73

4.7 Design and simulated diffraction pattern of the IDD1 aperture array used to iteratively test permutations of the apertures arrays solved with the tools in 3.4. This is a multi-slit design with a single width: brown= $5.375\mu m$. The diffraction pattern graph is intensity in $\frac{W}{m^2}$ vs position along the y-axis in m. This is one of the designs that was used in experimental validation via DMD experiment 74

4.8 Design and simulated diffraction pattern of the IDD2 aperture array used to iteratively test permutations of the apertures arrays solved with the tools in 3.4. This is a multi-slit design with: blue= $2.625\mu m$ and brown= $5.375\mu m$. The diffraction pattern graph is intensity in $\frac{W}{m^2}$ vs position along the y-axis in m. This is one of the designs that was used in experimental validation via DMD experiment 75

4.9 Design and simulated diffraction pattern of the IDD3 aperture array used to iteratively test permutations of the apertures arrays solved with the tools in 3.4. This is a multi-slit design with: blue= $2.625\mu m$ and brown= $5.375\mu m$. The diffraction pattern graph is intensity in $\frac{W}{m^2}$ vs position along the y-axis in m. This is one of the designs that was used in experimental validation via DMD experiment 76

4.10 Design and simulated diffraction pattern of the IDD4 aperture array used to iteratively test permutations of the apertures arrays solved with the tools in 3.4. This is a multi-slit design with a single width: blue= $2.625\mu m$. The diffraction pattern graph is intensity in $\frac{W}{m^2}$ vs position along the y-axis in m. This is one of the designs that was used in experimental validation via DMD experiment 77

5.1 A figure showing 4 panels demonstrating (a) the Full Wave across a range of $[0, 1000]$; (b) the Restricted Wave, where we take a section around the highest metric values from the wave to look at the wave around that point; (c) the Full Metric, which demonstrates what values the Berry metric takes on and where; and (d) the Restricted metric which shows the metric in and around the highest peak of the metric. This figure clearly shows the flaws in the metric, as it achieves values far higher than $k_0 = 1$ in many different places, but also shows how if you only look within certain regions, it is possible to miss the majority of the divergent behaviour. 85

5.2 A figure showing the results of the initial runs of the Berry reproduction simulation. The different panels show (a) the Full Wave, (b) the Restricted Wave, (c) the Full Metric, and (d) the Restricted Metric. This figure clearly shows the divergence of the metric above $k_0 = 1$. 87

5.3 Graphs showing the difference between the histograms of the various local wavevectors found using the Berry method over different windows (a) a range of $[0, 1000]$ and (b) a range of $[80, 120]$. The number of waves this was run over was 50000, and so count values of 50000 correspond to the particular $k/k0$ value occurring in every wave at some point. It is interesting to note that there is any difference, as although this was run on the same data, restricting the range shows how windowing can affect the results. 88

5.4 A histogram showing the distribution of superoscillating metric g values and the number of times they appear within a random field over a set of $50,000$ random fields. This graph was made using the novel detection method detailed in section 5.3. There are a total of 1717 counts here, which corresponds to a superoscillatory probability of $P(g > 1) = 1717/50000 = 0.03434$ 92

5.5 A figure depicting the different winding functions $w(t, \zeta)$ (circular) and $\omega(t, \zeta)$ (elliptical) of $f(t) = \cos\left(\frac{1}{2}t\right)$ at different winding frequencies ζ. The centre of mass, depicted by the cross indicates the amplitude of each winding frequency within the function. Most winding frequencies will be near zero, with only those corresponding to Fourier frequencies having a larger amplitude, as can be seen in $\zeta = 0.5$. Here, $g = 2$ and $n = 2$ for the elliptical winding pattern 96

5.6 A figure depicting the Fourier (circular, red) and Aharonov (elliptical, blue) winding patterns and centre of mass (CoM) positions for an Aharonov function $f(x)$ with $h_j \in \{-1, -1/3, 1/3, 1\}$ and $g = 4/3$. Here, $g = 4/3$ and $n = 4$ in order to get a constant coefficient between the Fourier and Aharonov transforms. That constant relating the Aharonov and Fourier windings for this system is $C \approx 1.85$. We do not consider the contributions of the relationships between $\zeta = 0$ and $\zeta = 2/3$ winding frequencies. The reason for this is that they are not Fourier frequencies of the function $f(x)$ and although, for $\zeta = 2/3$, there are some CoM deviations between Fourier and Aharonov transforms, this is likely because of ringing effects natural in a finite discrete winding calculation. This highlights the importance of using both the Aharonov and Fourier transforms in conjunction. 99

1 A figure illustrating the different set notation that may be used in the following chapters. The circle on the left is set A, and the circle on the right is set B. The purple area in the middle is the intersection of the two sets, $A \cap B$. The two circles and their intersection is the union of the two sets $A \cup B$. The purely red area of set A is the set difference of $A \setminus B$, and the purely blue are of set B is the set difference of $B \setminus A$. The white area is then the intersection of the two complements of the sets, $A^c \cap B^c$ 114

Abbreviations

DMD Deformable Mirror Device.

FEM finite element method.

FWHM full width half maximum.

HPC high performance computer.

Hz Hertz.

m meters.

MPSL mirror plane superlattice.

NA Numerical Aperture.

NDT non-destructive testing.

OSM Optical Super-Microscope.

PF pupil filter.

SLM Spatial Light Modulator.

SNR signal to noise ratio.

SO superoscillation.

SOL Superoscillatory Lens.

UoN University of Nottingham.

W Watts.

Chapter 1

Introduction

Vibrations. A phenomena which exists in all matter, irrespective of size, temperature, location or state. In one way or another, all matter vibrates. Within this intricate interplay of oscillations, forces and damping, patterns emerge the longer we gaze at this mesmerising mess. Eventually we start to notice patterns about the patterns, how they interact, when they occur and what causes them. We categorise, order, sort, sift and condense these rules, refining more and more over time until we can start to produce these patterns ourselves, and use them to our benefit. From these 6 chapters we hope that the study of some new physics can be digressed, discussed and dissected. It is our sincerest hope that these ideas are communicated in a clear, concise manner and that they can be evaluated without tedium.

This introductory chapter introduces the main thrust of this thesis, designing superoscillatory acoustic aperture arrays, and discusses some of the background of the two main topics that this area intersects: acoustics and superoscillations.

1.1 Thesis Overview

In this thesis we will be trying to answer several questions: Are superoscillating acoustic apertures possible? Can we detect the superoscillations they produce? Can we create a framework to design them? Can we manufacture the designs? Do the designs produce what we expect them to? What are the difficulties involved in this process? What are the limitations of these processes? In the course of this thesis we will try to answer all of these questions, and have them addressed by the end of the thesis, or if not fully answered, at least have laid the groundwork for the answer to be pursued further.

The thesis is structured into 6 chapters and in such a way that all chapters should flow naturally into one another. Arguments and information in one chapter might rely on information presented in previous chapters, and where appropriate this will be referenced or restated. A brief synopsis of this thesis may be seen given as: introductory sections explaining the basics of acoustics (section 1.2) and superoscillations (section 1.3), why they are interesting, applicable and worth researching. Followed by a chapter on foundational theory (chapter 2) of both acoustics (section 2.2) and superoscillations (sections 2.3, 2.4), where foundational theory will be built up to support the proceeding chapters. This is then followed by the major theory chapter of the thesis chapter 3: Apertures. This chapter goes into detail about design processes and theory behind the designs of the acoustic apertures that are being presented in this thesis. It also presents some interesting results that were found as a part of the design process. Following the designs of chapter 3, they are put to the test in both simulation and experiment in chapter 4: Results. This chapter presents the results from the simulation of the designs and discusses the experiment that the simulations were based on. Brief discussion is given to each design within the context of the results, but holistic analysis is given in later chapters. The results chapter is then precedent to the Detection chapter, chapter 5. This chapter is primarily concerned with the detection algorithms used for determining whether a superoscillation is present within a random field and is concerned with discussions of previous methods, their flaws and benefits (section 5.1), reproduction of results (section 5.2), and improving detection algorithms through novel approaches(section 5.3). This leads nicely into the final chapter, Chapter 6: Conclusions. In this chapter we bring all the other chapters together, showing how the questions set forth at the start of this section have been answered throughout, as well as showing where the deficits are. This chapter starts with further discussion on the intersection of the theoretical and simulated results in chapter 4, highlighting where they have agreed well, where they have not and possible reasons why. These deficiencies in theory lead nicely into a section on future work in the field of superoscillations and superoscillating acoustics, section 6.2. Finally, everything is wrapped up in the final section of the conclusion, section 6.3, discussing whether the questions were answered, whether they can be answered by future work in the area, or if they completely evaded scrutiny. After the conclusion, there are only appendices and bibliographies to examine. The appendices are referenced throughout the text of the thesis, but were considered tangential enough work to be included in an appendix rather than in the main body of the thesis.

1.2 Acoustics

Acoustics is the study of sound, its properties and how it travels through different mediums. It encompasses the largest and smallest phenomena involving sound, including the study of geological phenomena such as seismic waves [2]; architectural acoustic design as in the Sydney Opera House [3]; down to quantum effects such as bandgaps in semiconductors [4] and beyond. With this broad range of topics covered by the study of acoustics, it has found continued use in many modern technological and academic fields.

The study of acoustics is a subset of the study of vibration, and thus has application and implication just about everywhere that something vibrates. Sound at it's most basic is a mechanical wave, one where the wave is propagated by forces between objects at any scale, rather than a perturbation in a fundamental force. In a medium, this mechanical wave leads to compressions and rarefactions of a material, which transmit the wave as it propagates outwards through the medium. The inherent need for a medium is another property of sound. Sound is an emergent behaviour of deformations in a material, it acts as the phenomena that transmits, but not the cause of the deformation. Imagine a stone being dropped into a very still pond. The ripples that form may displace or disrupt the surface of the pond, but they did not cause the original displacement, it was the stone. This analogy essentially communicates what sound is, it is ripples of displacement within a medium. These longitudinal waves communicated through the continuous deformation of particle positions that causes compressions and rarefaction, changes in pressure that correspond to the force or impulse that was imparted on the media.

As such sound can be found in all states of matter, in fact the only place that sound is not found is within complete vacuum. This broad application of the phenomena means that its study and mastery is vastly useful to our modern lives, and has indeed yielded many technological leaps. From the very basics of communication through language, or noise, to the quantum applications of phonons in band gap structure, decoherence phenomena and momentum transfer, there is no scale of matter at which sound is not an important and relevant field.

In this thesis we are primarily concerned with sound propagating through solid media, specifically those of isotropic, or near isotropic crystals. These crystals allow for simplification of much of the theory surrounding wave propagation in media, as highly anisotropic crystals give rise to their own fascinating phenomena. It is unfortunate then, that we wish to avoid these phenomena, as they have been exploited in may ways, such as the phenomena of phonon caustics and within non-destructive testing to great effect. However, the behaviours of these phenomena are complex and thus beyond the scope of this thesis.

In simplifying to isotropic or near isotropy we eliminate the complicated behaviour of waves and phonons transmitted through complicated geometric and topological structures within the crystals, such as those explored in [5] Yamamoto et al. and consider instead, the most basic case. This basic case can be likened to that of the pond analogy, where waves transmit evenly within a calm liquid, whereas anisotropy could be considered trying to wrap your head around the mechanics and dynamics of sound propagating through flood waters filled with raging vortices, detritus and other confounding influences. Thus let us stick to our pond and delve into what it can teach us about isotropic acoustic materials.

It is pertinent, when discussing a topic, to divulge the language of the topic. Therefore as a part of this introduction, we will define some commonly used terms and phrases. Those mathematical definitions which need to be covered will be given later in the basic theory chapter (Chapter 2) in the acoustics section. For now a qualitative description will suffice for most things.

To start: phonons. Phonons are a quantisation of lattice vibrations within a solid medium. This is to say that they are pseudo-particles of sound that can be used and treated like quantum objects to explain some of the phenomena we see within crystals and other solids. Phonons exist as harmonic modes of the crystal lattice, and have an energy-frequency relationship much like their optical counterparts photons. However, as they are a function of their crystal lattice environment, they cannot be separated from it, and are in fact a tool used to describe certain phenomena, rather than a phenomena themselves. Much like how standing waves on the surface of this fictitious pond may seem to move without disturbing the surrounding water, it is an illusion, as there is constant jostling, collision, shear and stress within that serene pond that lies just beneath the surface. However, in almost all facets that count, those standing waves, or even free propagating waves can be considered a phenomena unto themselves, and it is indeed with these phenomena that this research concerns itself, the control and super-focusing, methods where sources are concentrated beyond the Rayleigh criterion, of ultrasonic vibrations through a lattice.

To truly understand phonons and vibrations within crystals we must turn to solid state physics, and comprehend what is meant by a crystal lattice and how it vibrates. Within perfect crystals, i.e. those without defects or impurities, the crystal lattice can be described entirely by the relationship of the elements that constitute the material and how it was formed [6]. Plastics, for example, tend to be very messy in their crystal structure, due to the long chains of hydrocarbons and complicated interactions between individual polymer strands and other polymer strands. Crystalline metals on the other hand form extremely ordered crystal structures on the small scale, where individual domains or grains may all align in their structure, but it is very difficult to actually achieve a large piece of crystalline metal with all the same grain, or without domain boundaries [6]. The reason these things matter is that these domains and grains cause internal stress within the metal when external stress is applied, thus any weaknesses within a metal tend to lie along these grain boundaries or domain boundaries. These defects are as integral to the study of solids and their phenomena as the crystal structure and elements that constitute them. If we turn to extremely ordered large crystals such as those formed by crystalline ionic compounds such as table salt or calcium carbonate; or crystalline covalent compounds such as diamond, quartz or pure silicon; we can observe similar, yet distinct phenomena to those provided by pure elemental metals or alloys. A crystalline lattice describes how atoms or nodes of a crystal arrange themselves in repeating units to form the greater crystal. The shape of the crystalline lattice is determined by the chemical properties of the elements that constitute the crystal, as well as the conditions under which the crystal was made. These also determine other bulk properties of the solid, such as electrical, thermal, and magnetic properties. This basic unit of a crystal has some interesting properties, as these form the building blocks of understanding how sound and phonons are transmitted throughout the bulk media.

The details of crystal structure lead directly to properties of the bulk media, such as Young's modulus, thermal conductivity and heat capacity, electrical conductivity, resistance etc, and are the foundations for much of material science. The way that these individual crystal units interact, form crystal grains, boundaries and behave in bulk, are beyond the scope of this thesis, and although we will be tangling with some of the ramifications of these structures, we do not need to analyse them directly. The biggest way that we interact with the crystalline mechanics and dynamics is when considering the GaAs/AlAs superlattices that are used to generate the coherent phonons necessary for the experiment. GaAs is a semiconductor that supports many modes of phonons, however, one of the key reasons that it is used is that it is near-isotropic. This means that the mathematics for dealing with the phonon transport across the crystal can be significantly simplified, as we assume that it is isotropic.

The superlattices of GaAs/AlAs are what is is known as mirror plane superlattice (MPSL)s and are used as a way to generate coherent phonons. Controlling precisely the thickness of the mirror planes interacts strongly with the phonon wave, and allows for standing waves of phonons to occur within the structure [7]. This phase control can be used to cause coherence in the optically generated phonons within the superlattice, as this system can be approximated to an open ended cylinder with the phonons travelling into the GaAs bulk media. Spatially modulating the generation zones of these phonons allows for specific diffraction patterns to be designed, hence the shadow masks that are created later in this thesis.

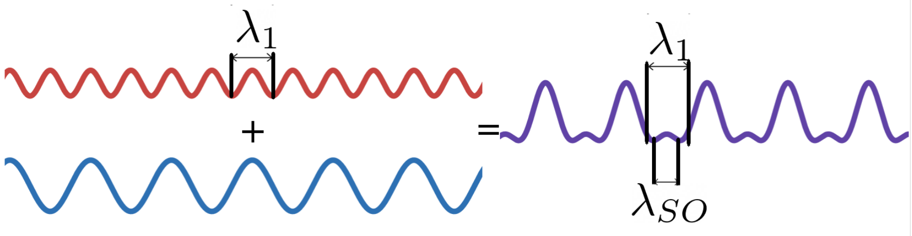

Figure 1.1: Superposition of two waves to create a superoscillatory wave. It is shown that a part of the combined wave has a smaller wavelength than that of the smallest wavelength that constitutes it.

1.3 Superoscillations

Superoscillations are a particular form of destructive interference [8] that have the intriguing property of having a local region of a wave that can oscillate faster than the fastest Fourier component of said wave. This effect can be seen in figure 1.1, where two waves superpose to create a third wave with a local region of higher oscillation frequency, and thus lower wavelength, than the waves that constitute it. Superoscillations were likely first noted as a phenomenon in World War 2 radar systems, where it was found that carefully balancing power to arrays of radar antennas could cause an arbitrarily tight radar beam [9]. However, it wasn't until the 1990's with work between Aharonov, Berry, and others that superoscillations were first studied as their own phenomena [9]. Since the advent of the field of superoscillatory study there have been many revelations. From its original use in Aharonov's work on weak quantum measurements [10]; to theoretical results in Berry's work predicting superoscillations in random fields [11]; to more recent experimentally verified results such as superspectroscopy, where chemicals of near identical spectra can be delineated using superoscillatory excitation [8], the study of superoscillations has yielded useful results throughout its course.

To give a qualitative description of superoscillations, they are a phenomena whereby a local region of an oscillatory function oscillates arbitrarily faster than its fastest Fourier component. This arbitrarily faster oscillation gives rise to some interesting possibilities. As the superoscillations can be arbitrarily fast, it means that a particular part of the function or wave can be used to interact with or image things far smaller than should be possible [9, 12], or stimulate classically forbidden states in quantum systems [13] and indeed solve wave equations such as the Klein-Gordon equations [14] which gives rise to the exciting possibility of superoscillatory quantum states.

Optical superresolution, and indeed superoscillations are a much sought after phenomena as they provide a possible improvement beyond current imaging systems and techniques, but not without trade-offs. According to Chen et al.'s review [12] and expanded upon in the original by Huang et al in [15] Fresnel lens spot size can be considered to contain 3 different regimes, subresolution, superresolution, and superoscillation. According to [12] and [15] the spot size of a subresolving Fresnel lens, is bounded to a lower spot size limit of $d_{spot} \geq 0.61\lambda/NA$, where NA is the numerical aperture of the Fresnel lens and d_{spot} is the spot size and λ is the wavelength of the light illuminating the Fresnel lens, whereas a superresolving Fresnel Lens is one bounded between $0.38\lambda/NA \leq d_{spot} < 0.61\lambda/NA$, and thus a superoscillating Fresnel lens is such that $d_{spot} < 0.38\lambda/NA$. A natural question is to ask about the distinction between the 3 regimes, as why do we need to distinguish superresolving, and superoscillating? The answer lies in the fact that superresolving spots do not necessarily have to beat the spot size of the highest spatial Fourier frequency involved in the function, whereas a superoscillation does. Huang et al [15] assert that this imposes a superoscillatory criterion of $d_{spot} < 0.38\lambda/NA$, and come to this conclusion by approximating the maximum single spatial frequency spot focussed through a lens of numerical aperture NA to a zero order Bessel function of:

$$J_0(2\pi r NA/\lambda) \tag{1.1}$$

and finding the first zero location, which lies at $r_s = 0.38\lambda/NA$. Thus there is a superresolution region, between the Rayleigh criterion $r_c = 0.61\lambda/NA$ and the superoscillation region, r_s where the trappings of superoscillations, specifically the high side lobes of the superoscillatory region can be avoided. The superoscillation criterion is used as a limit by Huang et al to design superresolving Fresnel zone plates and binary phase masks whilst maximizing the distance between the central superresolving region and any unwanted high amplitude side lobes.

This analysis of Huang et al.'s gives a good way to discuss Rogers et al.'s results in [16], in which a Superoscillatory Lens (SOL) is designed by a particle swarm optimization algorithm and then used it to resolve a variety of different objects. The SOL gives a local "hotspot" as they term it of $185nm$, which, given that it is illuminated by $640nm$ light and has a numerical aperture of $NA \approx 1.9$, is below the Rayleigh criterion $r_c = 0.61\lambda/NA = 205nm$ but not below Huang et al.'s superoscillatory criterion of $r_s = 0.38\lambda/NA = 127nm$. Being located within Huang et al.'s sueprresolving region is likely why Rogers et al.'s central spot is such a "hotspot" because it has not yet reached the superoscillatory criterion which would mean that the central spot intensity would decrease faster than the central spot size would decrease. Rogers et al. use this SOL to image slit and circular apertures and are able to resolve them far better than they would otherwise be able to be resolved. They show this by comparing to a normal microscope lens image of these objects, where distinctions between the objects are unable to be resolved.

It is interesting to note that in the majority of applications, either monochromatic spatial superresolution is trying to be achieved [1, 9, 11, 12, 16] but in Li et al.'s paper they attempt to produce an achromatic superresolving image using white light from a Xenon lamp [17]. Their use of a metasurface filter to generate the superoscillating wave packet, which then illuminates a $20\mu m$ hole shows significant improvements over the standard white light imaging, although once again reinforces one of the features of superoscillations, the high intensity side lobes. This feature is present in most every optical system using superoscillations for superresolution, as shown also in Rogers et al.'s paper [16]. The signature spot within a circle is a hallmark of most annular superoscillating optical imaging systems due to these side lobes, but as Huang et al showed [15], these are not necessarily a feature of all superresolving systems. As long as a superresolving system stays below the critical superoscillating criterion, r_c, then the side lobes of the optical system are not necessarily more intense than the central spot.

In Wong and Eleftheriades [18] they show evidence of their Optical Super-Microscope (OSM) system which exploits a Spatial Light Modulator (SLM) to generate a superoscillatory point spread function rather than using a shadow mask or spatially modulating the light that illuminates the object. As is shown in their paper, Wong and Eleftheriades manage to achieve superresolution with this method and validate this with the comparison of the spot size of their system without the superoscillatory SLM design. They also compare the resolution of two spots between the OSM and normal microscopy, finding that superresolution between two objects is achieved. Wong and Eleftheriades report a reduction in spot size of 72% and an improvement of resolution between two spots of 75%, and also have video evidence of a real time imaging system resolving the two spots in their supplementary information. Real time imaging of moving objects using OSM is a fascinating look into how robust Wong and Eleftheriades approach is and how useful it could be for other systems. It is interesting to note however that they claim to have achieved an improvement of spot size and resolution down $72 - 75\%$ of the Rayleigh criterion, r_c, however, this, at the lower end, corresponds to a spot size of approximately $0.44\lambda/NA$, putting it above the superoscillating criterion, r_s, and within Huang et al.'s superresolving, but not superoscillating region. This distinction is not a criticism, Huang et al. state that this superresolving region is likely the most practical region for investigation of superresolution as true superoscillation leads to larger side lobes and thus lower efficiency when it comes to imaging [15]. Wong and Eleftheriades also talk about the efficacy and practicality, discussing the necessity for a larger "region of silence" between the central spot and high intensity side lobes.

The concept of real time imaging in [18] of brings the consideration of time into the discussed systems, and due to the nature of superoscillations, it is possible to create both spatial or temporal superoscillations. Temporal superoscillations are exploited in McCaul et al.'s paper [8] to achieve superspectroscopy by introducing waves of specific amplitude and phase together in order to excite a superoscillation at a chosen superoscillatory frequency absorbed more readily than the fundamental frequencies that constitute that waveform. Spatial superoscillations are exploited in Rogers et al.'s paper [16] to cause a superresolving spot, as well as the superdirective radar beam reported in [9]. Although spatial superoscillations have been demonstrated, it has been shown that they have a bias towards superoscillating in a single direction [19]. Whilst this does not mean that superoscillations in more than 1-D cannot occur, it does mean that the trade-offs in amplitude and indeed focus spot eccentricity are required. That is to say that superoscillating in a single dimension will give the most freedom when it comes to optimising for other things like detectability, energy efficiency and other important physical considerations and constraints.

Early work in the field besides the superdirective radar beams, was conducted by Toraldo di Francia, whereby he attempted to make annular arrays of lenses superoscillate [1]. This work was more based on Fresnel lens concepts, in which each annular region was of a different transmissibility, and thus with careful tuning of the thickness of each Fresnel lens annulus, it was possible to cause superresolution. This phenomena, whilst not called superoscillation at the time, was clearly of interest, even as far back as the 1950's. It wouldn't be until the 1990's that superoscillations would come to have their name in a paper by Aharonov [10]. In this paper he proposed that infrared photons trapped within a perfectly reflecting box with only the smallest gap from which to escape, will eventually be detected outside of said box. Contemporary understanding of quantum mechanics did not allow for this, as the box was modelled as an infinite potential well. Instead the interference of the photons with each other would eventually lead to superoscillatory components and those components can leak out of the photonic prison. This publication of this paper became the instigating event for the field of superoscillatory research.

Since this early work in superoscillations has been conducted, there have been many advances in the field, including in recent years. Some of the most recent papers that have produced results in the field have shown both practical effects, such as McCaul et al.'s work in superspectroscopy [8], and driven theoretical interest in some of the most fundamental areas of physics, like Addazi et al.'s work into superoscillatory quantum and cosmological fields [14]. Aharonov, one of the progenators of the field, has himself recently published a paper on a new method for generating superoscillations, which gives a generating function to a large class of superoscillatory functions [20].

This decades long interest in the field has been driven by the potential promise it holds in stretching the limits of classical, and even quantum, systems. The ability of superoscillations to oscillate arbitrarily fast [9] leads to many exciting potential applications. Almost any system that has a wave form or solution as a part of it could potentially benefit from superoscillations. From modern technological pursuits such as communications, medical devices, imaging, and lithography; to probing the frontiers of physics in quantum physics, cosmology, material sciences and high energy physics; even to other academic fields such as cryptography, architecture, geology and mathematics, superoscillations have wide application and appeal.

For this thesis we will be concentrating on spatial superoscillations generated by spatially modulating light through aperture arrays. This spatial light modulations allows for the generation of coherent phonons within a superlattice that then propagate through a given substrate and are measured on the reverse side of the substrate medium. This experimental set up is shown in figure 2.1 and discussed further in the associated Chapters 2 and 4

Chapter 2

Foundational Theory

This chapter describes the foundational theory used throughout this thesis. It covers the two major parts of the main body of the work: acoustics and superoscillations. Each of these topics have books and reams of research dedicated to them, as such we will be extracting just the relevant parts of these topics to this thesis. We will start with a discussion of the experimental setup which will lead nicely into the theory surrounding the experiment, particularly acoustics, and then followed by an initial treatment of superoscillations. Before starting we feel it is important to point readers to some of the notation that will be used in the following chapters. This can be seen in Appendix 6.3

2.1 Experimental Set up

The experiments conducted by Khouloud Sellami and Tony Kent , had produced some results that were promising, however due to unforeseen circumstances these have been lost. This loss of experimental data is a blow, however, does not invalidate the theoretical work that was done to support these endeavours. The experimental setup can be seen in 2.1. The designs were originally made by optical lithography,

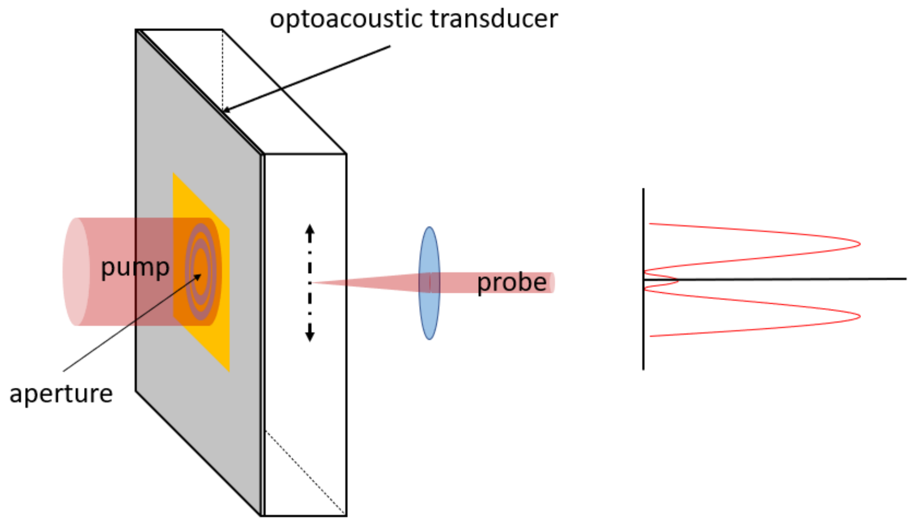

Figure 2.1: A graphic showing the experiment that is being considered in the theory for this thesis. It shows a incoming laser beam being spatially modulated by a gold shadow mask in the form of an annular design. The spatially modulated light then illuminates an opto-acoustic transducer, a GaAs/GaAsAl superlattice approximately $10\mu m$ thick, that generates coherent phonons of wavelength $\lambda_{mat} = 1\mu m$ that then propagate through a medium of GaAs $450\mu m$ thick. These phonons are then measured as a diffraction pattern by a rasterising probe beam that takes advantage of interferometry to measure the deformities in a 100nm polystyrene detector that was deposited on the reverse of the GaAs substrate using spin-coating technique

depositing a gold shadowmask aperture array directly on a GaAs/AlAs superlattice of $\approx 10\mu m$ which was grown on a bulk medium of GaAs of approximately $450\mu m$ thickness. The superlattice was used to generate coherent phonons that could propagate through the GaAs substrate and be detected the other side. Whilst initially the optical lithography method for generating spatially modulated light was the only option, the superlattice is now illuminated using a Deformable Mirror Device (DMD) to spatially modulate the light rather than having to have deposit a shadowmask via optical lithography on a separate sample for each design. This has multiple improvements over the old lithography methodology as it means that multiple different designs can be tried on the same bulk medium without having to worry about defects in each of the media, designs, or the deposition of the thin-film polystyrene interferometer. The thin film polystyrene interferometer is deposited directly onto the

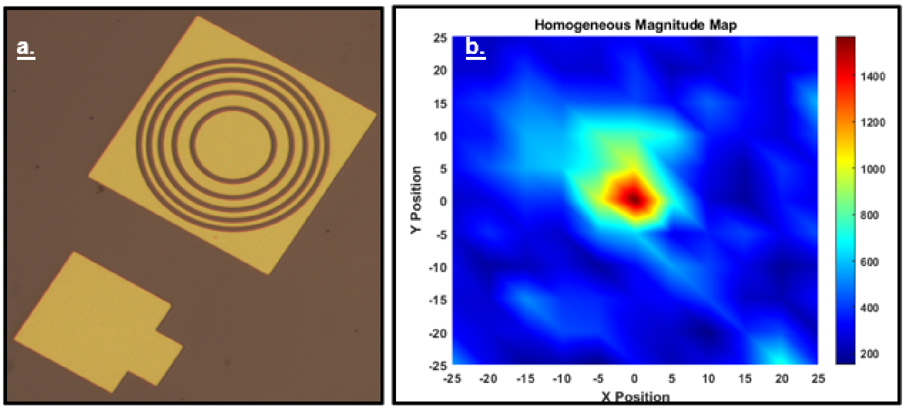

Figure 2.2: (a.)Illustrates the gold shadowmask created by Khouloud Sellami by optical lithography for a design based off Toraldo di Francia's designs [1] (b.) the measured strain field at the other side of the substrate. Here can be clearly seen a spot of FWHM $\approx 10\mu m$. This design is detailed in table 6.3 as EDD1. This figure was a part of a private communication from Kholoud Sellami and Tony Kent providing experimental feedback for the designs.

material and is imaged using a rasterised probe path. This method allows for a full 2D scan of the substrate area and thus allows for a better realisation of the diffraction pattern. Whilst this isn't necessarily important for aperture designs based off the slit aperture designs, it is very important for other diffraction apertures. It also allows the resolution of any anisotropic or non-linear effects to be realised by comparing the detected diffraction pattern to the simulated and calculated ones. The thickness of the bulk substrate guarantees that we are in the Fraunhoffer regime, $L >> \lambda_{mat}$, and so the use of Fourier optics to approximate this system is valid. Figure 2.2 depicts some early work using the optical lithography method to deposit the gold shadowmask directly onto the bulk medium, as discussed above. The figure demonstrating the measured spot size of the annular design was measured but the supporting data has since been destroyed or lost. The details for the design can be found in table 6.3 as EDD1.

2.2 Acoustics

Acoustic theory lies generally within one of two camps, fluid media and solid media. Fluid media, such as air, water and other liquids and gases pose a fundamentally different type of challenge to that of solid media. Fluid media has the dynamics of the fluid to consider, where in the "static" approximation, an unperturbed system may conduct sound much as we might expect an isotropic solid. That is to say that there are no other external factors or forces to consider when considering the propagation of sound in the media. Whereas the solid media poses a different challenge, as most solid media does not have much in the way of external dynamics to consider, instead there is the challenge of anisotropy to contend with.

Both of these challenges can be overcome, but do pose difficulties in the way of determining sound propagation through mediums. However, it is best to consider the framework that is most appropriate for the system under investigation. As discussed in the Introduction, chapter 1, the system we are looking at is that of a solid having acoustic energy injected by means of an optoacoustic transducer illuminated by a laser. The experiment is being conducted at room temperature with a GaAs substrate to act as a propagation medium and a GaAs/AlAs superlattice to act as an optoacoustic transducer to produce coherent phonons of a specific wavelength. Since the system is at room temperature, according to Wolfe in [21] "phonon-phonon scattering is so strong at room temperature that the thermal propagation is diffusive over all measurable distances." This thankfully simplifies the task of phonon propagation, as instead of having to tangle with the Christoffel tensor equation [21] and quantum effects, we can consider the acoustic energy as travelling in classical waves within an isotropic medium. Due to this, instead of coherent phonon generation regions, we consider the optoacoustic transducer as a pattern source of waves, given by some arbitrary distribution determined by each specific shadow mask design.

To describe this system, we consider some classical wave equations. The fact we have a source of waves leads us to consider the inhomogenous Helmholtz equation to describe the propagation of the acoustic waves through the medium:

$$(\nabla^2 + k^2)u(\underline{\mathbf{x}}) = q(\underline{\mathbf{x}}) \tag{2.1}$$

where ∇^2 is the Laplacian operator, k is the wavenumber, $u(\underline{\mathbf{x}})$ is the acoustic wave field, and $q(\underline{\mathbf{x}})$ is the source distribution. This can be solved via a Green's functions approach, where the Green's function for the 3D Helmholtz equation is [22]:

$$G(\underline{\mathbf{x}}, \underline{\mathbf{x}}') = \frac{e^{ik|\underline{\mathbf{x}}-\underline{\mathbf{x}}'|}}{4\pi|\underline{\mathbf{x}}-\underline{\mathbf{x}}'|} \tag{2.2}$$

and thus the solution becomes:

$$u(\underline{\mathbf{x}}) = \frac{1}{2\pi}\oint_V q(\underline{\mathbf{x}}')\frac{e^{ik|\underline{\mathbf{x}}-\underline{\mathbf{x}}'|}}{4\pi|\underline{\mathbf{x}}-\underline{\mathbf{x}}'|}d\underline{\mathbf{x}}' \ . \tag{2.3}$$

However, given the system we are considering, we can assume that z is large and fixed and that the source function $q(\underline{\mathbf{x}})$ is locate at $z = 0$, and so we use the parallel rays approximation to simplify things to:

$$u(\underline{\mathbf{x}}) = \frac{e^{ik|r|}}{8\pi^2|r|}\int q(\underline{\mathbf{r}}')e^{-ik[\underline{\mathbf{r}}'\cdot\hat{\underline{\mathbf{r}}}]}d\underline{\mathbf{r}'} \tag{2.4}$$

where $\underline{\mathbf{r}}'$ is the position vector for the heat source, given by $\underline{\mathbf{r}}' = x'\ \hat{\underline{\mathbf{x}}} + y'\ \hat{\underline{\mathbf{y}}}$ and $\hat{\underline{\mathbf{r}}} = \frac{\underline{\mathbf{r}}}{|\underline{\mathbf{r}}|}$ is the unit vector parallel to the $\underline{\mathbf{r}}$ vector denoting the position under consideration at some plane at $z = z_0$ and given by $\underline{\mathbf{r}} = x\ \hat{\underline{\mathbf{x}}} + y\ \hat{\underline{\mathbf{y}}} + z_0\hat{\underline{\mathbf{z}}}$. In most, if not all calculations going forward we will be considering Fraunhoffer diffraction, and thus $z_0 >> x, y$ and so $|r| \approx z_0$, which simplifies everything to the following:

$$u(\underline{\mathbf{x}}) = \frac{e^{ikz_0}}{8\pi^2 z_0}\int q(\underline{\mathbf{r}}')e^{-ik[\underline{\mathbf{r}}'\cdot\hat{\underline{\mathbf{r}}}]}d\underline{\mathbf{r}'} \tag{2.5}$$

This is simply the spatial Fourier transform of the acoustic energy source distribution, and this fact will be used throughout this thesis to compute the acoustic diffraction patterns.

Now that we have discussed how to solve the toy system, how do we now bring it into the physical system that we are considering? We rely on an old optics trick in the Fourier transform in order to relate this analysis to the physical system. We perform this by setting:

$$k = \frac{2\pi\underline{\mathbf{x}}}{z_0\lambda} \tag{2.6}$$

where 2π is a phase factor, z_0 is the distance to the measurement plane (later we use L) and λ is the wavelength of the oscillation in the material, which encodes the speed of sound in the material. This is where we retrieve our working definition of the Fourier optics equation for our system:

$$\begin{aligned} u(\underline{\mathbf{x}}) = \frac{e^{i\frac{2\pi\underline{\mathbf{x}}}{\lambda}}}{8\pi^2 z_0} \int q(\underline{\mathbf{r}'}) e^{-i\frac{2\pi\underline{\mathbf{x}}}{z_0\lambda}[\underline{\mathbf{r}'}\cdot\hat{\underline{\mathbf{r}}}]} d\underline{\mathbf{r}'} \ = \\ \frac{e^{i\frac{2\pi\underline{\mathbf{x}}}{\lambda}}}{8\pi^2 L} \int q(\underline{\mathbf{r}'}) e^{-i\frac{2\pi\underline{\mathbf{x}}}{L\lambda}[\underline{\mathbf{r}'}\cdot\hat{\underline{\mathbf{r}}}]} d\underline{\mathbf{r}'} \ . \end{aligned} \tag{2.7}$$

Given we are working in the Fourier optics approximation it is valid to consider an isotropic view of the speed of sound in the material as holding to the relationship $c = f\lambda$. The rearrangement of this relationship is how we encode the speed of sound into the system. In the experiment described previously, the optoacoustic transducer produces coherent waves of approximately $\lambda \approx 1\mu m$, and GaAs has a longitudinal speed of sound of $4730ms^{-1}$ [23] and so these are the values used throughout this thesis.

2.3 Superoscillations

Superoscillations have the useful property of being able to oscillate faster than their fastest Fourier component. Although this qualitative description is useful, it is pertinent that we are able to describe and generate superoscillations mathematically. According to McCaul et al in [8], superoscillations can be described as a particular kind of destructive interference. To give a more formal definition of a superoscillation, we consider the qualitative description, and ask how do we know that something oscillates? Normally to answer this, we would consider the Fourier transform of a particular function; however, superoscillations are "faster than Fourier" and practically what this means is that they do not turn up in Fourier transforms. As such we can use Fourier transforms to tell us whether something oscillates normally, and it will be a useful metric to compare to, but does not encompass enough to be able to deal with superoscillations. Then to define an oscillation, we have to be very broad. We consider the turning points of a function, and find the difference between turning points of the same kind. We sort these turning points as maxima, minima and inflection points, and find the difference between different instances of each. As a maxima cannot follow a maxima without either an inflection or minima between the two maxima we term the section of the function between these two maxima, a local oscillation. The oscillation Λ will be a portion of the total function $f(x)$ given between two bounds:

$$\Lambda(x) = f([a, b]) \tag{2.8}$$

where $[a, b]$ is a closed interval dictated by the bounds a, b given as two distinct turning points of the same kind. This also gives a direct correspondence to the local wavelength and local frequency, where the local wavelength is the length of the interval: $\lambda = |a - b|$; and the local spatial frequency is given by $k_{loc} = 2\pi/\lambda$, where we use the convention of having 2π phase within a period of an oscillation. We assume the natural units of the system, so the speed of sound in the system is 1. To convert back into the physical system units, we need to reintroduce the speed of sound into the local frequency, so $f_{loc} = 2\pi c/\lambda$ where c is the speed of sound, approximately $c = 4730ms^{-1}$ [23].

We know that we want the positions of all maxima and minima given by:

$$\{\underline{\mathbf{x}}_0\} = \{\underline{\mathbf{x}} \mid \nabla f(\underline{\mathbf{x}}) = 0\} \ . \tag{2.9}$$

We then sort solutions into maxima, minima and constant by:

$$\{\underline{\mathbf{x}}_0\} \begin{cases} \{\underline{\mathbf{x}}_0^+\} \text{ (maxima)} = \{\underline{\mathbf{x}}_i \mid \underline{\mathbf{x}}_i \in \underline{\mathbf{x}}_0 \ \text{ and } \ \nabla^2 f(\underline{\mathbf{x}}_i) < 0\} \\ \{\underline{\mathbf{x}}_0^0\} \text{ (inflection)}, = \{\underline{\mathbf{x}}_i \mid \underline{\mathbf{x}}_i \in \underline{\mathbf{x}}_0 \ \text{ and } \ \nabla^2 f(\underline{\mathbf{x}}_i) = 0\} \\ \{\underline{\mathbf{x}}_0^-\} \text{ (minima)}, = \{\underline{\mathbf{x}}_i \mid \underline{\mathbf{x}}_i \in \underline{\mathbf{x}}_0 \ \text{ and } \ \nabla^2 f(\underline{\mathbf{x}}_i) > 0\} \end{cases} \tag{2.10}$$

Then for all maxima find:

$$\{\Delta\underline{\mathbf{x}}_+\} = \underline{\mathbf{x}}_n - \underline{\mathbf{x}}_m \ , \tag{2.11}$$

where $\underline{\mathbf{x}}_n \in \{\underline{\mathbf{x}}_0^+\}$ and $\underline{\mathbf{x}}_m \in \{\underline{\mathbf{x}}_0^+\} \setminus \{\underline{\mathbf{x}}_n\}$.

Similarly for all minima find:

$$\{\Delta\underline{\mathbf{x}}_-\} = \underline{\mathbf{x}}_j - \underline{\mathbf{x}}_k \ , \tag{2.12}$$

where $\underline{\mathbf{x}}_j \in \{\underline{\mathbf{x}}_0^-\}$ and $\underline{\mathbf{x}}_k \in \{\underline{\mathbf{x}}_0^-\} \setminus \{\underline{\mathbf{x}}_j\}$.

If there exists some:

$$\lambda \in \{d \mid d \in \{\Delta\underline{\mathbf{x}}_+\} \cup \{\Delta\underline{\mathbf{x}}_-\}\} \ , \tag{2.13}$$

such that:

$$|\lambda| < \frac{2\pi}{f_{max}} \ . \tag{2.14}$$

Where,

$$f_{max} = \sup\big(\text{supp}\,\big(\ \big|\mathscr{F}[\ f(x)\ ]\big|\ \big)\big) \ , \tag{2.15}$$

where supp() is the support of the given function, then $f(x)$ superoscillates. We know that the supremum of the support exists, as the function is bandlimited, and therefore has, by definition, a compactly supported Fourier Transform.

It is reasonable to ask about inflection and saddle points, so those solutions in the set $\{x_0^0\}$. For inflection points $x_{in} \in \{x_0^0\}$, there are other points in the set $\{x_0^0\}$ which are in the neighbourhood of x_{in} and thus if we gave the same treatment as above, there would always some λ which diverges as we would be dividing by an infinitesimal. As for saddle points, we also do not need to consider them, as they are the maxima between local minima, and the minima between local maxima. This means that they do not need to be considered, as the width of the oscillation between maxima and minima will be given by the surrounding maxima or minima.

We can study the behaviour of a basic superoscillating function to get an idea of what superoscillatory behaviour is like. Consider:

$$f_s(x) = (\cos(x) - s)^2 \tag{2.16}$$

where $s \in [0, 1]$ is the variable that controls the superoscillation. In the limit that $s \to 0$, it is clear that $f_0(x) = \cos^2(x)$ and thus does not superoscillate. In the limit that that $s \to 1$ $f_1(x) = \frac{1}{2}\cos(2x) - 2cos(x) + \frac{3}{2}$ which has a less obvious behaviour. This behaviour is explored in more detail in the following section, but to summarise, the local wavelength of the function $f_1(x)$ in the superoscillatory region becomes 0, corresponding to a local frequency that is undefined.

As we can see in Figure 2.3 there is a range of behaviour for the $f_s(x)$ functions with intermediate values of $s \in [0, 1]$ leading to superoscillatory behaviour. We can thus see from inspection where superoscillations occur in these functions, but we have yet to show that these are indeed superoscillations. So let us take the Fourier transform of these functions to find what we will be comparing to:

$$\mathscr{F}(f_s(x)) = \frac{1}{2}\delta(\omega - 2) - 2s\delta(\omega - 1) + (s^2 + \frac{1}{2})\delta(\omega) \tag{2.17}$$

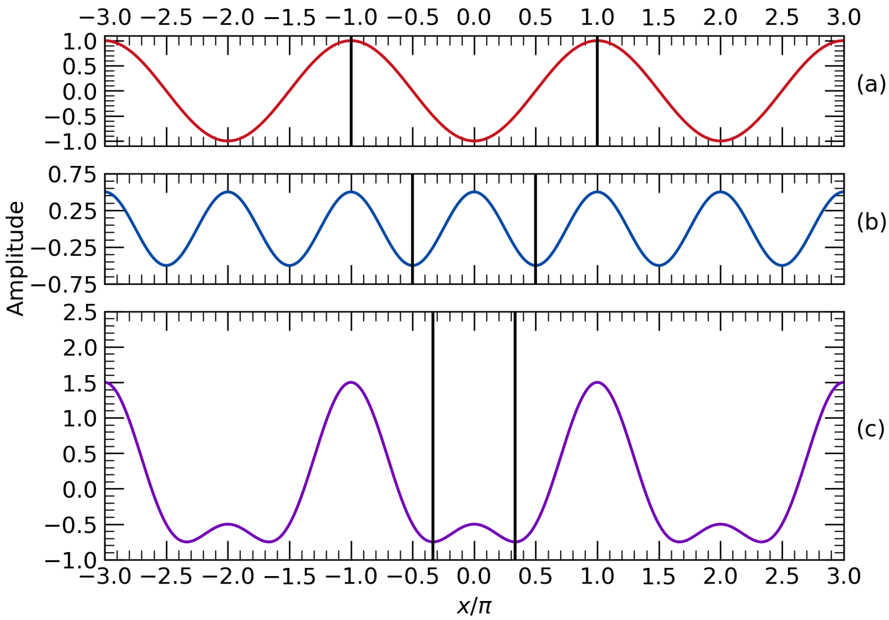

Figure 2.3: (a) A graph of $\cos(x)$, (b) A graph of $\cos(2x)$ and (c) A graph of $(\cos(x) - s)^2$ with $s = 0.5$ illustrated to demonstrate superoscillatory behaviour. The top two panels show the individual frequency components of the bottom panel. The black vertical lines occur at the first spatial period of each graph and are to aid in showing the superoscillatory region around 0. In (a) the smallest local spatial period is 2π, in (b) the smallest spatial period is π and in (c) the smallest spatial period is $2\arccos(s) = \frac{2}{3}\pi$. It can therefore both be seen and demonstrated that there is a superoscillatory region in panel (c)

Where $\delta(\omega)$ is the delta function, which is defined as:

$$\delta(x) = \begin{cases} \infty, & \text{if } \; x = 0 \\ \\ 0, & \text{otherwise} \end{cases} \quad . \tag{2.18}$$

As can be seen, there are 3 frequencies involved in $f_s(x)$, $\omega = 0, 1, 2$. These frequencies have two involved in the oscillation, and the $\omega = 0$ uniquely identifies the function we are looking at, as it corresponds to the offset from the axis. It can be seen that s, our superoscillatory variable, has no bearing on the frequencies involved, except to change their amplitude and therefore ratios.

Examining another means for getting the frequencies involved, the local wavevector method, detailed in [9, 11, 24] etc. we can begin to compare the differences in Fourier frequencies and effective frequencies.

As defined in [9, 11, 24], the local wavevector $k_c(x)$ is defined as :

$$k_c(x) = -\operatorname{Im}[\nabla \ln(f(x))] \tag{2.19}$$

which if we plug our function $f_s(x)$ into :

$$k_c(x) = -\operatorname{Im}[\nabla \ln \left((\cos(x) - s)^2\right)] = -\operatorname{Im}\left[\frac{-2\sin(x)}{\cos(x) - s}\right] \tag{2.20}$$

Now given that $\sin(x)$, $\cos(x)$, s are all real, then $k_c(x) = 0$, so this is not a particularly useful metric for this function. Since the function is 1D it is possible to easily order the turning points of the function and find the difference between them. If we consider this a measure of local wavelength, then:

$$\lambda_n = 2|x_{0_n} - x_{0_{n-1}}| \tag{2.21}$$

where x_{0_i} are the turning point positions of the function, found by solving:

$$\frac{df(x)}{dx} = 0 \tag{2.22}$$

and the factor of 2 comes from the fact that we are finding the difference between two turning points, so need to multiply by 2 to find the full wavelength. Thus let us once again put $f_s(x)$ into this formula.

$$\frac{df_s(x)}{dx} = -2\sin(x)[\cos(x) - s] = 0 \tag{2.23}$$

which has fairly intuitive solutions of $x = n\pi$ and $x = \pm\cos^{-1}(s) + 2n\pi$, which gives the local wavelength an s dependence. Given we want to find the smallest wavelength, which corresponds to the highest frequency, we want to know:

$$\inf(\lambda_n) = \inf(|x_n - x_{n-1}|) \tag{2.24}$$

There are a few tricks that can help us with this problem, first is realising that a maxima occurs every $n\pi$. This can be verified by inspection of the graph and the function $(cos(x) - s)^2$. Therefore, the smallest distance between turning points is always $\cos^{-1}(s)$, because minima occur every $2m\pi \pm \cos^{-1}(s)$ and so the distance between maxima and minima is $|n\pi - (2m\pi \pm \cos^{-1}(s))|$. This is at its smallest when $m = \frac{1}{2}n, \forall m, n \in \mathbb{N}$, leading to the previously stated solution.

Since this is our smallest distance, let us see what our limiting values of s do to this distance. At $s = 0$, $\cos^{-1}(0) = \frac{\pi}{2}$, leading to $\lambda_{min} = \pi$ and $f_{max} = 2$, a recovery of our fastest Fourier component. For $s = 1$, $\cos^{-1}(1) = 0$, leading to $\lambda_{min} = 0$, which is obviously not a physical wavelength, so the next smallest is between $m = 0,\ n = 1$ which gives $\lambda_{min} = \pi$ leading to a frequency of $f_{max} = 1$. The reason that we point out the limiting behaviour, is that it gives us a range of frequencies that we can look at:

$$f_{max} = \frac{\pi}{\cos^{-1}(s)} \tag{2.25}$$

which is divergent as $s \to 1$ and known at $s \to 0$ leading to an interval of $[2, \infty)$ for the range of local frequencies in the signal.

What this result shows is that s can control the local frequency of the superoscillation, and can achieve an arbitrarily fast oscillation above the Fourier limit. However there is a trade-off here. Although an arbitrarily fast superoscillation can occur, the amplitude of the superoscillation is suppressed quadratically as s increases. This exchange of frequency for amplitude is compounded when we consider the energy carried by each part of the wave.

The energy carried by the wave can be considered the integral of the linear intensity of the wave over a full period. The linear intensity is then given by the modulus squared of the function, $|f(x)|^2$, and so energy is given by:

$$E = \int_{-\infty}^{\infty} |f(x)|^2 dx \ , \tag{2.26}$$

and is plotted in figure 2.4. Which for our purposes, we only want to consider the energy for a single period, to be able to compare the energy carried by each part of the wave, and as the wave is periodic, it would introduce redundancies to the integral to consider more than 1 period. Thus we take the general integral for this function between $(-\pi, \pi)$ and find that the total energy of this function is proportional to:

$$E_{tot} = \int_{-\pi}^{\pi} |f_s(x)|^2 dx = \int_{-\pi}^{\pi} (\cos(x) - s)^4 dx = \frac{1}{4}\pi(3 + 8s^2(3 + s^2)). \tag{2.27}$$

Now that we know the energy in a full period, the superoscillatory region then

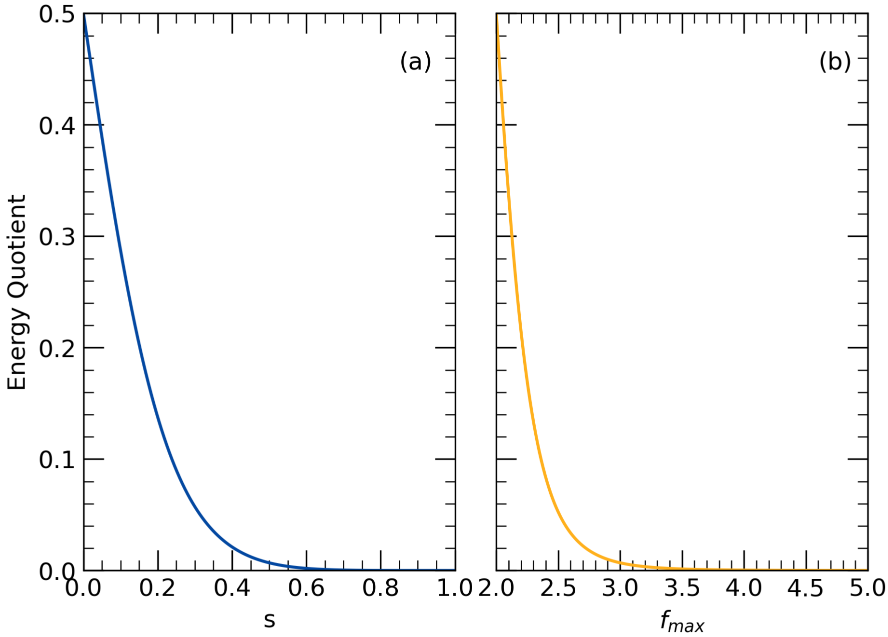

Figure 2.4: Energy Quotient plots with respect to (a) the superoscillating variable s and (b) the superoscillating frequency f. Plot (b) has an origin at $f = 2$ as below this value it would not correspond to valid values of s and as such there is a divergence beyond $f = 2$

contains;

$$E_{SO} = \int_{-\cos^{-1}(s)}^{\cos^{-1}(s)} (\cos(x) - s)^4 dx = \\ 3(3 + 8s^2(3 + s^2))\cos^1(s) - \frac{1}{12}(5s(11 + 10s^2)\sqrt{1 - s^2}) \tag{2.28}$$

but it is more usefully expressed as a quotient of the total energy in the period:

$$E_Q = \frac{E_{SO}}{E_{tot}} = \frac{1}{\pi}\cos^{-1}(s) - \frac{5s(11 + 10s^2)\sqrt{1 - s^2}}{3\pi((3 + 8s^2(3 + s^2)))}, \tag{2.29}$$

which has limits of $\frac{1}{2}$ at $s = 0$ and 0 at $s = 1$. These limits make sense, as the $s \to 0$ limit corresponds to a recovery of the function $\cos^2(x)$ and thus does not superoscillate so half of the energy is contained within half the period, and for $s \to 1$ as, there is no superoscillation, indeed there is no oscillation, as $\lambda_{loc} = 0$. The plot of this function (2.29) can be seen in figure 2.4. As can clearly be seen there is a dramatic decay of energy in the superoscillatory region as s increases, and ,correspondingly, the superoscillatory frequency increases. As an example, if we

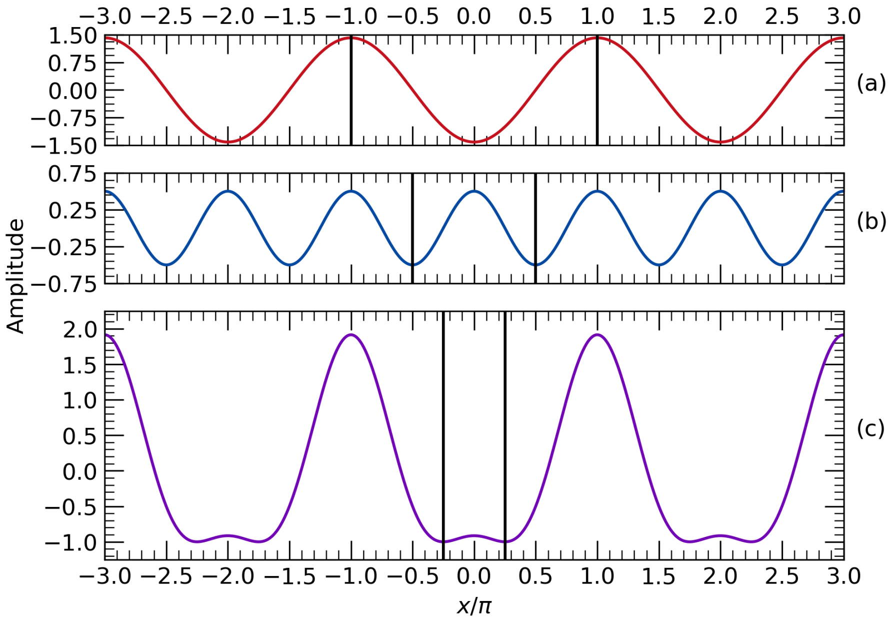

Figure 2.5: A plot of $f_{\frac{\sqrt{2}}{2}}(x)$ which corresponds to a superoscillating frequency double that of the Fourier limit. Here $f_{max} = 4$

were aiming to cause a superoscillation double that of the Fourier limit frequency, i.e. $f_{max} = 4$, then the energy quotient would be just 6.93×10^{-5}. The plot of this function can be seen in figure (2.5) where it is clear that a frequency doubling in the superoscillatory region leads to both enormous amplitude suppression, and energy quotient suppression.

If we wanted to look at the difference of amplitudes between the two regions, this is again relatively easy to compute. Since the maximas occur at $n\pi$ and superoscillations occur every $2m\pi$, the wings of the superoscillation occur at odd n values, so every $(2m+1)\pi$. Using these values in $f_s(x)$, the amplitude of the function at these points is $A_{SO} = f(2m\pi) = (1-s)^2$ and $A_{wing} = f([2m+1]\pi) = (-1-s)^2 = (1+s)^2$ since $0 < s < 1$ and thus the amplitude quotient is given by:

$$A_Q = \frac{A_{SO}}{A_{wing}} = \frac{(1-s)^2}{(1+s)^2} \tag{2.30}$$

This function is then plotted in figure (2.6) and we can once again see the decay of

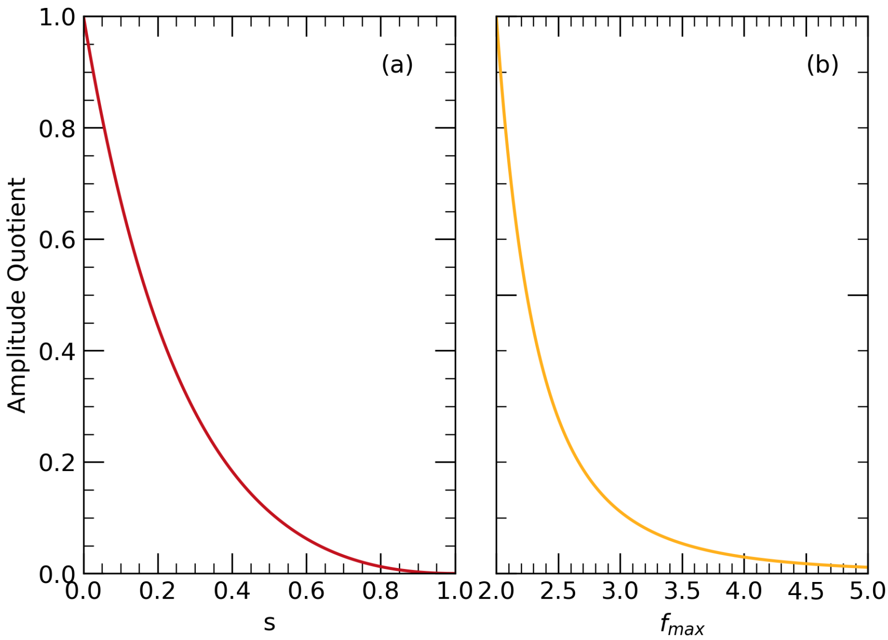

Figure 2.6: Amplitude Quotient plots with respect to (a) the superoscillating variable s and (b) the superoscillating frequency f. Plot (b) has an origin at $f = 2$ as below this it would not correspond to valid values of s and as such there is a divergence beyond $f = 2$

amplitude with increasing s and therefore f.

These energy and amplitude quotients are a good means of measuring the cost of increasing the superoscillating frequency with the trade-offs between amplitude and energy. If we calculate the amplitude quotient for frequency doubling as we have the energy quotient, we find that the amplitude quotient is $A_Q = 0.029$.

This notion is similar to the conclusions drawn by Konrad and Roux in [24], where they state that as superoscillating frequencies increase, the feasibility of superoscillations above a 1 order of magnitude increase is so exponentially suppressed as to be very improbable. If we were to examine the amplitude quotient and energy quotient of this, we find that the energy quotient is given by $E_Q = 1.1 \times 10^{-10}$ and the amplitude quotient is given by $A_Q = 3.8 \times 10^{-5}$. As we can see this is a vastly suppressed system, and if we take E_Q to be an analogue of the detectability, then the detectability of the superoscillation is 1×10^{-10} smaller than that of the wings of the superoscillation, making it very hard to detect.

Thus we have developed tools to help analyse and characterise parts of signals and superoscillations as well as examining a specific example of a superoscillating function, characterising its behaviour, and analysing it using those same tools. From this we have found that at least in the case of the basic superoscillating function $(\cos(x) - s)^2$ the same conclusions can be drawn as from Konrad and Roux [24] that the feasibility, detectability and amplitude of superoscillations decrease exponentially with increasing frequency. Specifically, that doubling the frequency leads to a detectability of roughly 7×10^{-5} and increasing the frequency by an order of magnitude leads to a detectability of 1×10^{-10}, which indicates an increasingly small likelihood of the superoscillation being sensed. This conclusion is further supported in [9] where it is postulated that in superoscillations, the frequency and amplitude can be considered a Fourier pair, whereby an inequality can be set up relating the two, such that we can exchange amplitude for frequency in a way that we can beat the traditional frequency limits.

2.4 Aharonov Superoscillations

In the previous section we looked at a particular superoscillating function $[\cos(x) - s]^2$, in this section we discuss a larger family of superoscillating functions and their associated Fourier series. One of the most studied superoscillating functions is given by,

$$f_n(x) = [\cos(\omega_n x) - ia\sin(\omega_n x)]^n, \tag{2.31}$$

in which: $n \in \mathbb{N}$; ω_n are frequency functions with arbitrary dependence on n; and a is the superoscillatory factor. Aharonov, in [20], decomposes this function into a

Fourier series as,

$$f_n(x) = \sum_{j=0}^{n} X_j e^{ih_j x}, \tag{2.32}$$

where:

$$X_j = \prod_{\substack{k=0 \\ k\neq j}}^{n} \frac{h_k - a}{h_k - h_j}; \tag{2.33}$$

n is the number of Fourier frequencies; h_j are normalised Fourier frequencies such that $h_j \in [-1, 1]$; and thus $a \in (1, \infty)$. If we take the limit of $n \to \infty$ the function converges to:

$$\lim_{n\to\infty} f_n(x) = e^{iax} \tag{2.34}$$

As such we can apply the tools we have developed to discuss superoscillations to this function, and analyse the results. Applying the local frequency equation from equation 2.22 to equation 2.31 we get that the turning points of the function are given by the solutions to the following:

$$\frac{df_n(x)}{dx} = -n\omega_n \left[\sin(\omega_n x) + ia\cos(\omega_n x)\right]\left[\cos(\omega_n x) - ia\sin(\omega_n x)\right]^{n-1} = 0 \tag{2.35}$$

thus, we need to solve each bracket for zero with their solutions being x_0 and x_1 respectively;

$$x_0 = \frac{i}{2\omega_n}\left(\ln\left[\frac{1-a}{1+a}\right]\right); \tag{2.36}$$

and

$$x_1 = \frac{i}{2\omega_n}\left(\ln\left[\frac{1+a}{a-1}\right]\right). \tag{2.37}$$

Therefore, to find the local frequency we need the distances between these zeroes, given by, $|x_0 - x_1|$, which results in;

$$\Delta x_0 = \left| \frac{i}{2\omega_n} \left(\ln \left[\frac{1-a}{1+a} \right] \right) - \frac{i}{2\omega_n} \left(\ln \left[\frac{1+a}{1-a} \right] \right) \right| \tag{2.38}$$

which is:

$$\Delta x_0 = \left| \frac{i}{2\omega_n} \left[2 \ln \left(\frac{a-1}{1+a} \right) + (3p - 2q)\pi i \right] \right| \tag{2.39}$$

where $p, q \in \mathbb{Z}$ are to distinguish between different zeroes from x_0 and x_1 respectively. Since we want to find the smallest possible value of Δx we need to minimize equation 2.40 by setting $p = q = 0$ which leads to a simplification of Δx to:

$$\Delta x_0 = \left| \frac{i}{2\omega_n} \left[2 \ln \left(\frac{a-1}{1+a} \right) \right] \right| = \frac{1}{\omega_n} \left| \ln \left(\frac{a-1}{1+a} \right) \right| . \tag{2.40}$$

Finally, we can find the local frequency by the equation $f = \frac{2\pi}{\Delta x}$ resulting in our final local frequency equation being:

$$f_{loc} = \frac{2\pi\omega_n}{\left| \ln \left(\frac{a-1}{1+a} \right) \right|} \tag{2.41}$$

This is a very interesting result, as ω_n is related to the maximum Fourier frequency, and so we get our local frequency in terms of the maximum Fourier frequency, and related by the superoscillating frequency a. This relationship is due to the polynomial nature of the superoscillating function described in equation 2.31. As we expand the polynomial in a binomial fashion, our first term will become $\cos^N(\omega_n x)$, this can be further expanded into:

$$\cos^N(\omega_n x) = \frac{1}{2^N} \sum_{k=0}^{N} \binom{N}{k} e^{i\omega_n (2k-N)x} \tag{2.42}$$

which has a maximum frequency component, as can be seen in the exponent, at $k = 0$ and thus $N\omega_n$. Here ω_n is a constant that relates the polynomial order of the superoscillating function in equation 2.31 to the Fourier frequency decomposition of said function, those frequencies being the $\{h_j\}$ set. The idea of equation 2.42 is to demonstrate how the polynomial cos() function expands into different frequency components, given by $e^{i\omega_n(2k-N)x}$. These frequency components are contained within the $\{h_j\}$ Fourier frequency set. If we set the polynomial order of the cos equal to the polynomial order of the superoscillating function, so $N = n$, then we can begin to analyse what the highest frequency component of the superoscillating function will be in terms of ω_n and n. This becomes $\max(\{h_j\}) = N\omega_n = n\omega_n$ So we want to know when does $f_{loc} > max(\{h_j\})$? Since we have separate equations describing both sides, we use them in this inequality:

$$\frac{2\pi\omega_n}{\left|\ln\left(\frac{a-1}{1+a}\right)\right|} > n\omega_n \ , \tag{2.43}$$

which, given that we can assume $\omega_n \in \mathbb{R}^+$ because of the way it is used in equation 2.31, gives an upper limit to what the polynomial order n should be in terms of the superoscillating frequency a. This inequality is given by:

$$n < \frac{2\pi}{\left|\ln\left(\frac{a-1}{1+a}\right)\right|} \ , \tag{2.44}$$

and shows that as a increases, so too does the upper bound of n. Given that we want to have as accurate a representation as possible, and that increasing n increases the superoscillatory region [24], we want n to be the largest integer smaller than $\frac{2\pi}{\left|\ln\left(\frac{a-1}{1+a}\right)\right|}$.

Now performing similar calculation to what we did in the previous subsection, we can begin to investigate the energy ratios and the amplitude ratios for this function. These will take on a different shape to the basic superoscillatory function that we saw in equation 2.16. If we investigate the limits of the Aharonov functions, we can start to get an idea of how the different energy and amplitude curves behave. It is clear that from equation 2.34 there is a limit as $n \to \infty$ and so investigating the behaviour of the energy and amplitude curves for this limit is important. The

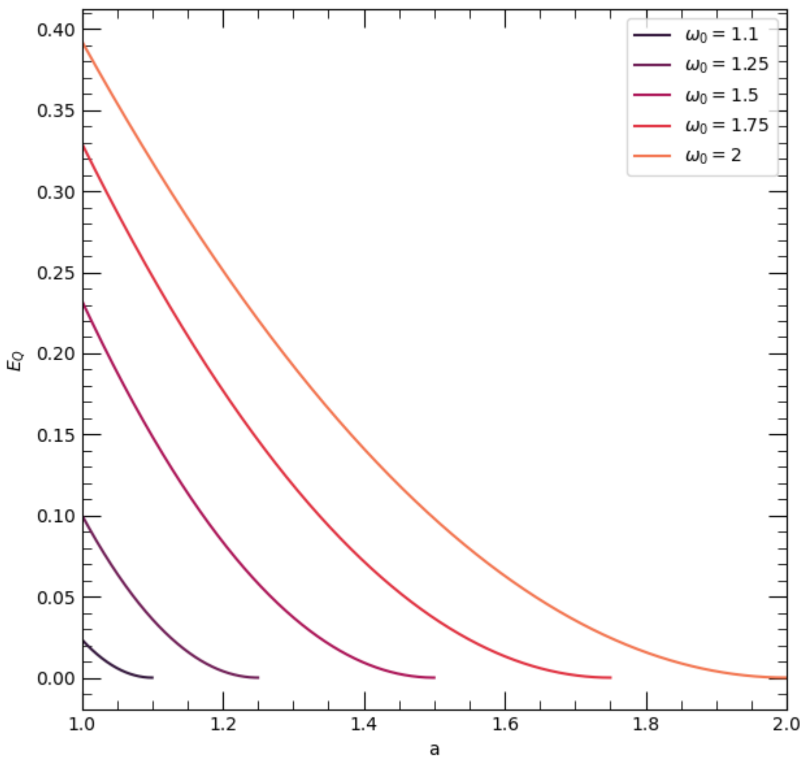

Figure 2.7: An energy quotient curve showing the relationship between the super-oscillating variable a and E_Q for $n = 1$

energy curve is relatively simple. That is because in the limit of $n \to \infty$ there is no non-superoscillatory region, the entire function is superoscillatory. Therefore, the energy curve is constant, as $E_{SO} = E_{tot}$ and each superoscillation contains $\frac{2\pi}{a}$ of the energy per period. The amplitude quotient is also relatively simple. As there are no wings of the superoscillatory region, there is no A_{wing} and so this is undefined.

However, if we look at the other end of the spectrum for $n = 1$, the lowest number that n can take, the behaviour is very different. Using Aharonov's expansion for $n = 1$,

$$f_1(x) = \sum_{j=0}^{1} X_j e^{ih_j x} = \left[1 - \frac{a}{h_1 - h_0}\right] \left[e^{ih_0 x} - e^{ih_1 x}\right] , \tag{2.45}$$

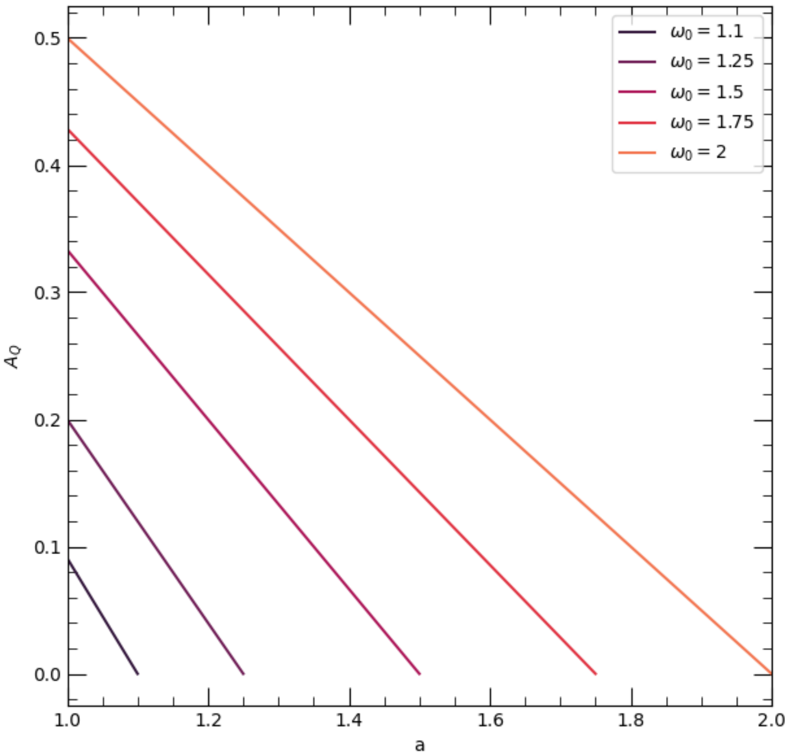

Figure 2.8: A figure showing the amplitude curves for different bandwidths ω_0 for the $n = 1$ Aharonov superoscillations.

this has zero points at $\frac{2n\pi}{h_1 - h_0}$ and has an absolute square value of:

$$|f_1(x)|^2 = 2\left[1 - \frac{a}{h_1 - h_0}\right]^2 \left[1 - \cos\left([h_1 - h_0]x\right)\right] . \tag{2.46}$$

Calculating the energy between two zero points is given by:

$$2\left[1 - \frac{a}{h_1 - h_0}\right]^2 \int_0^{\frac{2\pi}{h_1 - h_0}} \left(1 - \cos\left([h_1 - h_0]x\right)\right) dx = \frac{2\pi}{h_1 - h_0}\left[1 - \frac{a}{h_1 - h_0}\right]^2 . \tag{2.47}$$

As can be seen this leads to a quadratic relation and we know that $a > 1$ and $h_1, h_0 \in [-1, 1]$ thus the maximum difference between h_0 and h_1 is 2. We also know that the maximum that a can be is given by ω_0, or the bandwidth of the system. Given that the difference between $\Delta h_{ij} = h_i - h_j$ is the bandwidth for $n = 1$ and

$a \in (1, \Delta h_{ij}]$ this necessitates that $\Delta h_{ij} > 1$. Therefore, each energy curve is unique for each of the Δh_{ij} and these can be seen in figure 2.7

As can be seen in both equation 2.47 and figure 2.7, it takes a quadratic form, however, as we increase n, the polynomial order of the energy quotient goes as $2n$. this means that as the number of frequencies,n, involved goes up, the quicker the energy quotient will decrease, as the gradients become increasingly steep of $E_Q(a) \propto a^{2n}$.

The amplitude quotient for $n = 1$ is given merely by the coefficient here, as seen in figure 2.8, and thus follows a negative linear curve. As the number of frequencies n increases, then the amplitude quotient will have a more complex relationship, but will be of highest polynomial order n. As has been seen before, the limit of this behaviour, as $n \to \infty$ leads to $A_Q = 1 \ \forall a$.

2.4.1 Aharonov Supershift

Also in Aharonov's paper on new methods for creating superoscillatory patterns [20] he discusses using a similar technique for functions beyond the complex propagator, e^{ikx}. Indeed, he shows that it is possible to construct superoscillations out of any oscillatory function given a few caveats. This is shown in Theorem 4.6 in Aharonov's paper [20]. To make the theorem clear for our use, we restate it here. The first caveat is that the basis oscillatory functions $G(x)$ need to have infinite derivatives at the origin, and that their derivatives are non zero. This is to satisfy the governing equation, which is similar to the approach we took previously in section 2.4:

$$f_n^{(p)}(0) = (a)^p G^{(p)}(0) \tag{2.48}$$

where (p) denotes the p^{th} derivative of a function, and $a \in \mathbb{R}$ is our superoscillatory variable, and n $|a| > 1$. Given these conditions that there $\exists \ G^{(p)}(0) \neq 0 \quad \forall p =$

$0, 1, ...n$, then we can consider a set of points $h_j(n) \in [-1, 1]$, with $j = 0, 1, ...n$ and $n \in \mathbb{N}$, there exists a unique solution $Y_j(n)$ to satisfy the above condition, such that:

$$Y_j(n) = \prod_{\substack{k=0 \\ k \neq j}}^{n} \left(\frac{h_k(n) - a}{h_k(n) - h_j(n)} \right) \ . \tag{2.49}$$

This is extremely similar to the construction seen in equation 2.33 for the Aharonov coefficients. In fact, this similar construction leads to similar outcomes, as the function $f_n(x)$ becomes:

$$f_n(x) = \sum_{j=0}^{n} \prod_{\substack{k=0 \\ k \neq j}}^{n} \left(\frac{h_k(n) - a}{h_k(n) - h_j(n)} \right) G(h_j(n)x), \ x \in \mathbb{R} \tag{2.50}$$

and in the limit of $n \to \infty$:

$$\lim_{n \to \infty} f_n(x) = G(ax), \ x \in \mathbb{R} \tag{2.51}$$

which mimics the Aharonov generating equations as before. Essentially, in the limit of infinite frequencies or bandwidths, $n \to \infty$, we can cause a supershift from the bandlimited region of $h_j \in [-1, 1]$ in frequency space to a function that would have a frequency space of $[-a, a]$. This method allows us to expand our possible range of functions that we can use to include functions that have infinite, but bandlimited Fourier domains. One such important function is the $\text{sinc}(x)$ function, as it is used in the diffraction of slit apertures, which are the main examples that we will be looking at in this thesis. When we deal with these types of infinite, but bandlimited Fourier domains, it is said that the Foruier domain of $\hat{f}_n(\omega)$ permits a supershift in ω, if the condition in equation 2.51 is met, that of the infinite limit converging to the supershifted function $G(ax)$.

Chapter 3

Apertures

In this chapter, we consider the design theory behind creating superoscillating apertures. The general methodology used in this chapter is to take the Fourier transform of the transmission function and using Aharonov's supershift principles and some equations detailed in the following sections to calculate offsets for a given set of slit widths.

3.1 Slit Apertures

To examine diffraction through an array of slits it is useful to turn to Fourier optics and use a transparency function. The transparency function we examine will utilise a binary method to distinguish between materials, a transparent "open" part and an opaque "closed" part. This will be achieved using the rectangular function, $Rect\left(x\right)$ function, which is defined as,

$$Rect\left(\frac{x-c}{\beta}\right) = \begin{cases} 1, & \text{if } \ c-\frac{\beta}{2} \leq x \leq c+\frac{\beta}{2} \\ 0, & \text{otherwise} \end{cases}, \tag{3.1}$$

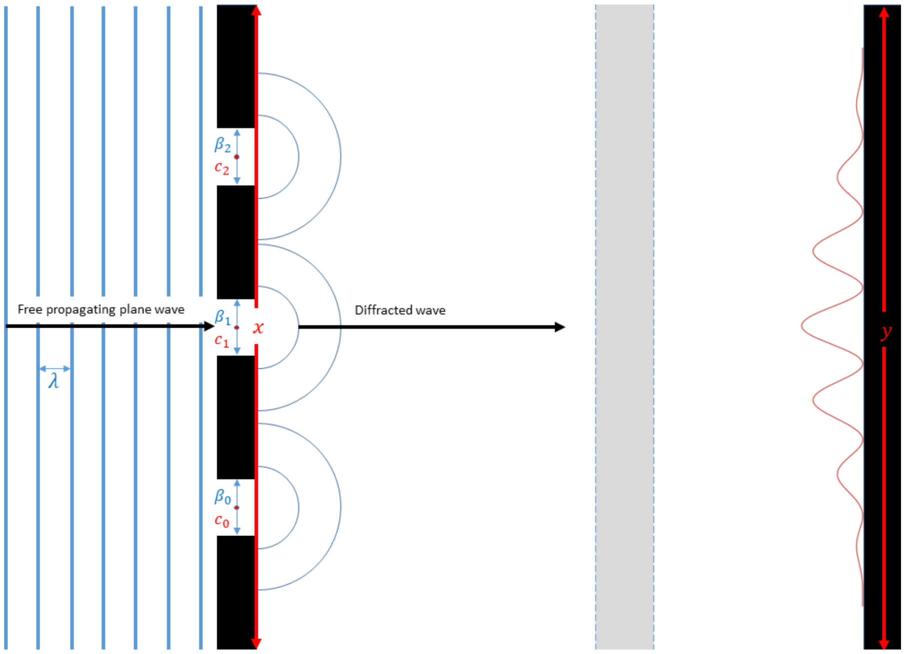

Figure 3.1: A figure showing the system for approximation by Fourier optics. A plane wave of wavelength λ illuminates an aperture array in the plane $\{z_0, x\}$ and is then diffracted across a distance L, (which is large compared with the wavelength and shown by the white space and the grey area bounded by blue dashed lines between the planes), and is measured at the diffraction plane at $\{z_1, y\}$. In this the β_j and c_j are as defined in equation 3.1, and x and y are parallel but separated by $z_1 - z_0 = L$.

where c is the central position of the aperture, β is the width of the slit and x is a coordinate describing the aperture array plane. We don't consider the other dimension, the one that would be out of the plane of the page, as, for the slit apertures, it is very large compared to the wavelength. To give a concrete physical interpretation of this mathematical formulation, we can turn to figure 3.1 to see what the system looks like. In this figure, a plane wave of wavelength λ illuminates an aperture array in the plane $\{z_0, x\}$ and is then diffracted across a distance L, (which is large compared with the wavelength and shown by the white space and the grey area bounded by blue dashed lines between the planes), and is measured at the diffraction plane at $\{z_1, y\}$. In figure 3.1 β_j and c_j are as defined in equation 3.1, and x and y are parallel but separated by $z_1 - z_0 = L$.

To use Fourier Optics we then perform the Fourier transform on this arbitrary

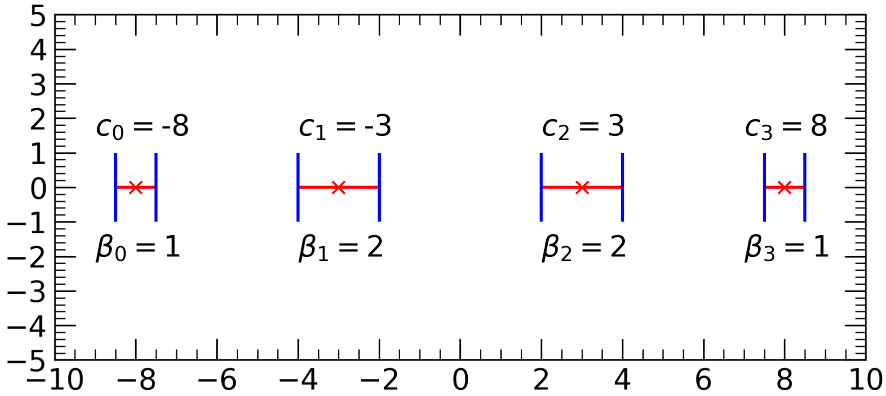

Figure 3.2: A diagram depicting a set of $\{c_j\}_j$ and $\{\beta_j\}_j$ as an example and demonstration of the constraint requirements detailed in equation 3.3 and below

aperture array transparency function. This is constructed as:

$$T(x) = \sum_{j=0}^{N} Rect\left(\frac{x - c_j}{\beta_j}\right) \ , \tag{3.2}$$

where c_j are defined so that $(\forall j \in \mathbb{N})$ they non-overlapping:

$$c_{j+1} > c_j + \frac{1}{2}(\beta_j + \beta_{j+1}) \ . \tag{3.3}$$

Whereas β_j has fewer constraints on it. They must be real and positive, $\beta_j \in \mathbb{R}^+$, due to the constraints on the ordering of c_j

The reason for these conditions is for clarity and simplicity, as although it should be possible to account for overlapping apertures, this simplifies the task without double counting issues arising from other constructions. For a clear picture, figure 3.2 shows the region and demonstrates the need for the constraints on both c_j and β_j. To begin finding the diffraction pattern, we perform the Fourier transform:

$$\mathscr{F}\left(T(x)\right) = \int_{-\infty}^{\infty} dx \ T(x) e^{ik'x} \ , \tag{3.4}$$

where here $\mathscr{F}$ denotes the Fourier transform, and we use the arbitrary nature of k' to set it to $k' = \frac{2\pi y}{L\lambda}$ in order to retrieve the diffraction pattern along the axis y. The new variable y is, as shown in figure 3.1, parallel to x separated by some distance L. Performing the Fourier transform for our transmission function:

$$\mathscr{F}\left(T(x)\right) = \int_{-\infty}^{\infty} dx\ e^{i\frac{2\pi y}{L\lambda}x} \sum_{j=0}^{N} Rect\left(\frac{x - c_j}{\beta_j}\right) . \tag{3.5}$$

As the $Rect(x)$ function is defined in Equation (3.1) we can see that it is constant throughout its span, except at its limits, where it takes on a zero value. As such we can make the interchange of summation and integration under the uniform convergence theorem [25],

$$\mathscr{F}\left(T(x)\right) = \sum_{j=0}^{N} \int_{-\infty}^{\infty} dx\ e^{i\frac{2\pi y}{L\lambda}x} Rect\left(\frac{x - c_j}{\beta_j}\right) , \tag{3.6}$$

which given that the $Rect(x)$ function is constant between its limits and zero elsewhere, the integral can then be given by:

$$\mathscr{F}\left(T(x)\right) = \sum_{j=0}^{N} \int_{c_j-\frac{\beta_j}{2}}^{c_j+\frac{\beta_j}{2}} dx\ e^{i\frac{2\pi y}{L\lambda}x} . \tag{3.7}$$

This has a relatively simple form when integrated:

$$\mathscr{F}\left(T(x)\right) = \sum_{j=0}^{N} \left[\frac{1}{i\frac{2\pi y}{L\lambda}} e^{i\frac{2\pi y}{L\lambda}x}\right]_{c_j-\frac{\beta_j}{2}}^{c_j+\frac{\beta_j}{2}} \tag{3.8}$$

. This then evaluates to;

$$\mathscr{F}\left(T(x)\right) = \sum_{j=0}^{N} \left[\left(\frac{1}{i\frac{2\pi y}{L\lambda}} e^{i\frac{2\pi y}{L\lambda}\left(c_j+\frac{\beta_j}{2}\right)}\right) - \left(\frac{1}{i\frac{2\pi y}{L\lambda}} e^{i\frac{2\pi y}{L\lambda}\left(c_j-\frac{\beta_j}{2}\right)}\right)\right] , \tag{3.9}$$

which then simplifies to,

$$\sum_{j=0}^{N} \frac{1}{i\frac{2\pi y}{L\lambda}} e^{i\frac{2\pi y}{L\lambda}c_j} \left[e^{i\frac{2\pi y}{L\lambda}\left(\frac{\beta_j}{2}\right)} - e^{-i\frac{2\pi y}{L\lambda}\left(\frac{\beta_j}{2}\right)} \right] = \sum_{j=0}^{N} \frac{\sin\left(\frac{\pi y}{L\lambda}\beta_j\right)}{\frac{\pi y}{L\lambda}} e^{i\frac{2\pi y}{L\lambda}c_j} \ . \tag{3.10}$$

Thus we retrieve the well known result:

$$E(y) = \sum_{j=0}^{N} \beta_j \operatorname{sinc}\left(\frac{\pi y}{L\lambda}\beta_j\right) e^{i\frac{2\pi y}{L\lambda}c_j} \ . \tag{3.11}$$

As we are looking for the intensity profile to superoscillate, we use the fact that $I(y) = |E(y)|^2 = E(y)E^*(y)$ where $E^*(y)$ denotes the complex conjugate of $E(y)$. Finding the complex conjugate of $E(y)$,

$$E^*(y) = \sum_{j=0}^{N} \beta_j \operatorname{sinc}\left(\frac{\pi y}{L\lambda}\beta_j\right) e^{-i\frac{2\pi y}{L\lambda}c_j} \ , \tag{3.12}$$

then multiplying the two equations together,

$$\begin{aligned} E(y)E^*(y) = &\left(\sum_{j=0}^{N} \beta_j \operatorname{sinc}\left(\frac{\pi y}{L\lambda}\beta_j\right) e^{i\frac{2\pi y}{L\lambda}c_j}\right) \cdot \\ &\left(\sum_{m=0}^{M} \beta_m \operatorname{sinc}\left(\frac{\pi y}{L\lambda}\beta_m\right) e^{-i\frac{2\pi y}{L\lambda}c_m}\right) \ , \end{aligned} \tag{3.13}$$

which can be simplified by $M = N$ (as there are the same number of apertures in the complex conjugate as the original function) resulting in:

$$I(y) = \sum_{j,m=0}^{N} \beta_j\beta_m \operatorname{sinc}\left(\frac{\pi y}{L\lambda}\beta_j\right) \operatorname{sinc}\left(\frac{\pi y}{L\lambda}\beta_m\right) e^{i\frac{2\pi y}{L\lambda}[c_j - c_m]} \ . \tag{3.14}$$

This result can actually be simplified further by considering the terms where $m = j$, we can see there should be a simplification as $c_j - c_m = 0$, and also the terms where $j \neq m$ but are variations of each other, for example, when the $c_j - c_m = -[c_{j'} - c_{m'}]$, whcih reduces the cross terms to a cos() interference term.

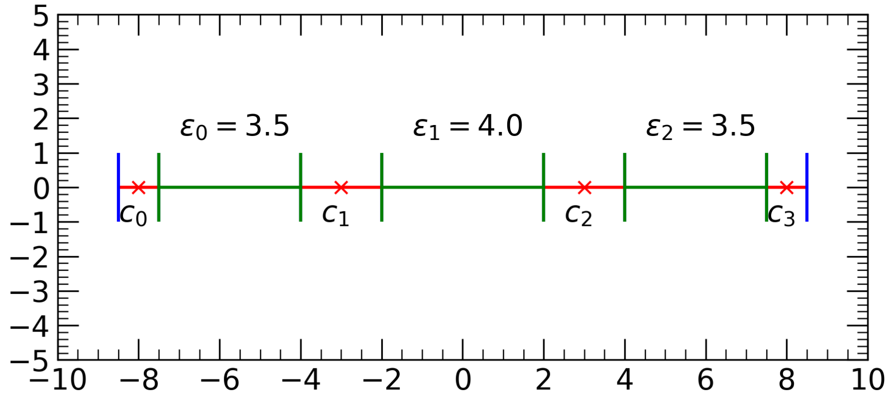

Figure 3.3: A figure depicting the definition of ϵ_k (green line) and how it relates to c_j (red cross) and β_j (red line)

Thus, the equation now has $N+1$ terms that have no interference terms, and $\frac{N(N+1)}{2}$ interference terms. As such we can rewrite equation (3.14) as follows,

$$\begin{aligned} I(y) = \sum_{j=0}^{N} \beta_j \operatorname{sinc}\left(\frac{\pi y}{L\lambda}\beta_j\right) \Bigg[\beta_j \operatorname{sinc}\left(\frac{\pi y}{L\lambda}\beta_j\right) + \\ 2\sum_{m=j+1}^{N} \beta_m \operatorname{sinc}\left(\frac{\pi y}{L\lambda}\beta_m\right) \cos\left(\frac{2\pi y}{L\lambda}[c_j - c_m]\right) \Bigg] . \end{aligned} \tag{3.15}$$

Both equation (3.14) and (3.15) are the full intensity profile of an arbitrary slit aperture of non-overlapping slits of arbitrary width and position. Due to c_j's constraints we can build a relationship between c_j and c_0. This is because we know that $c_{j+1} > c_j + \frac{1}{2}(\beta_j + \beta_{j+1})$, thus $\forall j > 0$;

$$c_j > c_0 + \sum_{k=1}^{j} \frac{1}{2}(\beta_k + \beta_{k-1}) \ . \tag{3.16}$$

We can then account for the differences between an inequality and equality by introducing a variable that measures the difference (distance) between the non-overlapping apertures, ϵ,

$$c_j = c_0 + \sum_{k=1}^{j} \epsilon_k + \frac{1}{2}(\beta_k + \beta_{k-1}) \ . \tag{3.17}$$

This new ϵ, as seen in figure 3.3, can change for every aperture but to simplify equation (3.15) we can retrieve the following relationship for $c_j - c_m$, $\forall m \leq j$,

$$c_j - c_m = \sum_{k=m+1}^{j} \epsilon_k + \frac{1}{2}(\beta_k + \beta_{k-1}) \ . \tag{3.18}$$

3.2 Superoscillations in Slit Apertures

In order to cause superoscillations in the intensity profile, we have to know the spatial frequencies involved in the intensity pattern. The way that we do this is classically via the Fourier Transform. The Fourier Transform of the intensity profile given in equations (3.14,3.15) can be calculated by exploiting some properties of the Fourier Transform.

3.2.1 Fourier Property Method

We exploit a useful property of the Fourier transform to answer the question of what spatial frequencies are involved in the intensity pattern. It is important to note that in this section the $\frac{2\pi}{L\lambda}$ has been dropped to work in the natural units of the system. However, the ease of re-introduction of this constant is shown in equation (3.33) First, let us examine the question that we are trying to solve:

$$\mathscr{F}(I(y)) = \mathscr{F}(E(y)E^*(y)) = \mathscr{F}(E(y)) * \mathscr{F}(E^*(y)) \ , \tag{3.19}$$

where $f * g(x)$ denotes a convolution of f and g. Given that each $E(y)$ is itself a Fourier transform, we get,

$$\mathscr{F}(I(y)) = \mathscr{F}(\mathscr{F}(T(x))) * \mathscr{F}(\mathscr{F}(T(x))^*) \ , \tag{3.20}$$

where $T(x)$ is our transparency function as defined in equation (3.2), which is completely real. As such we can exploit another property of the Fourier transform, that of:

$$\mathscr{F}(f(-x)) = (\mathscr{F}(f(x)))^* \ . \tag{3.21}$$

This then allows us to simplify equation (3.22),

$$\mathscr{F}(I(y)) = \mathscr{F}(\mathscr{F}(T(x))) * \mathscr{F}(\mathscr{F}(T(-x))) \ , \tag{3.22}$$

and thus, since applying the Fourier transform twice a time reversal occurs, $\mathscr{F}(\mathscr{F}(f(x))) = 2\pi f(-x)$ leading to,

$$\mathscr{F}(I(y))(k) = 4\pi^2 T(-x) * T(x) = 4\pi^2 \int_{-\infty}^{\infty} T(-\tau)T(\tau - k)d\tau \ . \tag{3.23}$$

We then substitute $T(x)$ from equation (3.2),

$$\mathscr{F}(I(y))(k) = 4\pi^2 \int_{-\infty}^{\infty} \sum_{j=0}^{N} Rect\left(\frac{-\tau - c_j}{\beta_j}\right) \sum_{m=0}^{N} Rect\left(\frac{\tau - c_m}{\beta_m} - k\right) d\tau \ . \tag{3.24}$$

This can be simplified much the same as we did for the Fourier transform in equation (3.7), but taking care due to the negative τ flipping the limits and making them negative,

$$\mathscr{F}(I(y))(k) = 4\pi^2 \sum_{j=0}^{N} \int_{-c_j - \frac{\beta_j}{2}}^{-c_j + \frac{\beta_j}{2}} \sum_{m=0}^{N} Rect\left(\frac{\tau - c_m}{\beta_m} - k\right) d\tau \ . \tag{3.25}$$

Taking the summations outside of the integral,

$$\mathscr{F}(I(y))(k) = 4\pi^2 \sum_{j,m=0}^{N} \int_{-c_j - \frac{\beta_j}{2}}^{-c_j + \frac{\beta_j}{2}} Rect\left(\frac{\tau - c_m}{\beta_m} - k\right) d\tau \ . \tag{3.26}$$

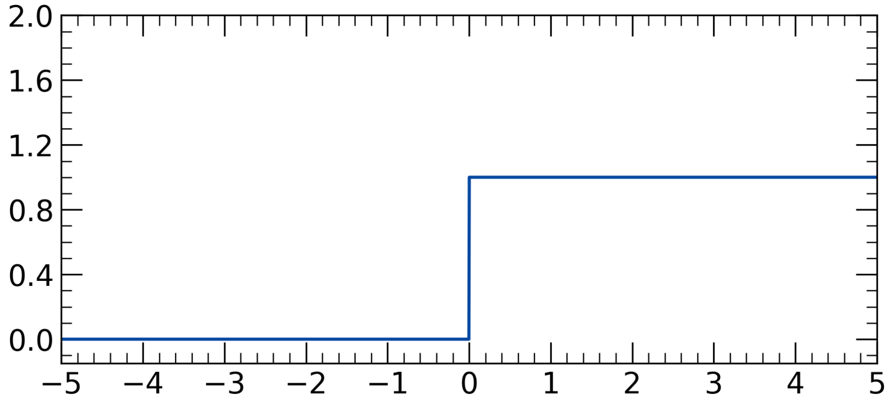

Figure 3.4: This figure depicts a Heaviside step function as described in equation 3.27.

We exploit a result of the convolutions of boxcar functions [26] (a slightly more general rectangle function) which relies on the limits of each rectangle function. In order to do this we must first define the Heaviside step function:

$$H(x) = \begin{cases} 0 & x < 0 \\ & \\ 1 & x \geq 0 \end{cases} \quad , \tag{3.27}$$

this function can be seen in figure 3.4. Thus the convolution of the boxcar functions becomes:

$$\begin{aligned} \mathscr{F}(I(y))(k) = 4\pi^2 \sum_{j,m=0}^{N} & \\ \Bigg[\left(k - \left[-c_j - \frac{\beta_j}{2} \right] - \left[c_m - \frac{\beta_m}{2} \right] \right) & H \left(k - \left[-c_j - \frac{\beta_j}{2} \right] - \left[c_m - \frac{\beta_m}{2} \right] \right) \\ - \left(k - \left[-c_j + \frac{\beta_j}{2} \right] - \left[c_m - \frac{\beta_m}{2} \right] \right) & H \left(k - \left[-c_j + \frac{\beta_j}{2} \right] - \left[c_m - \frac{\beta_m}{2} \right] \right) \\ - \left(k - \left[-c_j - \frac{\beta_j}{2} \right] - \left[c_m + \frac{\beta_m}{2} \right] \right) & H \left(k - \left[-c_j - \frac{\beta_j}{2} \right] - \left[c_m + \frac{\beta_m}{2} \right] \right) \\ + \left(k - \left[-c_j + \frac{\beta_j}{2} \right] - \left[c_m + \frac{\beta_m}{2} \right] \right) & H \left(k - \left[-c_j + \frac{\beta_j}{2} \right] - \left[c_m + \frac{\beta_m}{2} \right] \right) \Bigg] \quad , \end{aligned} \tag{3.28}$$

which if we gather centre positions and width terms together becomes,

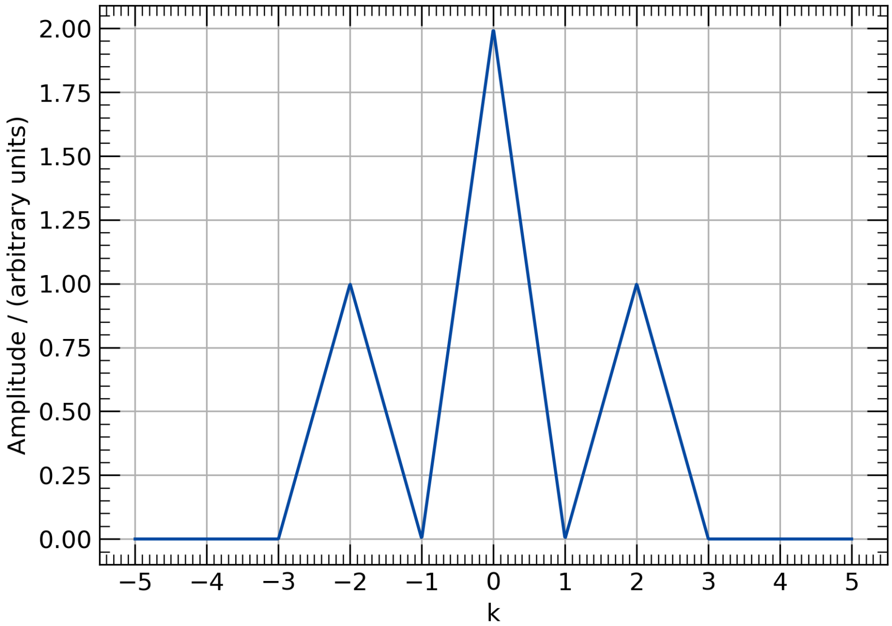

Figure 3.5: An illustration of a basic convolution as described in equation 3.29 this is the convolution of two equal width slits with $\beta = \{1, 1\}$ and $c = \{-1, 1\}$ with both β and c are in arbitrary units

$$\begin{aligned}\mathscr{F}(I(y))(k) = 4\pi^2 \sum_{j,m=0}^{N} \\ \Bigg[\left(k + [c_j - c_m] + \frac{1}{2}[\beta_j + \beta_m]\right) H \left(k + [c_j - c_m] + \frac{1}{2}[\beta_j + \beta_m]\right) \\ - \left(k + [c_j - c_m] - \frac{1}{2}[\beta_j - \beta_m]\right) H \left(k + [c_j - c_m] - \frac{1}{2}[\beta_j - \beta_m]\right) \\ - \left(k + [c_j - c_m] + \frac{1}{2}[\beta_j - \beta_m]\right) H \left(k + [c_j - c_m] + \frac{1}{2}[\beta_j - \beta_m]\right) \\ + \left(k + [c_j - c_m] - \frac{1}{2}[\beta_j + \beta_m]\right) H \left(k + [c_j - c_m] - \frac{1}{2}[\beta_j + \beta_m]\right)\Bigg] .\end{aligned} \tag{3.29}$$

The total function described in 3.29 is constituent of basis functions similar to Figure 3.6. We can then simplify things by considering each element of this summation as its own function, $\Psi_{j,m}(x)$, and examining the behaviour of these functions at critical points. Here the Fourier transform becomes:

$$\mathscr{F}(I(y))(k) = \sum_{j,m=0}^{N} \Psi_{j,m}(k) \tag{3.30}$$

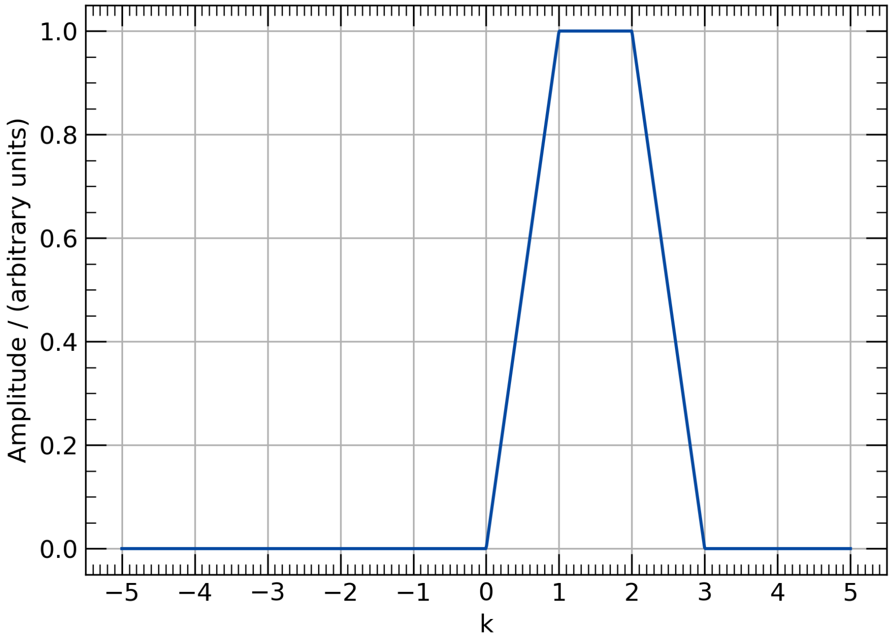

Figure 3.6: A function $\Psi_{j',m'}(k)$ with $c_{j'} - c_{m'} = -1.5$ and $\beta_{j'} = 1$, $\beta_{m'} = 2$

What this does show, is that there are infinite spatial frequencies involved in the diffraction, and as such we cannot consider the usual Aharonov functions when designing this array. Instead, as diffraction is still a band limited process, we have to use Aharonov's supershift principle [20] to try and construct superoscillatory diffraction patterns.

It is useful to discuss some of the properties of these $\Psi_{j,m}(x)$ functions. The first thing to note is that the maximum amplitude these functions take is always above the central point $c_j - c_m$. Second, the maximum amplitude that these functions achieve is limited by the smallest of β_j , β_m. Third, the non-zero x-limits of these functions are given by $x = c_m - c_j \mp \frac{1}{2}(\beta_j + \beta_m)$

3.2.2 Supershift

In order to cause a superoscillation, we have to know the maximum spatial frequency involved in the diffraction, and this is given by $k_{max} = \sup(\mathrm{supp}([\mathscr{F}(I(y))])$. Given that we have restricted what values c_j can take, we can make some assertions on what k_{max} can be. Due to the non-overlapping and ordered properties of c_j we can see that the largest difference between c_j's values will be $c_N - c_0$. For the width side of things, since we have already figured out what gives the largest frequency offset, and there is no slit redundancy, the choice of c forces our choice for β to be β_N and β_0. Thus the largest spatial frequency is then given by,

$$k_{max} = c_N - c_0 + \frac{1}{2}(\beta_N + \beta_0) \ , \tag{3.31}$$

or as given in Appendix 6.3,

$$k_{max} = \beta_0 + \sum_{l=1}^{N} \epsilon_l + \beta_l \ , \tag{3.32}$$

which is our band limit and largest Fourier component. This means that our super-oscillating frequency $g_{SO} > k_{max}$, which also translates to,

$$\lambda_{SO} < \lambda_{min} = \frac{L\lambda_{mat}}{k_{max}} \ , \tag{3.33}$$

where here λ_{mat} is the material wavelength. This result comes from bringing k_{max} back into the experimental coordinates system rather than the natural coordinates that are normally worked with, and therefore, $k_{max} = \frac{2\pi}{\lambda_{min}}$ If there are any features such that they are smaller than λ_{max} then it can be concluded that we have a superoscillation.

In order to construct the superoscillations via supershift, we look back to equations (3.14,3.15) and to the supershift section 2.4.1. From Aharonov's work [20], and as described in section 2.4.1, we see that we need to construct functions of the type:

$$\mathbb{A}(x) = \sum_{s=0}^{S} Y_s G(h_s x) \tag{3.34}$$

where $G(x)$ is an arbitrary oscillatory function that has the property of at least S

continuous derivatives at $x = 0$; h_s are an arbitrary set of frequencies, normalised to $h_s \in h \subset [-1, 1]$ and Y_s is defined in terms of h_s by,

$$Y_s = \prod_{\substack{t=0 \\ t \neq s}}^{S} \frac{h_t - g_{SO}}{h_t - h_s} \ . \tag{3.35}$$

We can then see that from equation (3.15), that $G(x)$, being arbitrary, can be defined in terms of the functions in the summation,

$$\begin{aligned} G_s(x) = \operatorname{sinc}\left(\frac{\pi x}{L\lambda}\beta_s\right) \Bigg[\beta_s \operatorname{sinc}\left(\frac{\pi x}{L\lambda}\beta_s\right) + \\ 2\sum_{m=s}^{N} \beta_m \operatorname{sinc}\left(\frac{\pi x}{L\lambda}\beta_m\right) \cos\left(\frac{2\pi x}{L\lambda}[c_s - c_m]\right)\Bigg] \ , \end{aligned} \tag{3.36}$$

leaving Y_s to be defined as,

$$Y_s = \beta_s \ , \tag{3.37}$$

when we evaluate at $G(0)$. All that needs to be done now is to determine what h_s are. However we have already shown what all of the frequencies in the equation are, back in equation 3.30, thus:

$$h_s(k) = \sum_{m=0}^{N} \Psi_{s,m}(k) \ . \tag{3.38}$$

However, as we are looking for the set $\{h_s\}_s$ to be a set of points in $[-1, 1]$ rather than a function of all k, we instead take the maximum of each h_s and subtract the minimum to find the bandwidth b_s, which should be unique for each s due to the uniqueness of c_s, so we define:

$$max(h_s) = \sup[h_s(k)] = c_N - c_s + \frac{1}{2}(\beta_s + \beta_N) \ . \tag{3.39}$$

Since c_0 is the smallest we can get:

$$min(h_s) = \inf[h_s(k)] = c_0 - c_s - \frac{1}{2}(\beta_s + \beta_0) \ , \tag{3.40}$$

and thus our bandwidth becomes,

$$max(h_s) - min(h_s) = c_N - c_0 + \frac{1}{2}(2\beta_s + \beta_N + \beta_0) \ . \tag{3.41}$$

As we can see is then $b_s = \beta_s + k_{max}$. Further proof of this is established in Appendix 6.3. We can now begin to design some superoscillating aperture arrays.

3.3 Proof of Superoscillations in Diffraction Gratings

The aim of this section is to show proof that diffraction gratings when illuminated by plane waves can give rise to superoscillations, at least in the mathematical sense.

3.3.1 Proof 1: Not all Diffraction Gratings Superoscillate

The definition of a superoscillation is given by:

> A local region of a band-limited function that oscillates faster than the function's fastest Fourier component

By using Fourier optics we can arrive at an equation for the general intensity pattern for a slit aperture array, as seen in equation 3.15. Which for a diffraction grating simplifies down by $\beta_j = \beta_m = a$ to:

$$I(y) = \sum_{j=0}^{N} a^2 \operatorname{sinc}^2\left(\frac{a\pi y}{L\lambda}\right)\left[1 + 2\sum_{m=j+1}^{N} \cos\left(\frac{2\pi y}{L\lambda}[c_j - c_m]\right)\right] \tag{3.42}$$

where c_j are defined as before in equation 3.3. Whereas, β_j has fewer constraints on it, but $(\forall j \in \mathbb{N})$ must be real and positive, so $\beta_j \in \mathbb{R}^+$ These constraints can be seen in figure 3.2. Equation 3.42 can actually be simplified even further into:

$$I(y) = a^2(N+1)\,\mathrm{sinc}^2\left(\frac{a\pi y}{L\lambda}\right)\left(1 + 2\sum_{j=1}^{N}\cos\left(\frac{2\pi y}{L\lambda}[a+\epsilon_j]\right)\right) \tag{3.43}$$

Given that we are examining a diffraction grating, we will assume equal spacing, so $\epsilon_j = a + \epsilon,\ \forall j$.

$$I(y) = a^2(N+1)\,\mathrm{sinc}^2\left(\frac{a\pi y}{L\lambda}\right)\left(1 + 2\sum_{j=1}^{N}\cos\left(\frac{2\pi y}{L\lambda}[a+\epsilon]j\right)\right) \tag{3.44}$$

It can also be shown that the maximum Fourier frequency component by a diffraction grating is given by:

$$f_{max} = \frac{2\pi}{L\lambda}k_{max} \tag{3.45}$$

where:

$$k_{max} = (c_N - c_0 + a) \tag{3.46}$$

Therefore we now have a target to beat with our superoscillatory functions.

We also need some tools to determine the local wavelengths of the functions. Given that we are looking at intensity profiles of diffraction patterns, the way this will be done is by looking for the zeroes of the function. An equivalent method is to find the difference between all sequential maxima or minima of the function. This is because the intensity profile always has a turning point at 0 as it is always positive and thus this is always a minima. Thus, finding the difference between zeroes is the same as finding the difference between minima. We then need to know if there is a formula for the superoscillatory frequency. This is normally chosen, but let us examine the design equation, which is from applying Aharonov's supershift principle as described in section 2.4.1 to equation 3.15:

$$\prod_{\substack{t=0\\t\neq s}}^{N}\beta_t + k_{max} - g_{SO} - \beta_s \prod_{\substack{t=0\\t\neq s}}^{N}(\beta_t - \beta_s) = 0 \tag{3.47}$$

Which for diffraction gratings, and indeed any aperture array with a degeneracy of non-unique slit widths simplifies to

$$\prod_{\substack{t=0\\t\neq s}}^{N}(\beta_t + k_{max} - g_{SO}) = 0 \tag{3.48}$$

This is because iff $\exists t$ such that $\forall t \neq s, \exists \beta_t = \beta_s$ then the second term always becomes zero at some point. Therefore, for a diffraction grating, equation 3.48 becomes:

$$(a + k_{max} - g_{SO})^N = 0 \tag{3.49}$$

which can only be solved when $g_{SO} = a + k_{max}$, which when renormalised into system coordinates becomes $g_{S0} = \frac{\pi}{L\lambda}(a + k_{max})$. Note that a and k_{max} are properties of the system, and are fixed, but g_{SO} is usually something we choose, but here it is in terms of system properties and therefore also fixed for the system.

Let us compute an example, single slit diffraction. As can be seen from both equation 3.42 and figure 3.7 the zeroes of the function occur when

$$\sin\left(\frac{a\pi y_0}{L\lambda}\right) = 0 \rightarrow y_0 = \frac{nL\lambda}{a}\ , n \in \mathbb{Z}\ , \tag{3.50}$$

which for the function shown in figure 3.7 gives $y_0 = 5n$. This agrees well with what we see, and the difference between the zeroes $\Delta y_0 = 5 = \frac{\lambda_{loc}}{2}$ Given this we know that

$$f_{loc} = \frac{2\pi}{\lambda_{loc}} = \frac{\pi}{\Delta y_0} = \frac{\pi}{5} \tag{3.51}$$

Now referring to the design equation, we see that the design equation for this system

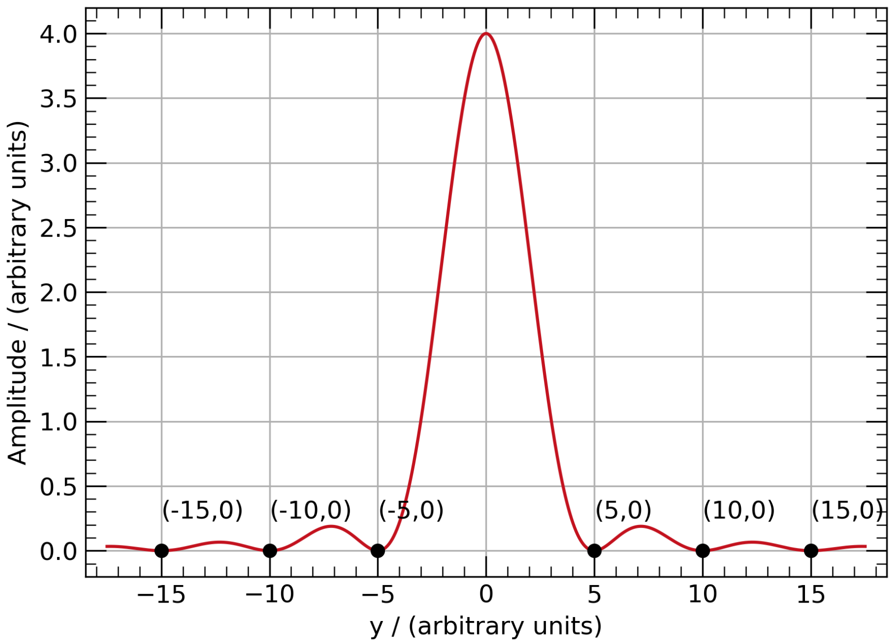

Figure 3.7: The intensity profile of a single slit aperture with the zeroes highlighted. This was generated by using equation 3.42 with $a = 2$, $\lambda = 1$, $L = 10$, and $c_j = c_m = 0$

is:

$$(a + k_{max} - g_{SO})^N = 0 \tag{3.52}$$

where N=0. This causes an issue, and even when computing g_{SO} and f_{max}:

$$\begin{aligned} f_{max} &= \frac{\pi}{L\lambda}(c_N - c_0 + a) = \frac{\pi}{5} \\ g_{SO} &= \frac{\pi}{L\lambda}(a + k_{max}) = \frac{2\pi}{5} \end{aligned} \tag{3.53}$$

It is easy to verify by inspection that the highest frequency component involved here is $f_{max} = f_{loc} = \frac{\pi}{5}$

However if we compute another example, the double slit diffraction grating. Since we are only interested in the very highest local frequencies we look where there is the fastest local oscillations, which can be seen by the zoomed version of the function in figure 3.8 in figure 3.9.

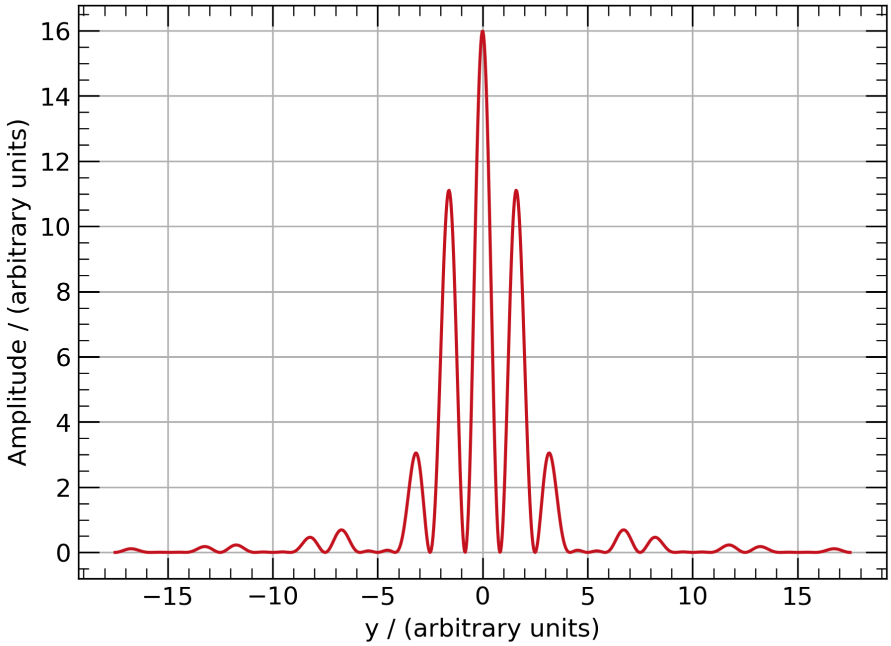

Figure 3.8: The intensity profile for double slit diffraction. This was generated by using equation 3.42 with $a = 2$, $\lambda = 1$, $L = 10$, and $c_0 = -3$, $c_1 = 3$

If we compute the local frequency from the zeroes of the function we get:

$$f_{loc} = \frac{2\pi}{2(5 - 4.1667)} = 1.2\pi \tag{3.54}$$

Now computing f_{max} and g_{SO}:

$$\begin{aligned} f_{max} &= \frac{2\pi}{L\lambda}(3 - (-3) + 2) = \frac{8\pi}{5} \\ g_{SO} &= \frac{2\pi}{L\lambda}(a + k_{max}) = 2\pi \end{aligned} \tag{3.55}$$

Clearly, this system does not superoscillate as $f_{loc} < f_{max}$. Therefore by contradicting our initial hypothesis, we have shown that not all diffraction gratings superoscillate

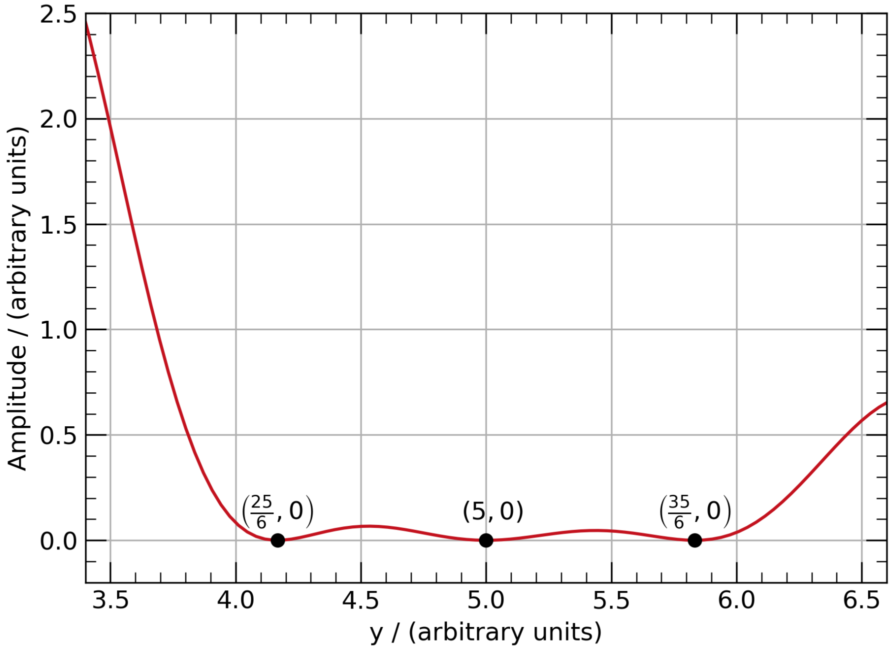

Figure 3.9: The zoomed in intensity profile for double slit diffraction, focused on the site of fastest oscillation. This was generated by using equation 3.42 with $a = 2$, $\lambda = 1$, $L = 10$, and $c_0 = -3$, $c_1 = 3$ and focuses on the interval $[3.5, 6.5]$

3.3.2 Examination of Diffraction Gratings for Superoscillation

However, if we examine equation 3.44 we can begin to examine an even further reduced problem. If we consider a system where we fix the gaps between the slits (ϵ) and then try and solve for zeroes this system. As we are introducing a new variable to this mix, we need to set some constraints on it. Here, ϵ will take very similar constraints to β and as such the constraints are that ϵ_j is real, $\epsilon_j \in \mathbb{R}$, and positive, $\epsilon_j > 0$. These constraints on ϵ_j can be seen in figure 3.3. Given these constraints, we need to solve the equation:

$$I(y) = a^2(N+1)\,\mathrm{sinc}^2\left(\frac{a\pi y}{L\lambda}\right)\left(1 + 2\sum_{j=1}^{N}\cos\left(\frac{2\pi y}{L\lambda}[a+\epsilon]j\right)\right) = 0 \qquad (3.56)$$

giving us two sets of solution points, $\{s_0\}_m$, $\{t_0\}_n$, the sinc solutions and the trig solutions, respectively. The sinc solutions are given when the sinc function's argument is an integer multiple of π, except for 0, (which is a special case due to the denominator of the sinc function also approaching 0 at this point):

$$\{s_0\}_m = \left\{ \frac{mL\lambda}{a}, m \in \mathbb{Z} \setminus 0 \right\} . \tag{3.57}$$

The trigonometric solutions are given when the cosine sum is equal to $-1/2$, which is a tricky thing to solve. However, using some approximations, as N increases, the first zero is given reasonably well by:

$$t_0 = \sqrt{\frac{3}{N(N+1)}\frac{L\lambda}{\pi(a+\epsilon)}} . \tag{3.58}$$

Therefore, the difference between sequential zeroes, Δy_0 will be found one of two ways: the first is the difference between the trigonometric solutions ; the second is the difference between trigonometric and sinc solutions. The reason that we do not consider the difference between sinc solutions is that the trigonometric solutions are always going to occur before another sinc solution does, as they are higher frequency, thus no sinc solution is sequential to another sinc solution.

The difference between sequential zeroes is given by:

$$\Delta y_0 = |s_m - t_n| \tag{3.59}$$

Thus we want to know if there is a solution in the neighbourhood of $\frac{mL\lambda}{a}$, so using Newton Raphson:

$$x_{n+1} = \frac{m\lambda L}{a} + \frac{1 + 2\sum_{j=1}^{N} \cos\left(2\pi mj\left[1+\frac{\epsilon}{a}\right]\right)}{2\sum_{j=1}^{N} \sin\left(2\pi mj\left[1+\frac{\epsilon}{a}\right]\right)\left[\frac{2\pi j}{L\lambda}[a+\epsilon]\right]} \tag{3.60}$$

which when expanded and simplified, becomes:

$$x_{n+1} = \frac{m\lambda L}{a} + \frac{1 + 2\sum_{j=1}^{N} \cos\left(2\pi mj\frac{\epsilon}{a}\right)}{2\sum_{j=1}^{N} \sin\left(2\pi mj\frac{\epsilon}{a}\right)\left[\frac{2\pi j}{L\lambda}[a+\epsilon]\right]} \tag{3.61}$$

If we assume there to be a zero in and around $\frac{m\lambda L}{a}$ for the trig solutions, then the difference between the sinc solutions and the trig solutions is given exactly by:

$$\Delta y_0 = \frac{1 + 2\sum_{j=1}^{N} \cos\left(2\pi m j \frac{\epsilon}{a}\right)}{2\sum_{j=1}^{N} \sin\left(2\pi m j \frac{\epsilon}{a}\right) \left[\frac{2\pi j}{L\lambda}[a+\epsilon]\right]} \ . \tag{3.62}$$

Thus using the values for f_{loc} we retrieve that:

$$f_{loc} = \frac{4\pi\sum_{j=1}^{N} \sin\left(2\pi m j \frac{\epsilon}{a}\right) \left[\frac{2\pi j}{L\lambda}[a+\epsilon]\right]}{1 + 2\sum_{j=1}^{N} \cos\left(2\pi m j \frac{\epsilon}{a}\right)} \tag{3.63}$$

As we now have the local frequencies let's consult what the global frequencies maximum would be to see if superoscillations can occur. The maximum Fourier frequency can be given by equations 3.45 & 3.46 but her we have no c_j to consider, so instead we use the version of equation 3.46 based on the widths and gaps between slits:

$$k_{max} = \beta_0 + \sum_{l=1}^{N} \epsilon_l + \beta_l \ . \tag{3.64}$$

By our simplifications however, all $\beta_j = a$ and all $\epsilon_j = \epsilon$ thus this equation becomes:

$$k_{max} = (N+1)a + N\epsilon \ . \tag{3.65}$$

Substituting into equation 3.45:

$$f_{max} = \frac{2\pi}{L\lambda}([N+1]a + N\epsilon) \tag{3.66}$$

and thus we have our yardstick.

The test now is to find if and when the local frequencies are larger than the maximum Fourier frequency, so our pivotal inequality is as simple as:

$$f_{loc} > f_{max} \tag{3.67}$$

Starting with the first formulation of f_{loc}:

$$\frac{\pi(a+\epsilon)}{L\lambda} > \frac{2\pi}{L\lambda}([N+1]a + N\epsilon) \tag{3.68}$$

which given that $N \in \mathbb{N}$ and $N > 0$, is blatantly contradictory, thus this local frequency does not show superoscillation.

However, if we examine the second formulation of f_{loc} we retrieve some more interesting results and ask does the following hold:

$$\frac{4\pi \sum_{j=1}^{N} \sin\left(2\pi m j \frac{\epsilon}{a}\right)\left[\frac{2\pi j}{L\lambda}[a+\epsilon]\right]}{1 + 2\sum_{j=1}^{N} \cos\left(2\pi m j \frac{\epsilon}{a}\right)} > \frac{2\pi}{L\lambda}([N+1]a + N\epsilon) \text{ ?} \tag{3.69}$$

The quotient on the right hand side can clearly diverge, as the denominator can vanish at certain values of $\frac{\epsilon}{a}$, and tends to around the values that $\epsilon \approx a$ or integer values thereof. Indeed around $\epsilon = a$ the entire quotient behaves as a tangent function, and we actually don't want $\epsilon = a$ exactly as it reduces the quotient to near 0. Thus some small aberration from $\epsilon = a$ is enough to cause superoscillation Given that we want $\epsilon = a + \varepsilon$, where $\varepsilon > 0$ for manufacture and experimental reasons, we can say that any integer multiplier, w, of $\epsilon = w(a + \varepsilon)$ just pushes the superoscillatory region to further zeroes of the sinc solution, and is categorised by the variable m.

3.4 Designing Superoscillatory Arrays

In this section we will try to design some superoscillatory arrays, based on various methods detailed in prior sections.

3.4.1 Designing Aharonov Aperture Arrays

The design of apertures comes from actually solving the systems of equations,

$$\prod_{\substack{t=0\\t\neq s}}^{N}\frac{b_t - g_{SO}}{b_t - b_s} = \beta_s \ , \tag{3.70}$$

for all ϵ_j and β_j. This produces N polynomials of order N but we have $2N$ unknowns, so this is an underdetermined system. However, we have freedom to choose a set of either ϵ_j or β_j, in this instance we will choose a set of ϵ_j. Plugging this in to equation (3.70) we have

$$\prod_{\substack{t=0\\t\neq s}}^{N}\frac{\beta_t + k_{max} - g_{SO}}{\beta_t - \beta_s} = \beta_s \ , \tag{3.71}$$

where k_{max} can be substituted in terms of ϵ_j and β_j to gain,

$$\prod_{\substack{t=0\\t\neq s}}^{N}\left[\frac{\beta_t + \beta_0 - g_{SO}}{\beta_t - \beta_s} + \sum_{l=1}^{N}\frac{\epsilon_l + \beta_l}{\beta_t - \beta_s}\right] = \beta_s \ . \tag{3.72}$$

This can then have the constants of the sum be gathered into a term, $D = \sum_{l=1}^{N}\epsilon_l - g_{SO}$ to give,

$$\prod_{\substack{t=0\\t\neq s}}^{N}\frac{1}{\beta_t - \beta_s}\left[D + \beta_t + \beta_0 + \sum_{l=1}^{N}\beta_l\right] = \beta_s \ , \tag{3.73}$$

which gives rise to a simpler form of the equation in,

$$\prod_{\substack{t=0\\t\neq s}}^{N}\left[D + \beta_t + \beta_0 + \sum_{l=1}^{N}\beta_l\right] - \prod_{\substack{t=0\\t\neq s}}^{N}\beta_s(\beta_t - \beta_s) = 0 \tag{3.74}$$

Or:

$$\prod_{\substack{t=0\\t\neq s}}^{N}\left[\beta_t + k_{max} - g_{SO}\right] - \beta_s\prod_{\substack{t=0\\t\neq s}}^{N}(\beta_t - \beta_s) = 0 \tag{3.75}$$

This system of equations is solved numerically using the solvers detailed in the next section.

3.4.2 Solving The Aharonov Design Equation

As detailed in the previous section 3.2 there is a design equation that needs to be solved in order to determine the start and thus all other positions based on the gaps between the slits, ϵ. Solving this equation is not as simple as it seems because although we can dictate the set of slit widths, $\{\beta_j\}_j$, we still have to solve for separation, ϵ. Restating the equation 3.75:

$$\prod_{\substack{t=0 \\ t\neq s}}^{N} [\beta_t + k_{max} - g_{SO}] - \beta_s \prod_{\substack{t=0 \\ t\neq s}}^{N} (\beta_t - \beta_s) = 0 \ , \tag{3.76}$$

we can now examine some interesting conditions on the equation, such as examining once again the degenerate case. If there exists more than one slit with the same slit width, then the second term of the equation disappears completely, as there will be some $\beta_t = \beta_s$ where $t \neq s$. This gives rise to our degenerate equation:

$$\prod_{\substack{t=0 \\ t\neq s}}^{N} [\beta_t + k_{max} - g_{SO}] = 0 \ , \tag{3.77}$$

which in order to solve this equation, we decide on a g_{SO} that we wish the apertures to achieve, and the set of slit-widths β_j that we want to use, and solve for k_{max} which contains our starting and ending positions. As can be seen each term in this equation can be equal to zero in order to satisfy the equation, and thus we can see that we have at least N roots to this equation. We also have more because we can iterate through the s values it takes, and thus we have a system of N equations. We can narrow down the number of solutions by imposing that k_{max} must be larger than the sum of all slit widths:

$$\sum_{t=0}^{N} \beta_t < k_{max} < g_{SO} \tag{3.78}$$

which gives a region for which the solution can be searched. Comparison between the s iterated equations can also help narrow down the solution, as if there is a common solution then that can be used as a solution. Symmetry can also be used to reduce the problem, as if there is a line of symmetry along the 0 of the axis, then both sides can use be solved for individually. Otherwise numerical solvers are used to try and solve these problems by finding where they cross the positive-negative threshold and then interpolating linearly between the two points. This assumes that there are no discontinuities in the equation, which given that it is a polynomial, we are relatively safe in assuming. This allows us then to find values for k_{max} based on different outermost slits. This is an iterative process, and is based very heavily on perturbations of the slits within the set that have been chosen.

If there is instead a set of unique slit-widths, we need to solve the full equation 3.75. One of the easiest ways to solve this, is to return to the system it describes and try to find the offset for which the Aharonov supershift function achieves the Aharonov coefficient corresponding to the particular slit-width. It is important to note that the following equation only works for unique slit sets, or systems with symmetry around the origin, as otherwise Y_j is not calculable and there is no reflection to reduce the system into a set of unique slit widths. This looks something like:

$$Y_j = G(\beta_j(x - \delta_j)) \ . \tag{3.79}$$

Here, we use the definiton of Y_j established in equation 2.49 Finding the offsets δ_j allows for the positioning of the predetermined slit-widths, and given that there is a restricted area over which the aperture can be made, then the value of g_{SO} can be determined by using this maximum limit to the offset to determine k_{max} as the positioning of the slits is what leads to the highest frequencies. This works by treating each slit-width β_j (or slit pair) as being independent from the other slit-widths, and thus able to be solved for their offsets individually. The equation then becomes a search for 0 again and various different methods can be employed. Both Newton-Raphson and interpolation methods are used to solve equation 3.79.

3.4.3 Designing Diffraction Gratings

Now that we have shown that solutions do exist for ϵ the best thing to do is to introduce a constant to define how much faster we want the local frequency to be over the global maximum. We will call this constant g, the superoscillatory metric, a measure of how much faster than the fastest Fourier component f_{loc} is. It is defined as:

$$g = \frac{f_{loc}}{f_{max}} \ , \tag{3.80}$$

and should be such that $g > 1$ for superoscillations. Let us return to equation 3.67 and make it an equality rather than an inequality:

$$f_{loc} = g f_{max} \ . \tag{3.81}$$

Following the logic of the previous section 3.3, we arrive, from equation 3.69, at the result that:

$$g = \frac{4\pi \sum_{j=1}^{N} \sin\left(2\pi m j \frac{\epsilon}{a}\right)[[a+\epsilon]j]}{\left[[N+1]a + N\epsilon\right]\left[1 + 2\sum_{j=1}^{N}\cos\left(2\pi m j \frac{\epsilon}{a}\right)\right]} \ , \tag{3.82}$$

which is given all in terms of system parameters, and so each superoscillatory diffraction grating should be able to be characterised by its g value. From the constraints that $\epsilon = a + \delta$ for some $0 < \delta < a$ we can numerically try to find the ideal δ to cause a superoscillation at a given g. We can also express this in a different way, we can try to find the multiplier $d = \frac{\epsilon}{a}$, which leads to the following equation to solve:

$$g = \frac{4\pi \sum_{j=1}^{N} \sin\left(2\pi m j d\right)[[1+d]j]}{\left[N(1+d)+1\right]\left[1 + 2\sum_{j=1}^{N}\cos\left(2\pi m j d\right)\right]} \ . \tag{3.83}$$

This is solved through numerical methods, solving for values of d for a chosen g. This search space is limited to just $1 < d < 2$ due to the constraints stated previously.

Chapter 4

Results

This chapter deals with the results achieved via simulation of various different aperture designs. The designs simulated and analysed range from the early design work, that was conducted as a proof of concept, to later designs that were created as a part of the work conducted in the previous chapter. These designs were simulated in tandem with the development of the theory from chapter 3 and informed the theory in iterative designs. In this chapter we see specific solutions to the design equations and their simulated results. These specific solutions are detailed in tables at the end of the thesis, in tables 6.3 and 6.3. We also discuss the impact and efficacy of each of the designs in the discussion section of this chapter.

4.1 Results

This section covers simulated results from the various designs created throughout the process of refining superoscillatory aperture design. At the time of creation, most of these apertures were believed to superoscillate. However, with hindsight, and better tools for analysis, it can be seen that not all the apertures that were intended to superoscillate, superoscillated.

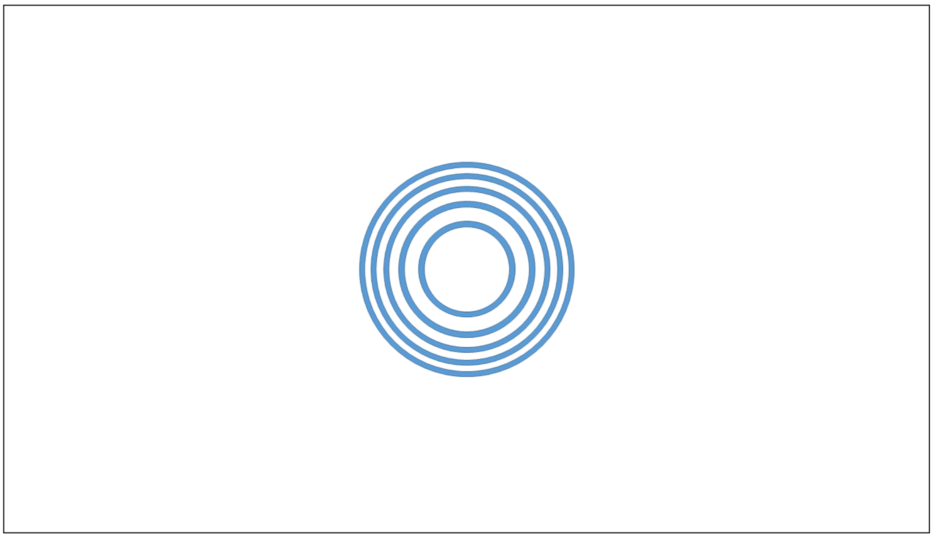

Figure 4.1: A figure illustrating the design used for annular aperture array, adapted from Toraldo di Francia [1] and detailed in table 6.3

4.1.1 Early Designs

Unfortunately, only a small number of the designs were tested, but those that have, have produced some very promising results. These results howvever have since been lost and as such will not be discussed. The Torlado Di Francia based design that was made for the annular apertures based on his paper [1] but was modified to suit our needs. Full details of this design are given in figure 4.1 and table 6.3.

Although we are not discussing experimental results, the results shown in figure 2.2 did highlight a few issues with the designs and the experiment. One of the biggest issues with the designs was the blocking of the central region, as this meant that the laser power actually able to generate phonons was severely restricted. This was a problem throughout all of the early design work, as all of the early designs solutions seemed to preclude the central region. This problem was remedied in later design and theory approaches. One of the big problems with the experiment was that due to the designs excluding so much laser power, the signal to noise ratio (SNR) was very bad, as the actual signal was massively attenuated by the absorption and reflection of the gold shadowmask. The other problem was with the deposition of

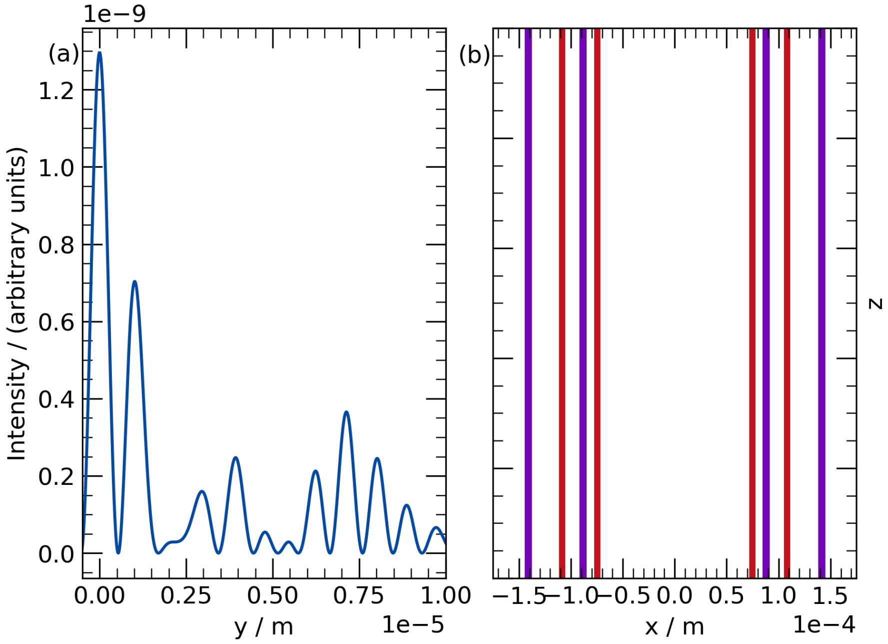

Figure 4.2: A figure depicting the simulated diffraction pattern (a.) and the design (b.) of a slit aperture array that was produced for tests by optical lithography. It can be seen that there are features that are on the order of the wavelength of the phonons in GaAs $\approx 1\mu m$

the polystyrene thin film interferometer layer on the back of the GaAs substrate. Any small deposition error could lead to very large noise in the signal read out by the laser probe, and this sensitivity to manufacture was one of the leading causes of noise. The combination of superoscillations low amplitude, loss of laser power due to designs and the deposition issues lead to the early designs and experiments having poor detectability.

One of the early designs was the progenitor for much of the rest of this thesis. As shown in figure 4.2, a superoscillatory slit aperture array was attempted to try and cause superoscillations, using system values of $L = 450\mu m$ for the length of GaAs substrate and $\lambda = 1\mu m$ for the acoustiv wave wavelength. Naively, it was thought that the central spot would likely be the location of the superoscillatory spot, but as further investigation showed, that superoscillation actually comes much further out in the pattern. There are in fact many superoscillations within this diffraction

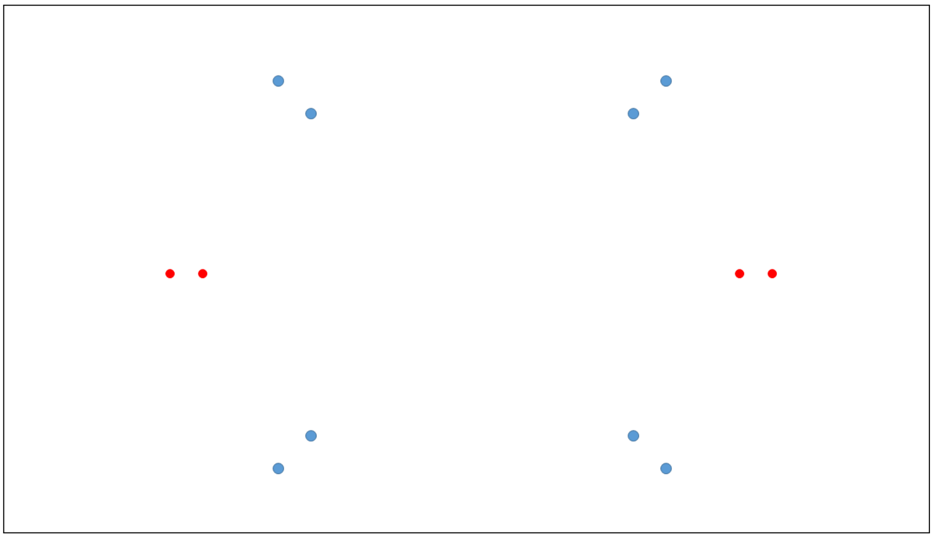

Figure 4.3: A graphic showing a circular aperture based design for superoscillatory diffraction. The red apertures represent an aperture diameter of $4\mu m$ and the blue apertures are of diameter $5\mu m$. The offset blue apertures are at an angle of $(2n+1)\frac{\pi}{4}$ from the plane of the red apertures

pattern, but the highest spatial frequency one:

$$f_{loc}(EDD2) = 5.15MHz \tag{4.1}$$

occurs between $5.13-5.74\mu m$ within the pattern, giving a local wavelength of $\lambda_{loc} = 0.61\mu m$. Compared to the calculated maximum frequency of EDD2 is:

$$f_{max} = 4.03MHz \ , \tag{4.2}$$

it is clear that the aperture array does actually superoscillate, as $f_{max} < f_{loc}$. As discussed further in the subsequent section 4.2, one of the biggest problems with this design is that the central region totally blocks the light that would be incident on it, thus reducing the strength of the signal significantly.

The final initial design was one based on circular apertures and was designed to try and implement some off-axis, non-radially symmetric designs, to see how super-oscillations in more than 1D behave. The reason for this is that according to [19] superoscillations that occur in more than 1 dimension are even further suppressed in amplitude. This is because the amplitude and various local frequencies in a dimension are related as a Fourier pair, and so trying to cause a superoscillation of any significant difference in more than 1 dimension, i.e getting a very small, circular spot size on a saser will lead to such a significant drop in amplitude as to make the spot almost negligible. This leads to most circularly symmetric superoscillations having some form of eccentricity to the spot size.

4.1.2 Slit Designs

This section concerns the designs and results of slit aperture arrays that were created by following the methods set out in section 3.4.1. The following designs were all made to try and cause superoscillations on the reverse side of the GaAs substrate. The first design, named SDD1, is shown in figure 4.4, and is a multi-width array. This means that the simplifications of the diffraction grating cannot be made here, instead it took a full numerical approach via the methods laid out in section 3.4. In figure 4.4(a) the design can be seen, and the slit widths and central slit positions are given by the corresponding entry in table 6.3. It can be seen that the diffraction pattern this produces has a very tight central peak, with very small features to its sides. The question now becomes whether this pattern actually superoscillates. We now rely on the tools developed in the basic superoscillatory theory section 2.3, by comparing the highest Fourier component to the smallest local feature. Given that we have all the information we need to deduce the highest Fourier component, it is simply given by:

$$f_{max}(SDD1) = 0.57MHz \tag{4.3}$$

and comparatively, the largest local frequency is given by:

$$f_{loc}(SDD1) = 0.93MHz \tag{4.4}$$

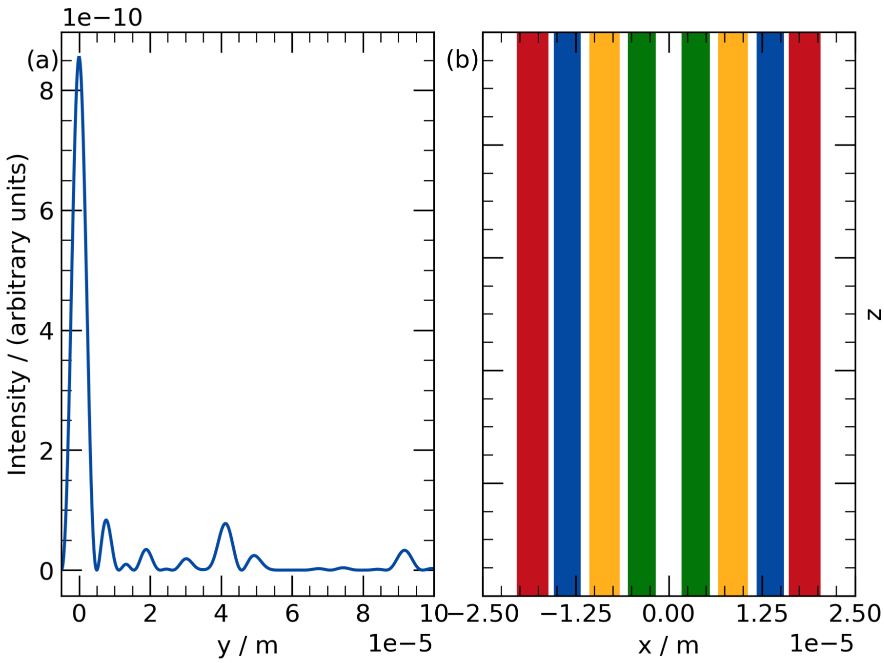

Figure 4.4: Design and simulated diffraction pattern of the SDD1 aperture array. This is a full design with multiple slit widths: red= $3.375\mu m$, purple= $3.5\mu m$, blue= $3.75\mu m$, green= $4.0\mu m$. The diffraction pattern graph is intensity in $\frac{W}{m^2}$ vs position along the y-axis in m. This is one of the designs that was used in experimental validation via DMD experiment

and thus we can definitively say that this design superoscillates.

It is important to note that the simulations used to produce the diffraction patterns seen in the following sections were numerical approximations of the Fourier transform of the transmission functions of each of these slit apertures. The reason this simulation was chosen over more in-depth simulations like finite element method (FEM) is that these were meant as a first pass simulation, but ended up giving good agreement with experiment, and so weren't revised into more complicated methods.

The second slit design that was submitted for experimental verification was SDD2. This was purely to help as a test case to try and verify whether the simulations were close to the achieved results or not. This would help determine whether the simplistic Fourier transform based simulations were good enough, rather than having to resort to costly FEM simulations to coincide with the system. The achieved simulation

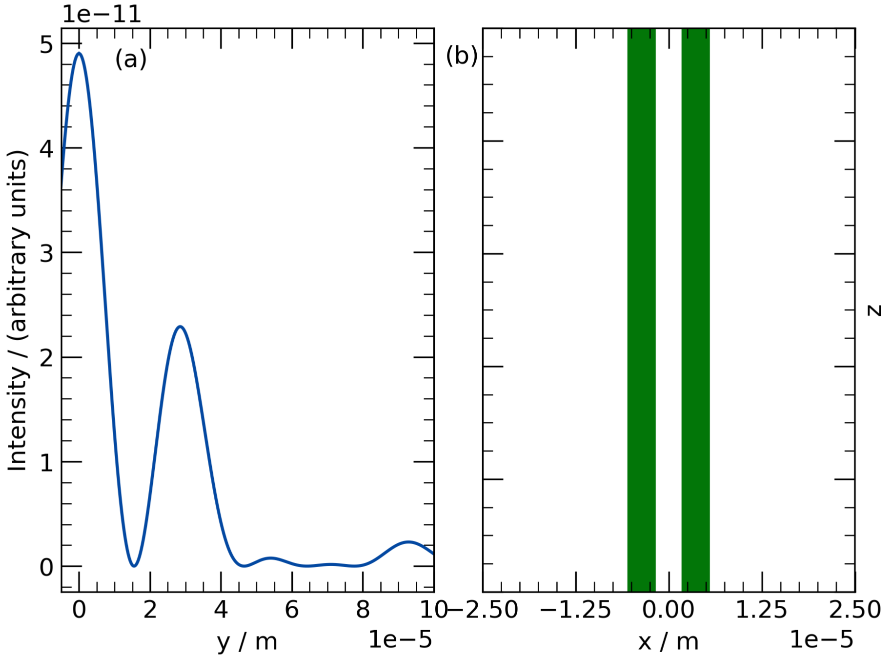

Figure 4.5: Design and simulated diffraction pattern of the SDD2 aperture array used to verify that Fourier optics is a valid method. This is a double slit design with a single width: green= $4.0\mu m$. The diffraction pattern graph is intensity in $\frac{W}{m^2}$ vs position along the y-axis in m. This is one of the designs that was used in experimental validation via DMD experiment

results were

$$f_{max}(SDD2) = 0.15MHz \ , \tag{4.5}$$

and

$$f_{loc}(SDD2) = 0.24MHz \ . \tag{4.6}$$

and can be seen in figure 4.5 which shows that this design superoscillates with $\lambda_{loc} = 3.3\mu m$. This was not expected, but a very interesting result.

The third design that was given for experimental verification of this batch was SDD3 and was to try and demonstrate the effects of simulation vs. experiment on the highest Fourier component set of apertures in the full aperture array SDD1.

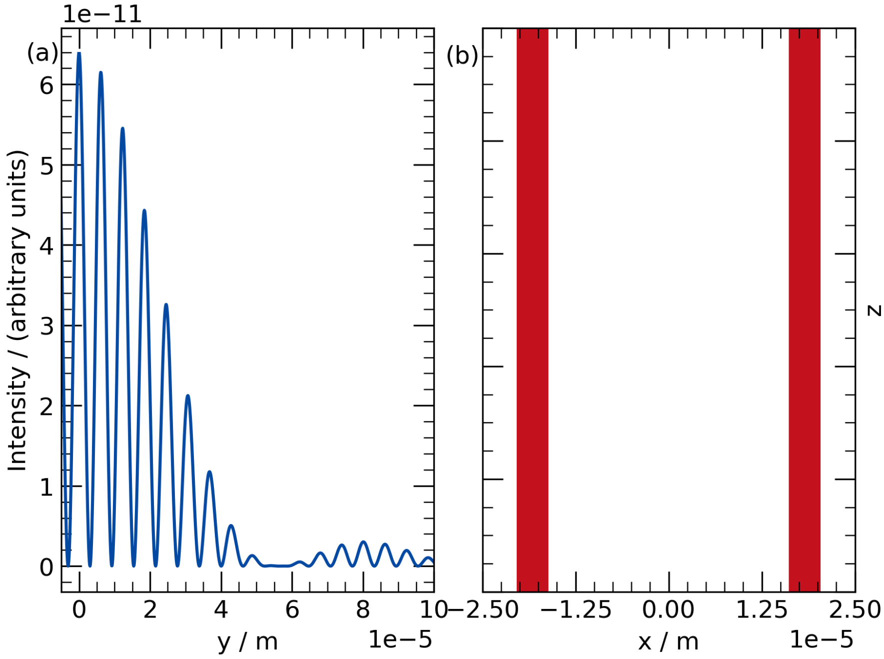

Figure 4.6: Design and simulated diffraction pattern of the SDD3 aperture array used to verify the highest frequency component within the aperture array diffraction pattern. This is a double slit design with a single width: red= $3.375\mu m$. The diffraction pattern graph is intensity in $\frac{W}{m^2}$ vs position along the y-axis in m. This is one of the designs that was used in experimental validation via DMD experiment

As can be seen, the agreement between

$$f_{max}(SDD3) = 0.57MHz \; , \tag{4.7}$$

and

$$f_{loc}(SDD3) = 1.34MHz \; , \tag{4.8}$$

this design also superoscillates at $\lambda_{loc} = 2.4\mu m$, which was not intended but is interesting.

Despite the fact that only SDD1 was supposed to superoscillate, all 3 of these designs appear to superoscillate. This is a curious result given that SDD2 and SDD3 were meant only to check and compare the simulation results to the experimental results, as they are the simplest designs. Given these results, it struck me as curious to

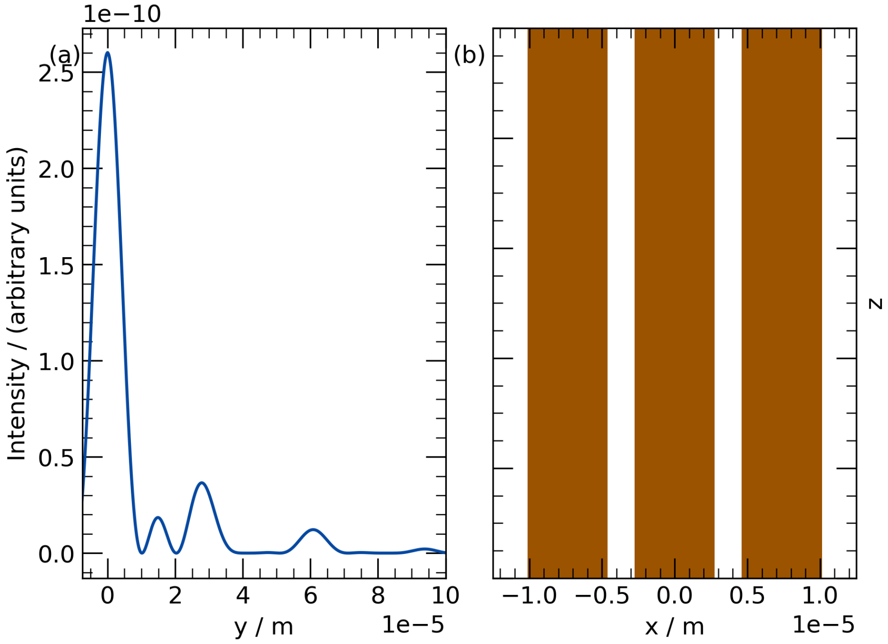

Figure 4.7: Design and simulated diffraction pattern of the IDD1 aperture array used to iteratively test permutations of the apertures arrays solved with the tools in 3.4. This is a multi-slit design with a single width: brown= $5.375\mu m$. The diffraction pattern graph is intensity in $\frac{W}{m^2}$ vs position along the y-axis in m. This is one of the designs that was used in experimental validation via DMD experiment

see what perturbations of apertures given a set of position solutions that had large degeneracy amongst the solutions would do to the diffraction pattern.

4.1.3 Iterative Designs

These iterative designs were made with a set of slits and positions that had repetitions (degeneracies) within the position solutions. This seemed to imply that any perturbation of positions and apertures within this solution space would work; however, it needed verification.

As can be seen in figure 4.7 a diffraction grating style design was used. At the time this was designed, it was believed that single width diffraction grating aperture arrays could not superoscillate, and so this was meant to be a control. However, the simulations and process of calculating the analysis on these results seemed to bring into question the veracity of that assumption. As can be seen by section 3.3.2, some

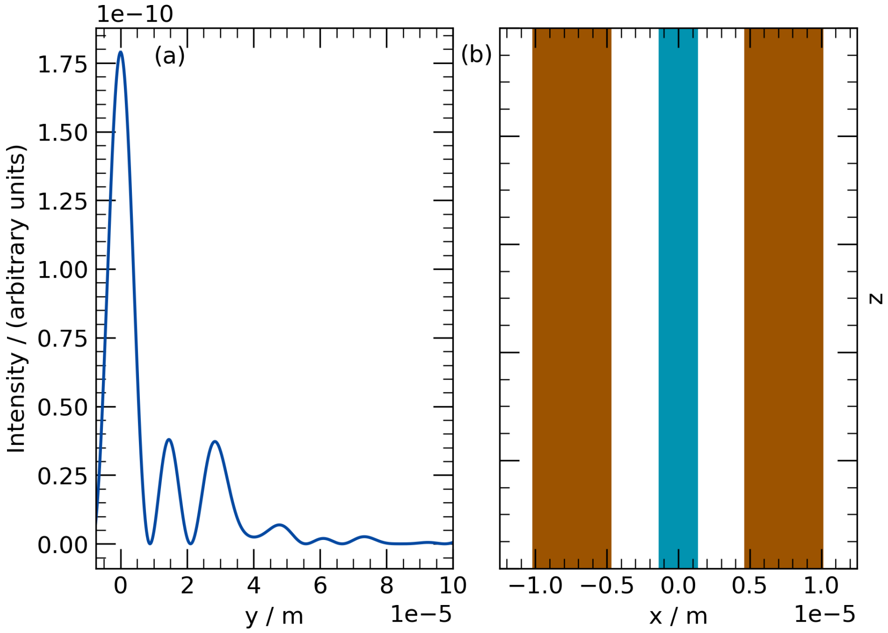

Figure 4.8: Design and simulated diffraction pattern of the IDD2 aperture array used to iteratively test permutations of the apertures arrays solved with the tools in 3.4. This is a multi-slit design with: blue= $2.625\mu m$ and brown= $5.375\mu m$. The diffraction pattern graph is intensity in $\frac{W}{m^2}$ vs position along the y-axis in m. This is one of the designs that was used in experimental validation via DMD experiment

diffraction gratings do in fact superoscillate. Although this result was not known at the time, it was worth comparing these variations with other variations.

The second variation that was used to experiment with the design was IDD2. This produces a curious diffraction pattern, as can be seen in figure 4.8(a) as there is a what looks possibly to be a high amplitude superoscillation in the first peak beyond the zero peak. However, this is in fact not a superoscillation, as this pattern does not superoscillate at all. It actually oscillates at exactly the expected frequencies. This is interesting, as this was supposed to be a part of a perturbation of solutions to the Aharonov design equation, and one of the degeneracies, but apparently, even when solving these equations, there are some solutions which do not superoscillate.

The third design was IDD3 which has its maximum superoscillatory region very close to the central peak. This superoscillation occurs between $13.0 - 18.4\mu m$, $\lambda_{loc} =$

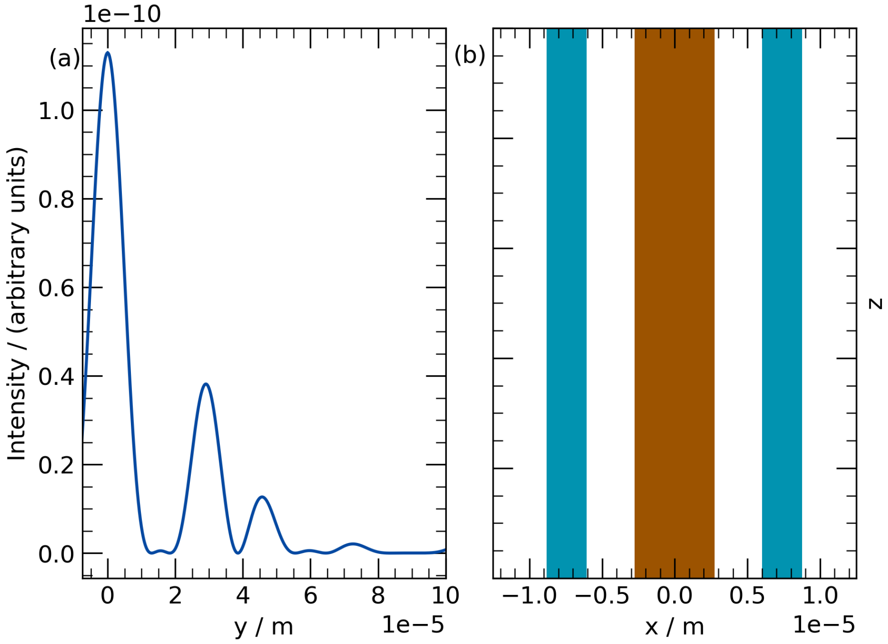

Figure 4.9: Design and simulated diffraction pattern of the IDD3 aperture array used to iteratively test permutations of the apertures arrays solved with the tools in 3.4. This is a multi-slit design with: blue= $2.625\mu m$ and brown= $5.375\mu m$. The diffraction pattern graph is intensity in $\frac{W}{m^2}$ vs position along the y-axis in m. This is one of the designs that was used in experimental validation via DMD experiment

$5.4\mu m$, and has a superoscillatory frequency of:

$$f_{loc}(IDD3) = 0.58MHz \ , \tag{4.9}$$

which when compared to its calculated maximum Fourier frequency at:

$$f_{max}(IDD3) = 0.24MHz \ , \tag{4.10}$$

clearly shows that IDD3 superoscillates.

Finally IDD4 delivers what is possibly the clearest example of a diffraction grating superoscillation. As can be seen from table 6.3 however, it's highest superoscillatory region occurs between $81.0 - 85.7\mu m$ from the centre of the pattern. This leads to a local frequency of

$$f_{loc}(IDD4) = 0.66MHz \ , \tag{4.11}$$

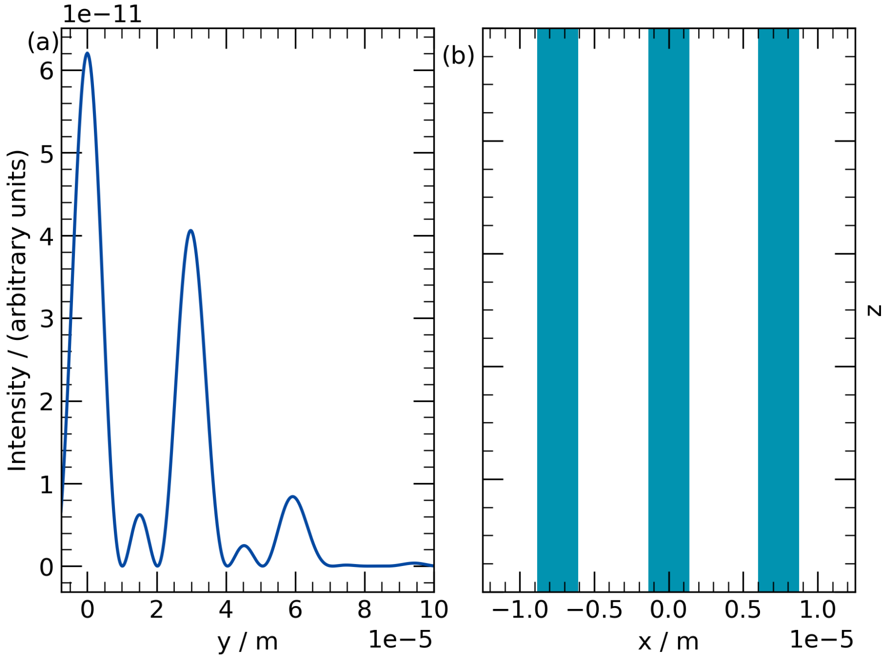

Figure 4.10: Design and simulated diffraction pattern of the IDD4 aperture array used to iteratively test permutations of the apertures arrays solved with the tools in 3.4. This is a multi-slit design with a single width: blue= $2.625\mu m$. The diffraction pattern graph is intensity in $\frac{W}{m^2}$ vs position along the y-axis in m. This is one of the designs that was used in experimental validation via DMD experiment

which compared to,

$$f_{max} = 0.24MHz \tag{4.12}$$

means that IDD4 superoscillates with the local wavelength of $\lambda_{loc} = 4.7\mu m$. As can be seen from these results the majority of the pertubations superoscillate, but not all. The reason for this is unknown.

4.2 Discussion

The designs laid out in the previous sections were designed iteratively via various different changes to the experiment and also to the theory. What worked and what did not was observed and then implemented as changes or kept if possible. This led to a variety of different designs, and as can be seen, especially with the iterative designs, a surprising number of them seem to superoscillate, at least in theory.

4.2.1 Early Designs

One of the biggest criticisms of the early designs was that because the designs blocked the central region, this caused an enormous loss of laser energy able to propagate through the system. This meant that the laser power needed to achieve any measurable results was too high to be achieved in the experimental set up that was being used. This was a large problem that plagued the experiment throughout. The signal to noise ratio (SNR) of all of the designs was poor. This is a problem with superoscillations in general, as the higher the superoscillatory frequency above the Fourier limit, the larger the wings around the superoscillatory region are in amplitude. This can be seen in the relationships between the energy and amplitude quotients in figures 2.4 and 2.6 respectively. Due to this fact, trying to measure superoscillations directly becomes an act of balancing a low superoscillatory frequency to reduce SNR and having a very precise system to be able to resolve the very slight differences in expected non-superoscillatory pattern and produced superoscillatory patterns.

Slit and Iterative Designs

The biggest change for the slit and iterative designs were the changes to the area over which the pattern could be produced. The previous $200\mu m \times 200\mu m$ was restricted to just $150\mu m \times 150\mu m$. This change reduced the solution space enormously, but also meant that a higher intensity of laser light could fall onto the region, leading to a higher intensity of phonon generation, and better detectability on the reverse of the substrate. This restriction in solution space corresponded to a change of methods in the experiment. This change was to replace the old optical lithography method with a new Deformable Mirror Device (DMD) to illuminate the superlattice. The DMD meant that the solution space was restricted because of it's limitations in resolution and the method of light projection from the DMD.

However, the theoretical results and the simulated result have shown that, at least in theory, the design equations work, and have produced superoscillatory diffraction patterns. interestingly though, when dealing with degenerate solutions, not all of the solutions do appear to superoscillate. The reason for this is unclear but it is a curious result. It sees to suggest a more complicated relationship between superoscillations than the ones we have detailed in the Apertures chapter, chapter 3. However, we do seem to have at least hit on some kind of relation, as although perhaps not the full description, as the majority of these patterns superosillate, we are at least better than random chance.

Interestingly, our highest superoscillatory increase, known as g factor, came from $IDD1$ which had a g factor value of 4.36. This was not intended and indeed, although it was meant to be superoscillatory, it was expected that the $SDD1$ aperture would perform better, due to it's high number of aperture widths. Indeed, all of the highest g factors come from diffraction grating style designs as opposed to mixed slit widths. This is likely as there are more of these designs when compared to mixed slit width designs, and is not of any physical significance. There is nothing in the equations to suggest that diffraction grating designs are always going to be the most superoscillatory, indeed they seem to be the most restricted in their designs. This restriction may actually work to their benefit in some degree, as it narrows the solution space that has to be searched in order to find them.

Chapter 5

Detection

As has been outlined in Section 2.3, certain previous methods for analysing whether a superoscillation exists within a function or not have certain flaws. In this chapter, we aim to address these flaws and try to formulate a new tool for detection of superoscillations based on overlap integrals with a particular form of superoscillating function.

5.1 Previous Methods

Perhaps the most widely used tool in the literature [9, 11, 24] is that of the phase gradient, also known as the local wavevector method. It is characterised by:

$$k_c(x) = -Im[\nabla \ln(f(x))] \tag{5.1}$$

which rephrased is:

$$k_c(x) = \frac{u(x)\nabla v(x) - v(x)\nabla u(x)}{u^2(x) + v^2(x)} \tag{5.2}$$

where $u(x), v(x)$ are the real and imaginary parts of the function $f(x)$, respectively. This is the main method for Berry in his paper predicting the fraction of superoscillations in N-Dimensional fields [11], however, as we have seen in 2.20 it can miss some superoscillations in 1D. This problem is actually compounded when trying to reproduce the Berry paper's results [11]. If we consider this tool for 1-D functions in general, we tend to find that there are issues with divergences or ambiguous answers. For example, the $\sin(x)$ function:

$$k_c(x) = -\operatorname{Im}[\nabla \ln(\sin(x))] = -\operatorname{Im}[\cot(x)] = 0 \ , \tag{5.3}$$

or:

$$k_c(x) = \frac{u(x)\nabla v(x) - v(x)\nabla u(x)}{u^2(x) + v^2(x)} \ , \tag{5.4}$$

where $u(x) = \sin(x)$ and $v(x) = 0$, and thus once again:

$$k_c(x) = 0 \ , \tag{5.5}$$

which states that the local wavevector of a $\sin(x)$ wave is 0. If we lift the restriction of taking the purely imaginary part and look instead at replacing it with:

$$k_c(x) = -i[\nabla \ln(\sin(x))] = -i\cot(x) \ , \tag{5.6}$$

as Konrad and Roux do in their paper [24], it becomes clear that instead of having a local wavevector of $k_c = 0$, we get a diverging k_c at $x = 0$ due to the $\cot(x)$ function. Indeed with the Konrad and Roux definition, any function which has a vanishingly small quotient in the logarithm derivative is liable to diverge. Berry's definition is able to get around this with taking the imaginary component but leads to any and all purely real functions having no local wavevector. This is evident from the second formulation, equation 5.4, where any function without imaginary component is going to be 0 in its local wavevector. This tool, whilst useful in its application to complex multi-dimensional fields does not have application in real 1-D function analysis.

Another type of detection algorithm are based on convolutions with oscillatory like waveforms, such as in Ezra et al.'s work [27] where they use convolutions with so called "top-hat", "sombrero" and other Gaussian derived functions to give a probability of a superoscillatory frequency or wavelength being within a function. This approach is novel and interesting for the fact that it is a relatively easily computable problem. It will give a spectra of wavelengths possibly in the function, with associated probabilities. This can then be further extended with statistics to give confidence intervals and other measures to give a probabilistic answer as to whether a superoscilaltion occurs within the function. One of the benefits to this method is that it has application in all complex, real and N-dimensional function, as the comparison function can easily be made to match these criteria.

However, it runs into the problem of introducing an unbounded Fourier space. Due to the nature of the Gaussians used in the analysis of the function having no bandlimit on their Fourier transform, the Fourier space becomes unbound, and thus only probabilities of superoscillations can be given. The reason this is such a problem is that we no longer know if any value we get for a given frequency above the bandlimit is due to superoscillations, or an expected aberration due to the unbound nature of the Fourier space. One of the other drawbacks is having to choose a Gaussian function with which to convolve the function under analysis. This is because different Gaussian profiles give better probabilities based off the local shape of the function. To give a slightly reductive overview of the method, it is like having a sheet of tracing paper, with infinitely many sizes and shapes of function and trying to match each part of the function to each of the different profiles on the tracing sheet. The benefit is it's quick and easy to perform, the downsides are that it is not a definitive answer, and you can only get a likeness probability; and that you introduce an unbounded Fourier space to the analysis. This unbounded frequency space is shown in Ezra et al. [27] and is used as a way of calculating these probabilities.

An unbound Fourier space is also the problem that is run into when considering a windowed Fourier transform. There are two ways of performing a windowed Fourier transform, one is to once again convolve the investigation function with a windowing function. This allows the Fourier transform to take place only over a given domain and that allows for the investigation of very specific parts of a function. The other is literally to change the limits on the integration of the Fourier transform to only cover the region of interest. These two are equivalent in the case of a rectangular $\mathrm{Rect}\left(\frac{x-c}{\beta}\right)$ as defined in equation 3.1 but with other windowing functions it is slightly different. This causes there to be a sinc envelope function in the frequency space, and when $\mathrm{Rect}\left(\frac{x-c}{\beta}\right)$ is convolved with a function that has a spatial range that is larger than it its frequency range is going to cause an unbound Fourier space due to the sinc function. However, one thing that every windowing function has in common is that they have an unbounded Fourier space and thus any superoscillatory effects that might exist will have to be deconvolved from the total Fourier transform. Whilst this is not impossible, it does introduce noise into the deconvolved Fourier space. This is because pointwise deconvolution of a restricted range of a physical variable leads to large amounts of "ringing" in the Fourier deconvolution [28]. This is in addition to the fact that given superoscillations are by their nature invisible to Fourier transforms, it would be likely that no extra information could be gained from this process.

5.2 Reproducing Berry

In order to demonstrate the issues with the previous methods, specifically the local wavevector method, we turn to a paper produced by Berry on the probability of superoscillations occurring in random complex fields [11]. In this paper Berry et al. predict that, according to the local wavevector methods, the probability quotient of random fields that superoscillate depends on the dimensions that the field exists within, and their results show that for 1D that quotient is:

$$P_{1\ super} = 1 - \frac{1}{\sqrt{2}} = 0.29289\ . \tag{5.7}$$

This probability is the one that we need to try to reproduce when reproducing this paper. This reproduction is based in numerical simulation of the system that Berry et. al studied in their paper. The system as described in [11] is one comprised of N monochromatic complex scalar waves, which have the form:

$$\psi(\mathbf{r}) = u(\mathbf{r}) + i\ v(\mathbf{r}) = \rho(\mathbf{r}) \exp\{i\ \chi(\mathbf{r})\}\ , \tag{5.8}$$

and define their local wavevector similar to equation 5.2 except they only consider the magnitude of the gradient of the phase:

$$k(\mathbf{r}) = |\nabla\chi(\mathbf{r})| = \frac{|u(\mathbf{r})\nabla v(\mathbf{r}) - v(\mathbf{r})\nabla u(\mathbf{r})|}{\rho^2(\mathbf{r})}\ . \tag{5.9}$$

Where $\rho(\mathbf{r})$ is an amplitude at a given point, and real function; $\chi(\mathbf{r})$ is the phase function and $\mathbf{r}$ is some N-dimensional coordinate vector $\mathbf{r} = \sum r_i \mathbf{e}_i$. In the paper a specific example for $N = 50$ with 25 frequencies distributed between $[-k_0,\ -0.99k_0]$ and the other 25 between $[k_0,\ 0.99k_0]$. In this they perform a Monte-Carlo style simulation to achieve a graph of the probability distribution verses wavenumber quotient, a dimensionless quantity that is k/k_0 . The distribution of the probability over the local wavenumber to the global wavenumber maximum goes to demonstrate the issues with the local wavevector method. It shows that for a random field there will always be a local wavenumber of 0. This essentially corresponds to some kind of offset which would uniquely identify each function, even if that offset is 0.

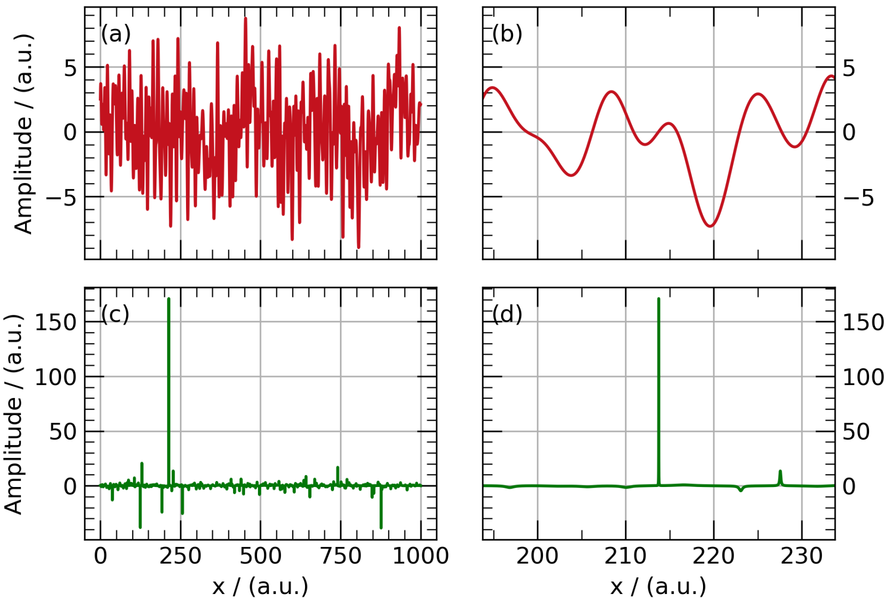

Figure 5.1: A figure showing 4 panels demonstrating (a) the Full Wave across a range of $[0, 1000]$; (b) the Restricted Wave, where we take a section around the highest metric values from the wave to look at the wave around that point; (c) the Full Metric, which demonstrates what values the Berry metric takes on and where; and (d) the Restricted metric which shows the metric in and around the highest peak of the metric. This figure clearly shows the flaws in the metric, as it achieves values far higher than $k_0 = 1$ in many different places, but also shows how if you only look within certain regions, it is possible to miss the majority of the divergent behaviour.

5.2.1 Simulations

The replication of this study was conducted on University of Nottingham's HPC, Ada, using 5×10^5 different random fields of 50 random frequencies. In our simulations we wanted to reproduce the methods implemented in Berry's paper, and so we generated datasets with a large number of random amplitudes and frequencies, with amplitudes ranging anywhere within the complex unit circle and frequencies being distributed as per the paper, randomly within the two intervals $[-1,\ -0.99]$, $[1,\ 0.99]$, so $k_0 = 1$, with 25 frequencies within each interval. We also made sure to use their algorithm, as given in equation 5.9, to calculate the local wavevector to be as accurate to their method as possible. However, a numerical l'Hôpital's method was introduced to try and deal with any situations in which a direct computation of the local wavevector method might fail.

Initial runs of this method were run between an x variable of $[-200, 200]$ to try and capture superoscillations, however it was observed that the values of $P_{1\ super}$ was not converging to the correct value. It was then that the domain over which the function was analysed was increased to $[-1000, 1000]$ and the fraction of fields that met the metric for superoscillation also increased. This is likely because this is how long it takes for the very small aberration from monochromaticity to start to dephase properly. This dephasing is what typically causes the Berry metric to increase to a value beyond the bandlimit of k_0 that is implemented. From our simulations we could not seem to retrieve the value that Berry et al. achieved, and despite checking the method multiple times it still seemed resistant to our attempts at replication. However, when the range was changed to that which was presented in the figures showing the superoscillations in the paper, this $[180 - 200]$ range, we began to get close to the values quoted. When investigating in this range the probability found was $P_{1\ super} = 0.31$ for 5×10^5 fields, which whilst close is not exact. It is suspected that only a limited range of investigation was used in these calculations, and whilst this is a necessity of the numerical methods, an investigation of the range at least on the order such that the aberration from monochromaticity can dephase. Given that chromatic aberration $\delta = 1 \times 10^{-3}$, this means that it dephases and has a periodicity of around 1000, and so an investigation in and around this range must be conducted to avoid missing superoscillatory behaviour in this metric.

Not only do these graphs show that the Berry method seems to diverge within the range of $\pm 1/\delta$ they also show that the waves can take on a variety of different shapes within the range that is investigated. Even limited range investigations give rise to a wide variety of different wave shapes over their range, as can be seen by comparing figures 5.2 and 5.1.

One of the other ways of comparing the Berry paper to the results that were obtained through simulation was trying to match the curves for probability retrieved. These

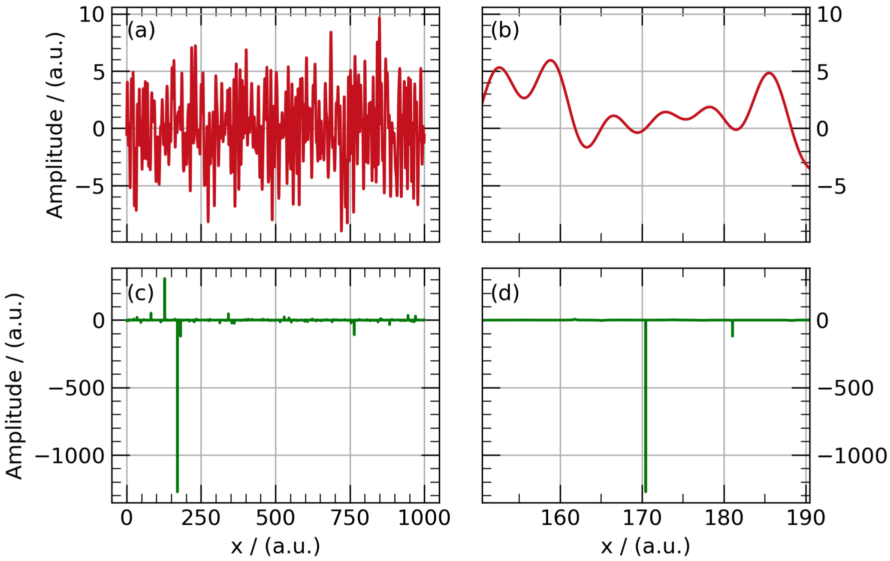

Figure 5.2: A figure showing the results of the initial runs of the Berry reproduction simulation. The different panels show (a) the Full Wave, (b) the Restricted Wave, (c) the Full Metric, and (d) the Restricted Metric. This figure clearly shows the divergence of the metric above $k_0 = 1$

k/k_0 curves show the probability that a particular local normalized wavenumber occurs within the field. The graph in the Berry paper is a Gaussian distribution, with the probability of a local wavenumber of 0 being $P_1(0) = 1$ [11]. This probability curve was something that was of interest to try and recreate, as it seemed to heavily support their conclusions.

The graphs in figure 5.3 are analogue histograms for the probability curve in Berry's paper [11]. In order to find the associated probability we would have to integrate across the entire histogram and then divide by that value. This would lead to a better representation of the probability of a particular histogram range occurring within the random field. It is, however, clear to see the difference in shape between Berry's method's curve, as seen in figure 5.3, and the curve that we find, as seen in figure 5.4. Even on the restricted range graph in figure 5.3(b) it is evident that nowhere near the amount of local wavenumbers above 1 are achieved in our attempts than the Berry paper.

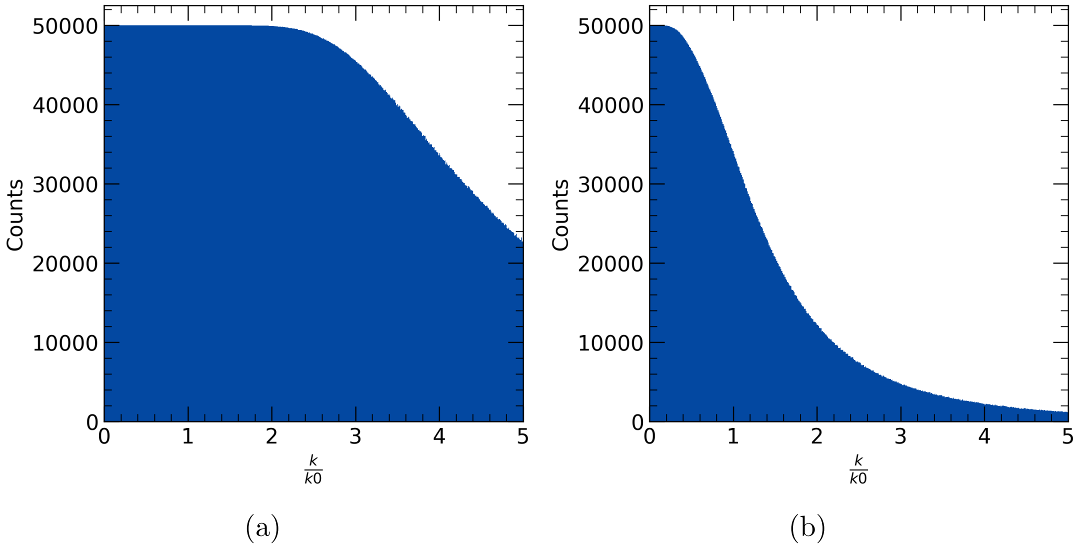

Figure 5.3: Graphs showing the difference between the histograms of the various local wavevectors found using the Berry method over different windows (a) a range of $[0, 1000]$ and (b) a range of $[80, 120]$. The number of waves this was run over was 50000, and so count values of 50000 correspond to the particular $k/k0$ value occurring in every wave at some point. It is interesting to note that there is any difference, as although this was run on the same data, restricting the range shows how windowing can affect the results.

The reasons for this are a touch opaque, as the simulations were performed to attempt to reproduce Berry and Dennis' work as closely as possible. However, it is possible that the choice of random distributions is to blame for these discrepancies. We chose to distribute our phase and amplitude values within the full unit circle in the complex plane, however it is possible that the distribution used in Berry's paper was different. Given their use of monochromaticity with a deviation of only $\delta = 0.001$ it is possible that the distribution they used was a thin annulus in the complex plane, with outer radius of 1 and inner radius of 0.999. It is also possible that other random distributions were used, such as a unit box, or other random distributions within the complex plane, but it is not known what was used, and thus exactly why there is a difference in results. Further investigation may reveal slightly deeper insights, as Huang et al. highlight that they also find that the Berry and Dennis metric is useful in only specific situations, where the function is locally near or at zero intensity [15]. Results here are unfortunately inconclusive, but do point towards some potentially interesting results that may provide a deeper insight into the nature of superoscillations.

5.3 Analysis Methods

Rather than the Berry approach, we suggest an approach based off Aharonov's formalisms for the Fourier series of one of the superoscillating functions given in equation 2.31. The method comes from performing an overlap integral with a given function, and the equation 2.31:

$$\mathbb{A}(f(x)) = \int_{-\infty}^{\infty} f(x) \left[\cos(\omega_N x) - ig\sin(\omega_N x)\right]^N dx \ . \tag{5.10}$$

This function acts as an analogue to the Fourier transform, and indeed simplifies to this for $g = 1$. If we apply Aharonov's simplification for expressing this function in terms of a Fourier series, then we can start to make some simplifications. Recalling from equation 2.32 the simplification of equation 2.31, we can substitute it in to equation 5.11:

$$\mathbb{A}(f(x)) = \int_{-\infty}^{\infty} f(x) \sum_{j=0}^{N} X_j e^{ih_j x} dx \ . \tag{5.11}$$

Which by the uniform convergence theorem [25], we can simplify to:

$$\mathbb{A}(f(x)) = \sum_{j=0}^{N} X_j \int_{-\infty}^{\infty} f(x) e^{ih_j x} dx \ . \tag{5.12}$$

This is exactly a weighted Fourier transform, whereby each frequency involved is weighted by some term X_j which is given by equation 2.33. Now this is useful for us, only when compared to the Fourier transform, where we compare the Fourier weightings of each frequency to the Aharonov weightings. The reason that we do that is that the Aharonov weightings are a polynomial in the superoscillating metric g but occur at the same locations as the Fourier weightings within the k-space. What is being looked for are singular solutions to the ratio of the Aharonov to Fourier coefficients, where the superoscillating metric is greater than 1. If we consider the polynomials $X_j(g)$ weighted by the Fourier coefficients F_j we want to know if there is a solution for $g > 1$ such that for all j these weighted polynomials have a singular solution. Put another way does there exist a constant c such that $\forall j$ and $g > 1$:

$$\frac{X_j(g)}{F_j} = c \ . \tag{5.13}$$

The ideal solution for this is when $c = 1$ and $g > 1$, i.e the function is exactly in the form of an Aharonov superoscillating function. However, as the coefficients $X_j(g)$ are a quotient of the normalised frequencies h_j whereby the actual bandlimit information f_{max} is divided out in the quotient (this can be seen in equation 2.33 and the definition of g in equation 3.80), there can actually be a scaling factor between X_j and F_j. This scaling factor is exactly c, which accounts for the loss of the bandlimit information in $X_j(g)$. Thus what is being investigated is whether the Fourier transform is similar to the Aharonov transform or if there is a more complicated relationship, or put another way, are the Aharonov and Fourier transforms the same shape, but different scales for a given g.

Put a different way, we want to decompose a function into a sum of superoscillating functions so:

$$f(x) = \sum_{l=0}^{M} C_l \left[\cos(\omega_{N,l}x) - ig_l \sin(\omega_{N,l}x)\right]^N \tag{5.14}$$

which via the Aharonov simplification from equation 2.32 becomes:

$$f(x) = \sum_{l=0}^{M} C_l \sum_{j=0}^{N} X_{j,l} e^{-ih_{j,l}x} \ . \tag{5.15}$$

Thus for to find C_l and $X_{j,l}$ we can compute the overlap integral:

$$C_l = \sum_{j=0}^{N} X_j \int_{-\infty}^{\infty} f(x) e^{-i(\omega - h_{j,l})x} dx \tag{5.16}$$

which is exactly the Fourier transform with respect to $h_{j,l}$, which are arbitrary frequencies. Thus we have that:

$$C_l = \sum_{j=0}^{N} X_{j,l} \int_{-\infty}^{\infty} \int_{-\infty}^{\infty} f(x) e^{-i(\omega - h_{j,l})x} \delta\{\omega - h_{j,l}\} dx d\omega \tag{5.17}$$

Assuming that we have a band-limited frequency function of a finite number of frequencies, then we can use the Fourier transform to find both N and the frequency set that we are working with, fixing $h_{j,l}$. Fixing the frequencies also has the consequence of fixing l. Thus:

$$C = X_j F_j, \ \forall j \tag{5.18}$$

Where F_j are the Fourier weightings of each Fourier frequency, given by:

$$F_j = \int_{-\infty}^{\infty} \int_{-\infty}^{\infty} f(x) e^{-i(\omega - h_j)x} \delta\{\omega - h_j\} dx d\omega \tag{5.19}$$

What this equation shows is that the function will superoscillate if the Fourier coefficients multiplied by the Aharonov coefficients for each frequency are a constant value C. This is essentially a scaling factor for the Fourier Transform and the Aharonov transform, meaning they must be similar, but differ in amplitude only by some constant C. This C has no restrictions on it, thus $C \in \mathbb{C}$.

This problem has been tackled using numerical approaches, and some previous work by Konrad and Roux [24] to limit the search space. Given that a superoscillating metric of $g > 10$ is vanishingly small as to be extremely unlikely, we only consider a search space of $g \in (1, 10]$ and see if there is a stable solution for c across all N values of $X_j(g)/F_j$ evaluated at g.

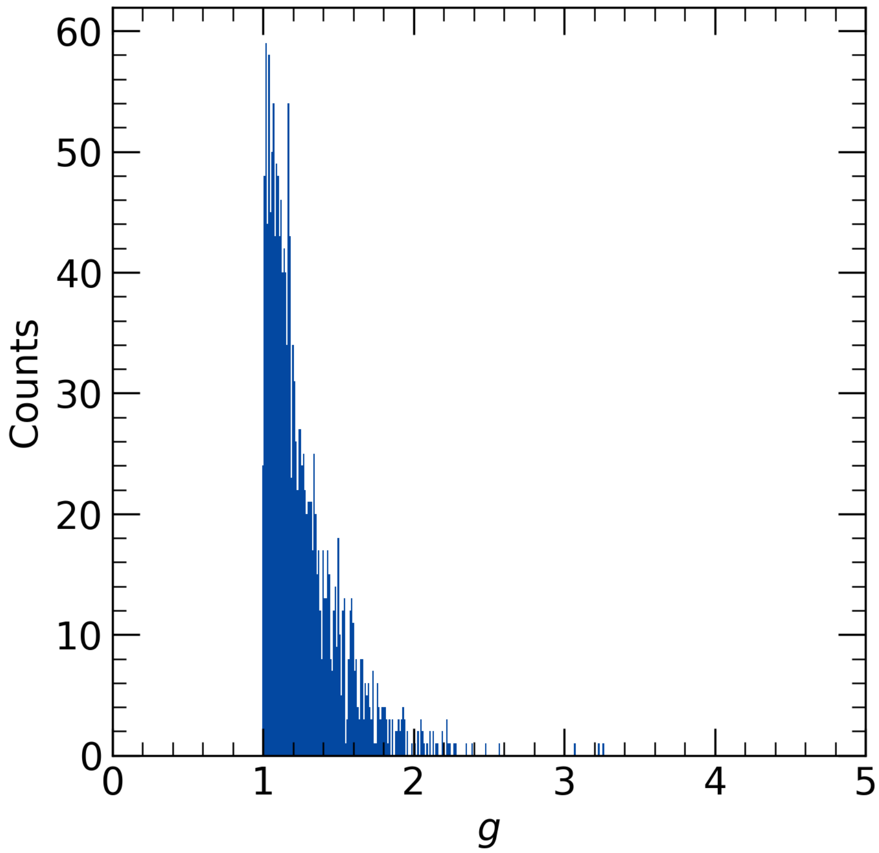

Figure 5.4: A histogram showing the distribution of superoscillating metric g values and the number of times they appear within a random field over a set of $50,000$ random fields. This graph was made using the novel detection method detailed in section 5.3. There are a total of 1717 counts here, which corresponds to a super-oscillatory probability of $P(g > 1) = 1717/50000 = 0.03434$

This search for a single c value across all of the Fourier and Aharonov values at a given g leads to some interesting insights. As the algorithm searches, it has an error associated with the calculated c values. This error can be considered a tolerance, and as we relax the tolerance, the larger the fraction of the total fields appears to superoscillate. This is because whilst superoscillations are relatively robust to small perturbations, this noise that occurs does add error onto our total fraction. The balance between the tolerance such that numerical error doesn't lose all superoscillatory fields and does accept too many non-superoscillatory fields is a difficult one to strike. It was decided that the tolerance for the amplitude search should be 1×10^{-4} as it was small enough so as to reduce false positive and is on the same order of magnitude as the $N = 50,000$ so can reduce the number of possible false negatives.. This lead to retrieving a final fraction of the 1D random complex fields as being 0.0032. Now what this actually states is not what fraction of random fields superoscillate, but rather, what fraction of random fields are an Aharonov class superoscillation.

As can be seen in figure 5.4 there is a distribution of g across the random fields, with the most likely superoscillations being those much closer to $g = 1$. This is as we would expect, because by all accounts and especially [24], higher superoscillatory frequencies are exponentially suppressed. As we can see an exponentially decreasing relationship between the number of counts and g, where, even accounting for noise, it's shape is fairly visible from the histogram

Whilst the Aharonov class superoscillations are a large class of superoscillations, they are not the only ones. As was discussed in chapter 2, the basic superoscillating function as described in 2.16 does not belong to this class of functions. In fact as it is defined in terms of a variable s the basic superoscillating function does have a value range of s such that it is part of the Aharonov class of superoscillating function. That range has $s \in [0, 0.25)$ and any values beyond this are not valid Aharonov class functions. However, it is not restricted to being a part of this class of superoscillating functions.

Another way of analysing functions is to use the Aharonov supershift principle. This would allow for analysis of compactly supported, but continuous Fourier spaces, as although bandlimited, there are infinite frequencies. As the previous method relies on a finite number of frequencies, as shown in the exponent N of equation 5.14, the following method based on the supershift principle gives an approach that allows for analysis. This supershift approach would look something along the lines of:

$$f(x) = \sum_{j=0}^{N} Y_j G(\beta_j x) \ , \tag{5.20}$$

where as shown in section 3.4.1, $G(x)$ is some orthogonal basis function, β_j is some bandwidth associated with the basis function, and Y_j is their amplitude, thus would be given by the Aharonov formulation:

$$Y_j = \prod_{\substack{k=0 \\ k\neq j}}^{N} \frac{\beta_k - \alpha}{\beta_k - \beta_j} \ , \tag{5.21}$$

and by the overlap equation:

$$Y_j = \int_{-\infty}^{\infty} f(x) G(\beta_j x) dx \tag{5.22}$$

This does not unfortunately simplify to a Fourier transform in all cases, however can provide valuable insight into whether a function superoscillates as an Aharonov class superoscillation. It is also important to note that β_j are not as simple as the Fourier bandwidths of the frequency functions for the function under investigation, it can be a more complicated relationship and is instead based on the Fourier bandwidths of the basis function $G(x)$. Again this has not been fully explored, but is another possible tool that can be used in trying to detect superoscillations in signals and fields that are otherwise difficult to measure.

5.4 The Aharonov Transform

It has been shown that in equations 5.11 and 5.12 given that the superoscillatory metric $g \to 1$ they simplify to the Fourier transform. This admits the possibility of treating the Aharonov transform similarly to the Fourier transform, especially in explaining how and why the Aharonov transform is so similar. A normalised windowed Fourier transform of a function can be considered the centre of mass of a rotating vector $e^{-i2\pi\zeta t}$ multiplied by the function itself $f(t)$ over a given interval $[a, b]$. To explicitly state this formula, it is:

$$\hat{f}(\zeta) = \frac{1}{a-b} \int_b^a f(t) e^{-i2\pi\zeta t} dt \tag{5.23}$$

where ζ is our transform variable or, put another way, our winding frequency, and $[a, b]$ is some arbitrary interval over which the function $f(t)$ is defined. This differs from a Fourier transform in some minor ways, one is that it is windowed and therefore it is not performed over the entirety of the domain over which $f(t)$ is defined. The other is that it is normalised by the length of the interval, so that we bound $\hat{f}(\zeta)$ to the same range as $f(t)$, such that for all the t and ζ domains, $|f(\zeta)| \leq |f(t)|$. The reason we choose this form of the Fourier transform is that it is closer to the algorithms used in the numerical computations used for the discrete Aharonov transform and the algorithms discussed in section 5.2.

The essence of the Aharonov transform is that instead of wrapping the function around a circle, we instead wrap it around an ellipse with an eccentricity related to the superoscillatory metric g. When considering the wrapping function $w(t, \zeta) = f(t)e^{-i2\pi\zeta t}$, we can split these functions into their real and imaginary components to act as analogues to functions along the classic Cartesian coordinates x, y. These functions are:

$$u(t, \zeta) = \Re\left(f(t)e^{-i2\pi\zeta t}\right) = \Re(f(t))\cos(2\pi\zeta t) - \Im(f(t))\sin(2\pi\zeta t)\ , \tag{5.24}$$

and

$$v(t, \zeta) = \Im\left(f(t)e^{-i2\pi\zeta t}\right) = \Im(f(t))\cos(2\pi\zeta t) + \Re(f(t))\sin(2\pi\zeta t)\ , \tag{5.25}$$

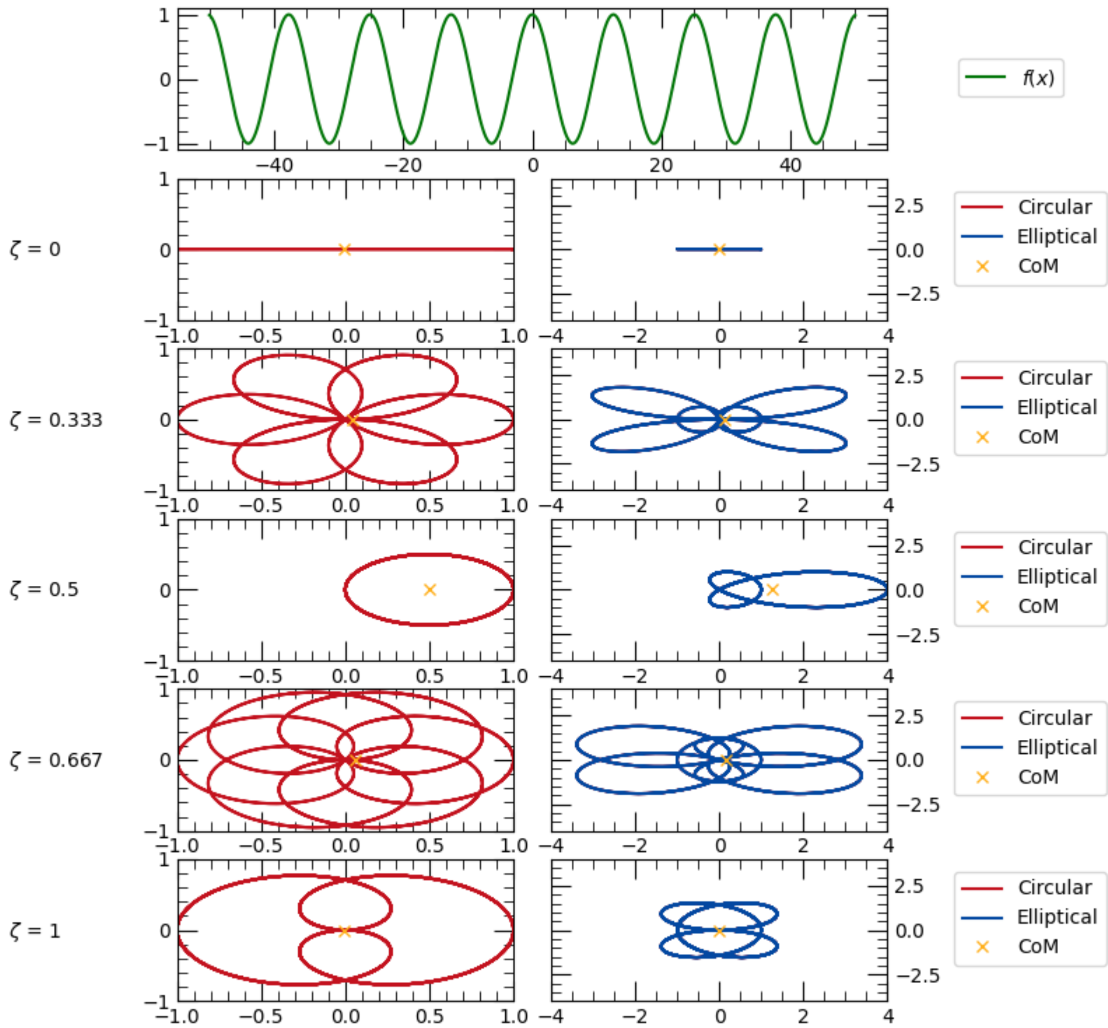

Figure 5.5: A figure depicting the different winding functions $w(t, \zeta)$ (circular) and $\omega(t, \zeta)$ (elliptical) of $f(t) = \cos\left(\frac{1}{2}t\right)$ at different winding frequencies ζ. The centre of mass, depicted by the cross indicates the amplitude of each winding frequency within the function. Most winding frequencies will be near zero, with only those corresponding to Fourier frequencies having a larger amplitude, as can be seen in $\zeta = 0.5$. Here, $g = 2$ and $n = 2$ for the elliptical winding pattern

and follow the relation that:

$$u^2(t, \zeta) + v^2(t, \zeta) = ||w(t, \zeta)||^2 = ||f(t)||^2 \,. \tag{5.26}$$

Given that the imaginary and real components of $e^{-i2\pi\zeta t}$ are weighted equally, this corresponds to a wrapping of the function $f(t)$ around a circle, with a winding frequency of ζ. This can be seen in figure 5.5, where for $\zeta = 0.5$ the centre of mass of the winding function is far to the right of 0 for $w(t,\zeta)$.

However, for our superoscillatory function, $\big[\cos(\omega_n x) - ig\sin(\omega_n x)\big]^n$ we have an imbalance in the real and imaginary components of this function, thus using our Aharonov transform our winding function becomes $\omega(t,\zeta) = f(t)[\cos(\omega_n t) - ig\sin(\omega_n t)\big]^n$. This then decomposed into it's real and imaginary parts is:

$$\begin{aligned}\rho(t,\zeta) &= \Re\left(f(t)\big[\cos(\omega_n x) - ig\sin(\omega_n x)\big]^n\right)\\ &= \Re(f(t))p(t,\zeta) + \Im(f(t))q(t,\zeta)\ ,\end{aligned} \tag{5.27}$$

and,

$$\begin{aligned}\eta(t,\zeta) &= \Im\left(f(t)\big[\cos(\omega_n t) - ig\sin(\omega_n t)\big]^n\right)\\ &= \Re(f(t))q(t,\zeta) + \Im(f(t))p(t,\zeta)\ ,\end{aligned} \tag{5.28}$$

with,

$$p(t,\zeta) = \sum_{k=0}^{m}\binom{n}{2k}(-ig)^{2k}\cos^{n-2k}(2\pi\zeta t)\sin^{2k}(2\pi\zeta t)\ , \tag{5.29}$$

and,

$$q(t,\zeta) = \sum_{k=0}^{m}\binom{n}{2k+1}(-ig)^{2k+1}\cos^{n-2k-1}(2\pi\zeta t)\sin^{2k+1}(2\pi\zeta t)\ . \tag{5.30}$$

Here, $m = \lfloor\frac{1}{2}n\rfloor$, and the $p(t,\zeta)$ and $q(t,\zeta)$ functions are the respective real and imaginary decompositions of the superoscillatory function and we have used that $\omega_n = \zeta$. The same relation is preserved in terms of squaring the elliptical winding function, so:

$$\rho^2(t,\zeta) + \eta^2(t,\zeta) = ||\omega(t,\zeta)||^2 \tag{5.31}$$

but notably, this does not equal $||f(t)||^2$, if instead we consider the real and imaginary parts of $f(t)$, we get a rather more complicated relation:

$$\begin{gathered}\rho^2(t,\zeta) + \eta^2(t,\zeta) =\\ R^2\big[p^2(t,\zeta) + q^2(t,\zeta)\big] + 4RIp(t,\zeta)q(t,\zeta) + I^2\big[p^2(t,\zeta) + q^2(t,\zeta)\big]\end{gathered} \tag{5.32}$$

with $R = \Re(f(t))$ and $I = \Im(f(t))$. If we now consider the treatment of a purely real function, $\rho(t,\zeta) = Rp(t,\zeta)$ and $\eta(t,\zeta) = Rq(t,\zeta)$, and that:

$$q(t,\zeta) = -ig\tan(2\pi\zeta t)\sum_{k=0}^{m}\frac{p_k}{(2k+1)(n-2k-1)} \tag{5.33}$$

with:

$$p_k = \binom{n}{2k}(-ig)^{2k}\cos^{n-2k}(2\pi\zeta t)\sin^{2k}(2\pi\zeta t)\ . \tag{5.34}$$

The reason we highlight this is to show the imbalance between the $p(t,\zeta)$ and $q(t,\zeta)$ functions. Parametrising the space as $(x(t), y(t)) = (Rp(t,\zeta), Rq(t,\zeta))\Big|_{\zeta}$ leads to an asymmetry in x and y. This asymmetry can be expressed as an eccentricity, which is typically given as:

$$\varepsilon = \sqrt{1-\frac{1}{g^2}} \tag{5.35}$$

and is a measure of the difference between the focal points of the ellipse and the central point. For a circle this difference is 0, as the focal points lie on the central point, and as $\varepsilon \to 1$ this becomes a parabola, and then for $\varepsilon > 1$ it is a hyperbola. As can be seen in figure 5.5 with the elliptical winding patterns, there is a difference between the circular and elliptical winding patterns, but importantly the centre of mass behaves the same given the same winding frequency, ζ. The reason this is important is that the Aharonov transform is, as shown in equation 5.18, a scaled Fourier transform, and this means that it will behave in the same way, just with a different amplitude.

This can be seen in figure 5.6, as we use the optimal values for g and n, we have a constant coefficient between the different winding frequencies relating to the Fourier frequencies in the winding pattern. The only big deviations from this are $\zeta = 0$ and $\zeta = 2/3$. As these aren't Fourier frequencies involved in the function, we have no restrictions on what the coefficients between them should be, so we disregard them. Worth noting is that we do not show the winding frequencies of the negative

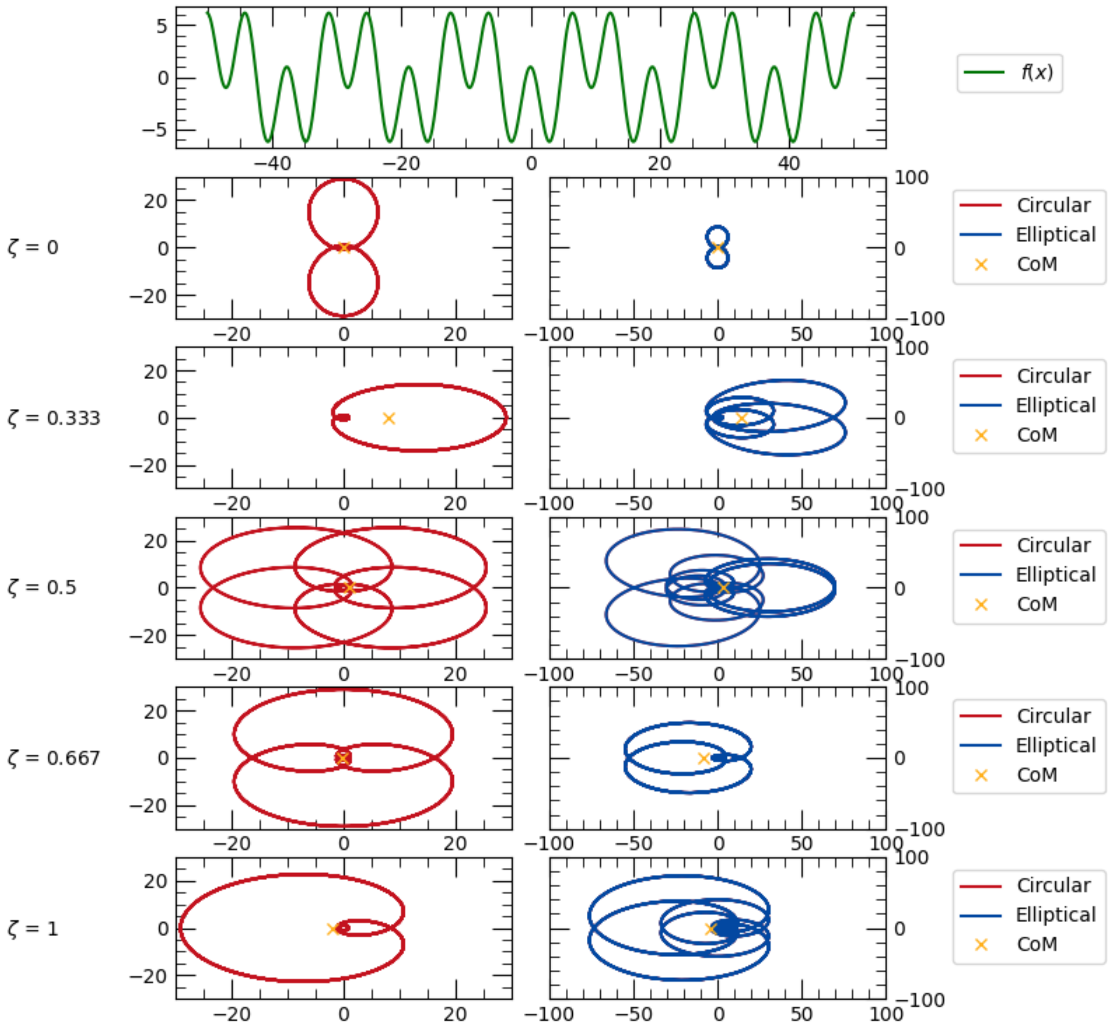

Figure 5.6: A figure depicting the Fourier (circular, red) and Aharonov (elliptical, blue) winding patterns and centre of mass (CoM) positions for an Aharonov function $f(x)$ with $h_j \in \{-1, -1/3, 1/3, 1\}$ and $g = 4/3$. Here, $g = 4/3$ and $n = 4$ in order to get a constant coefficient between the Fourier and Aharonov transforms. That constant relating the Aharonov and Fourier windings for this system is $C \approx 1.85$. We do not consider the contributions of the relationships between $\zeta = 0$ and $\zeta = 2/3$ winding frequencies. The reason for this is that they are not Fourier frequencies of the function $f(x)$ and although, for $\zeta = 2/3$, there are some CoM deviations between Fourier and Aharonov transforms, this is likely because of ringing effects natural in a finite discrete winding calculation. This highlights the importance of using both the Aharonov and Fourier transforms in conjunction.

frequencies. This is because, for this function the negative winding frequencies give the same values for C, just with a negative CoM position. This is not always true, but for the illustrative purpose of showing the ringing effects of $\zeta = 2/3$ it has been left out of the figures.

The usefulness of this is that it nicely shows the easy mapping between a Fourier transform and an Aharonov transform, and how important it is to use both in conjunction. As the Aharonov transform is just a scaling of the Fourier transform, we can try to predict what the coefficient should be by calculating Aharonov coefficients for the Fourier frequencies in the function. To do this we look at equation 2.33 and the h_j described in figure 5.6, and calculate a set of normalised Aharonov coefficients by dividing through by the largest Aharonov coefficient, $max(|X_j|)$, getting a set of $\{X'_j\}_j$ by:

$$\{X'_j\}(g) = \left\{ x \middle| x \in \frac{X_j(g)}{max(|X_j|)} \right\} = \left\{ x \middle| x \in \frac{1}{max(|X_j|)} \prod_{\substack{k=0 \\ k \neq j}}^{n} \frac{h_k - g}{h_k - h_j} \right\} . \tag{5.36}$$

We compare these normalized Aharonov coefficients with the normalised Fourier coefficients, calculated in much the same way as equation 5.36 above:

$$\{F'_j\} = \left\{ x \middle| x \in \frac{F_j}{max(|F_j|)} \right\} . \tag{5.37}$$

This then allows us to find the quotient between X'_j and F'_j which for all j should be constant for the correct g value. This establishes a set of n simultaneous equations which can be expressed as:

$$\begin{pmatrix} X'_0(g) \\ X'_1(g) \\ \vdots \\ X'_n(g) \end{pmatrix} = \chi \begin{pmatrix} F'_0 \\ F'_1 \\ \vdots \\ F'_n \end{pmatrix} . \tag{5.38}$$

This approach allows for easier computation using parallelised computing, as searching for χ for each set of fields as established in section 5.2 becomes much easier compared to precisely solving all n of these equations.

There is also possible future work in trying to establish a way to reduce the search space based on the eccentricity equation of the Aharonov winding ellipse; however, at this point, this research has not been conducted. It could however help reduce the computation time significantly, by aiming to calculate eccentricities, rather than individual Aharonov coefficients.

Chapter 6

Conclusions

In this chapter we discuss the simulated and analytical results that have been achieved throughout this thesis, where there is room for improvement and future work, and then conclude with a discussion of the impact, potential uses and whether the questions that were asked at the beginning of this project have been answered.

6.1 Design and Detection Results

To summarise the results of this thesis, we have managed to show that: superoscillating acoustic apertures are possible, not only this but superoscillating diffraction gratings are possible. We then designed some apertures for testing, mainly using the ease of computation with the slit apertures to create a variety of superoscillating aperture designs. These were then simulated to test the validity of the designs and to ensure that there was more evidence for manufacturing before the experiments were conducted.

The initial designs were a naive foray into designing superoscillatory apertures but did allow for a lot to be learned about the process. This process was then refined using slit apertures, as they were the simplest to compute the analytical diffraction pattern for, and so were used as a benchmark to help design and test the methods that were used in the rest of the design process. This led directly to the SDD style designs and these were extremely informative in their design. Especially SDD2 and SDD3, as these diffraction gratings were merely meant as a way to test simulation and analytical calculation against experiments. These, however, also turned out to superoscillate, as well as the initial SDD1 design. This was intriguing as a previously retrieved result, specifically the one mentioned in section 3.3.1 and equation 3.49, had been interpreted incorrectly, as it was thought this meant that diffraction gratings could not superoscillate. Instead what it seems to imply is that diffraction gratings can only superoscillate at or below $a+k_{max}$. This realisation lead to the developments of the proofs that are given in the Apertures chapter, chapter 3, as well as the investigation into perturbations of degeneracies in the design equations that lead to the IDD designs.

The IDD designs were meant as an investigation of what happens with degenerate solutions of the design equations. They provided an intriguing look into how successful the design equations are, but also highlighted that not every solution that is achieved does superoscillate. This is an incredibly interesting result as this was not expected, as the design equations seemed to be built specifically for superoscillatory behaviour. Thus it seems that there may be a more complicated relationship between superoscillatory behaviour than these design equations encapsulate.

The Detection chapter, chapter 5 has some very interesting results. In it we critique previous detection methods, and show the windowing issues that the Berry local wavenumber method runs into. This is seen in section 5.2, and shows how the histograms produced are similar to the probability curves published in their paper [11]. We also develop new methods for detecting specifically Aharonov class superoscillations on the same data that the Berry methods were run, and we present those results in section 5.3. These results showed that Aharonov class superoscillations are very rare, occurring in only about 0.3% of $50,000$ random fields, with an aberration from monochromaticity of $\delta = 0.001$.

To discuss the best design it is pertinent to consider what the best metric is. There is the obvious metric of the highest superoscillatory frequency, in which case the best design is $IDD1$, however, this is not necessarily the best metric. This is due to the nature of superoscillations. The higher the superoscillatory frequency, the lower the detectability, and so we wish to look for superoscillations with the best SNR. To start, let us examine those superoscillations with the lowest superoscillatory metric, g. In this regard $EDD2$ is a natural starting place, and we find that the maximum SNR, i.e the amplitude of the superoscillation, compared to the amplitude of the function maximum is roughly ≈ 0.038. If we compare this now to the SNR of $SDD2$, the second lowest g, we can see that $EDD2$ has a much better SNR as for $SDD2$, the SNR is ≈ 0.01. This pattern continues for most of the other arrays, and so we can say that for the best maximum signal to noise ratio (SNR) that $EDD2$ is the best array design. It is, however, important to note that this compares the maximum of a sincusoidally decaying function, which always happens at the centre, with the maximum amplitude of a the quickest superoscillation. There are often other, slower superoscillations, which achieve a better SNR than the quickest superoscillation, but here we are interested in achieving the maximum possible superoscillatory frequency, in theory. In practice however this runs into issues of detectability and thus a system would have to have a maximum SNR sensitivity of at least greater than ≈ 0.03 in order to detect the superoscillations produced in $EDD2$.

6.2 Future Work

There are lots of potential avenues of investigation that can be conducted post this thesis. For one refinement of further aperture arrays and investigation into aperture arrays of different shapes other than slits, as was discussed in section 4.1.1. It has been shown by Toraldo di Francia and Rogers et al. superresolving annular aperture arrays are possible [1, 16], and as such there is much to be developed in terms of the theory in this thesis. Aperture arrays based on annular apertures, circular, or even arbitrary shaped apertures could be developed using the framework we have set out. Basing it either on the Aharonov supershift method or controlling the zeroes method, there are many benefits to developing the theory beyond just slit apertures, as it means that a greater portion of the field can superoscillate, greater control over the superoscillatory region, and better control of the amplitude ratios can be achieved. Annular apertures could be of particular interest as it is possible that the design style of concentric annuli could lead to vast simplifications in the process of design. These methods are similar to the metalens and pupil filter (PF) approaches taken in Rogers et al's review on mathematical methods for superoscillations [19]. This offers very exciting new possibilities into designing both aperture arrays and understanding superoscillations better in general.

Other potential applications of superoscillations are so wide ranging and varied that they encompass as many fields as there are uses for imaging and detection. However, one of the most interesting and tangible uses for superoscillations would be in using it for x-ray crystallography subwavelength scattering. If it can be shown that a superoscillatory input can scatter off some feature too small for the highest Fourier frequency, then it can be shown that superoscillations have a huge role to play in NDT. It would also show how important incorporating superoscillatory analysis into a variety of different fields would be. Although superoscillations have been demonstrated experimentally [16], it is still in its infancy as a field in terms of application.

Beyond probing crystalline structure, it would be of great interest to try and develop a theory of anisotropic superoscillations, especially for acoustic applications. It is curious to consider highly anisotropic substances when discussing superoscillations as features such as phonon caustics [21], seem to imply a sort of natural superdirectivity when it comes to certain substances. This has not been fully explored, but given that a material naturally has a bandlimited number of wavenumbers and vectors that can be supported, it is not obvious why naturally occurring superoscillatory materials could not exist due to their crystal structure. Indeed it would be very interesting to try to develop a metamaterial or similar substrate that produces superoscillation exclusively, given certain ranges of inputs. Similar to a superlattice, where instead of producing very coherent phonons of a single wavelength to then propagate into a material, this superlattice would produce polychromatic phonons either dephased in the right way to superoscillate, or of coherent phonons of varying amplitudes, such that their superposition would superoscillate. Indeed designing these metamaterials may give insight into crystal structures that could be used to help identify natural crystal formations.

An enormous and prevalent field of research that superoscillations could be used in is communications. Communications has many aspects from the physical transport of the information across distances, to encryption, decryption and improving bandwidth limits for more information to be transmitted down communication lines. Superoscillations have applications in all of these fields, however two of particular interest are those pertaining to the Nyquist rate, and cryptography.

The Nyquist rate is the lowest rate at which a continuous-time signal can be sampled to produce an aliasing free discrete representation or the lowest sampling rate at which a signal can be reconstructed perfectly without losing information [29]. Superoscillations, being a phenomena which exploits the bandlimit could prove to be an interesting tool to try and beat the Nyquist rate. If this works, it may allow for more information to be communicated down the same lines with little to no disturbance to infrastructure. This could hopefully be achieved with a simple retrofitting of different algorithms and communication protocols. This avenue has not been fully explored, however, given that superoscillations can beat the Rayleigh criterion for diffraction, it would not be too large a stretch to apply the same hope for the Nyquist rate being beaten.

Cryptography is a curious use case for superoscillations, but there are some interesting applications. Given that superoscillations can be used to encode most any signal within the superoscillatory region, it makes sense that there is a way to encode and decode a signal into superoscillations given a shared basis set of frequencies. The premise is that a superposition of superoscillatory functions could produce any signal within a given local region. If the set of frequencies that are producing this are known, then a select number of those frequencies can be transmitted with all the information needed to decrypt the message, and as long as the set of frequencies being used isn't known to an interceptor then it isn't possible to decrypt the message. This could also provide a form of tamper proofing, as theoretically it would be possible to know the decay of certain frequencies over given ranges (given ideal conditions). It is also perhaps possible to then ascertain by travel times, phase shift, and other information associated with the decay of the amplitude of waves, as to whether the signal has been intercepted and retransmitted. This potential tamper proofing, and encryption of the wave such that even if intercepted, without the decryption key the information is entirely unreadable means that combined with other encryption algorithms on the data, a signal could be doubly encrypted, and even harder to decode. Again no further work has been done on this, and this is conjecture based on the properties of superoscillations, but it does provide some curious applications that could be investigated further.

Associated with the cryptography work that could be done, is expanding further on the detection work as mentioned towards the end of section 5.3. We could try to expand the class of detected superoscillations from just basic Aharonov class superoscillations to include the basic superoscillatory function, as mentioned in equation

2.16 and even try to account for supershifts. The supershift work would be very interesting, as it would mean that there could be a far wider application of this detection method than just signal processing with sin and cos.

6.3 Conclusion

Here we look to summarise the work achieved in this thesis and examine whether the questions set forth at the start have been achieved. The salient research of this work was in designing superoscillatory acoustic aperture arrays. These arrays, addressed in the Apertures chapter, 3 and Results chapter 4, with the best designs to be produced being $IDD1$, for the highest superoscillatory metric g, and $EDD2$ for the best SNR.

Then there is the results achieved in the Apertures chapter 3 where we show that superoscillatory diffraction gratings can exist, and what the theory behind designing them is.

Finally we have the detection work, presented in the Detection chapter 5, where we highlight issues with the previous detection methods for superoscillations, which still have use in certain circumstances, and suggest a method to improve on these techniques. This is supported by a recalculation of Berry's probabilities for near monochromatic 1D fields [11], retrieving a probability for $P_{1\ super} = 0.03434$ rather than Berry's $P_{1\ super} = 0.29289$.

Thus we come to concluding whether we have addressed and answered the questions set forth in section 1.1. To reiterate the first and perhaps the most leading question asked, but also the most important: Are superoscillating acoustic aperture arrays possible? The answer is: theoretically, yes. This is supported by the evidence given in tables [6.3,6.3], and chapters [3 & 4]. It is important to note that not all acoustic aperture arrays will superoscillate, and indeed we have shown that there are a some diffraction gratings that do not, explicitly as seen in section 3.3.1. We have subsequently shown that some diffraction gratings can superoscillate, section 3.3, and have expanded that idea into full slit aperture arrays. The method that has been detailed in the aperture design sections, sections [3.4, 3.4.1], can and could be expanded to more aperture shapes, such as circular or annular apertures. However, this has not been fully developed, and the simulations that were performed of these early designs fall short in accuracy, due to the complexity of the designs, and the difficulties with detection, the work of which was fleshed out after the early work.

If more were to be done, numerically simulating these designs using FEM rather than Fourier techniques would likely yield better results. It is likely that given a circularly symmetric system that can be reduced down to a linear problem, that the same solutions for the slit apertures could be applied, as the superoscillations would occur in the direction chosen for the solved offsets. This possibility has not been rigorously investigated, and it is likely that the boundary imposed by the out of line symmetry from the simplification could introduce some aberrant effects that interfere with the superoscillatory conditions. However, reflection symmetry about the origin line shows that there is only a reinforcing effect to the superoscillations in the initial SDD designs and so that can be generalised to any kind of symmetry that the system might have.

Secondly, can we detect the superoscillations produced by these aperture arrays? This is a complicated question, as theoretically, the answer is yes, but they are difficult to detect. This is shown throughout the detection chapter, and is supported by the results in tables 6.3 and 6.3. However, experimentally, from the preliminary runs, it was difficult to detect the superoscillations, due to the high SNR. This was attempted to be remedied by the SDD and IDD designs, however, the results were unfortunately lost and so it is unkniwn whether this helped the SNR.

The question of whether we can create a framework to design superoscillatory acoustic aperture arrays has been the focus of a large part of this thesis, and so have we answered it? Given the details in chapter 3 and the results in chapter 4 it is safe to say that we have answered this question thoroughly, and developed a framework,a s well as working examples of superoscillatory acoustic aperture arrays, at least from a theoretical perspective. However, as can be seen from discussion in section 4.2, there are some patterns from the design equations that do not produce superoscillatory diffraction patterns. This was unexpected, and answers yet another one of our questions, do the designs always produce the patterns we expect them to? The designs seem to, but the design equations don't always make superoscillatory patterns

This brings us nicely to the next question, as to whether we have been able to manufacture them, and whether they are manufacturable designs. The EDD designs were produced by optical lithography, as can be seen in figure 2.2 and the IDD and SDD designs were tested on the DMD before running the experiments on them. This means that the designs are manufacturable and testable. However, the biggest limitation to these processes are the spatial limitations of the DMD, or previously the substrate that was being used. These severely limit the number of solutions,as well as the number of slits that each array can have. This in turn means that the freedom and optimisation options available for designing the arrays are limited as well. The spatial restrictions were the biggest limitation in designing the aperture arrays for the experiment, but did allow for the narrowing of the search space.

Finally, the last question of whether we can detect superoscillations in general. This is a complicated question once again, because we have shown that previous methods leave open some potential avenues and often are victim to other aberrant features, such as windowing issues or unbound Fourier spaces. These issues we attempted to address with the novel detection methods detailed in section 5.3 and we managed to achieve detecting Aharonov class superoscillations with the possibility of using similar methods to detect other classes of superoscillations. So whilst in part we are able to detect superoscillations, it is not a complete tool for detecting all superoscillations.

Thus how has the work presented in this thesis compared to the questions that were highlighted at the start. Whilst, most have been answered in some measure or another, there is still a large amount of potential avenues to investigate, and a lot of these, from some that lead directly from this work, like expanding the classes of detectable superoscillations, to more speculative work, such as that on cryptography, have been detailed in the previous section 6.2. It is exciting to see what potential routes the work presented in this thesis might open, and what follow on work there will be to conduct.

Appendices

Appendix A

The majority of the following is standard set theory notation, and is best explained with notation. We describe an interval as the set of points in any field between two limits, a and b. This can be denoted in two ways, open (a, b), where all points in this interval are given by $a < x < b$, and closed $[a, b]$, where all points in this interval are given by $a \leq x \leq b$. This notation can also be mixed for half-open sets. To give a full set treatment to this we consider that $\{x\}$ is a set of points determined by the interval $[a, b]$:

$$\{x\} = \{y \mid y \in [a, b] \subset \mathbb{R}\} \tag{1}$$

which can be read as the set $\{x\}$ is described by all points y given that, which is denoted by $|$, y is in the closed interval $[a, b]$, which itself is a subset, denoted by the $\subset$, of the real number line, $\mathbb{R}$. Another process we may be interested in is combining or restricting sets, which can be considered in much the same way as Venn diagrams, as seen in figure1. In this we can see the different set notation that might be used: union,

$$A \cup B = \{x \mid x \in A \text{ or } x \in B\} \; ; \tag{2}$$

intersection,

$$A \cap B = \{x \mid x \in A \text{ and } x \in B\} \; ; \tag{3}$$

set difference,

$$A \setminus B = \{x \mid x \in A \text{ and } x \in B^c\} \; ; \tag{4}$$

where here B^c denotes the complement of B, given by,

$$B^c = \{x \mid x \notin B\} \; , \tag{5}$$

where $x \notin B$ means that x is not in B.

Other notation that is used is that of supremum, sup, the largest object in an

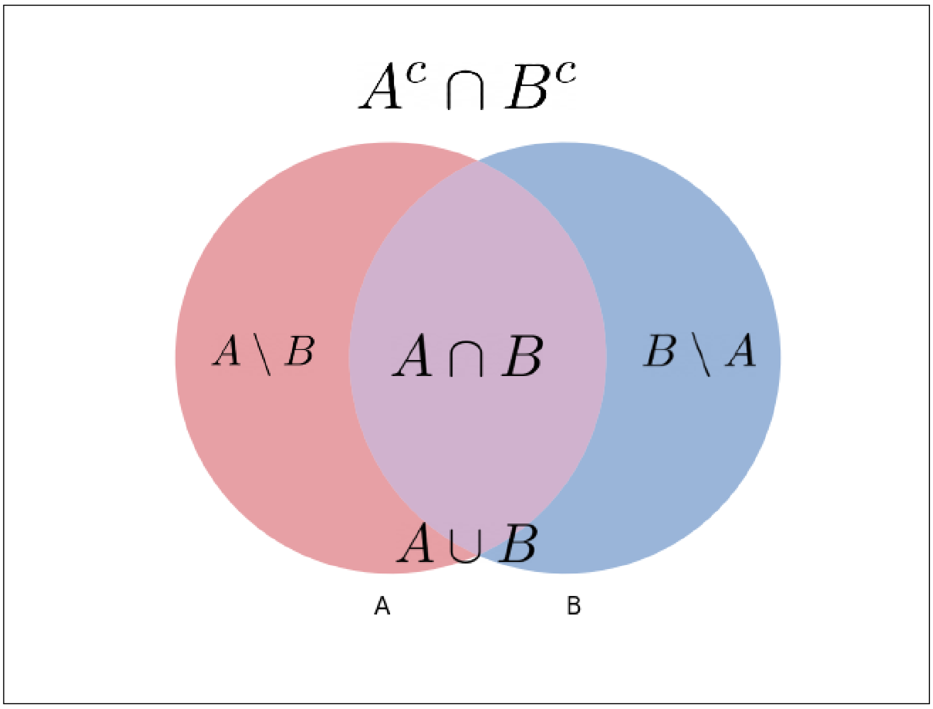

Figure 1: A figure illustrating the different set notation that may be used in the following chapters. The circle on the left is set A, and the circle on the right is set B. The purple area in the middle is the intersection of the two sets, $A \cap B$. The two circles and their intersection is the union of the two sets $A \cup B$. The purely red area of set A is the set difference of $A \setminus B$, and the purely blue are of set B is the set difference of $B \setminus A$. The white area is then the intersection of the two complements of the sets, $A^c \cap B^c$

ordered set; infinum, inf, the smallest object in an ordered set and their limiting forms $\limsup$ and $\liminf$ which are the least upper bound (LUB) of the set, and the greatest lower bound (GLB) of the set, both of which may or may not be in the set. To give an example, let us examine two intervals $(a, b) \subset \mathbb{R}$ and $(a, b) \subset \mathbb{R}$. These two would appear to be the same from initial inspection, but their openness and closedness is very important, as $\sup((a, b))$ does not exist, but $\sup([a, b]) = b$. However, $\limsup((a, b)) = b$ and $\limsup([a, b]) = b$ also. This shows the difference between the open and closed sets, as well as the limiting forms of the supremum and infinum as opposed to their normal forms.

Appendix B

In the following section we will outline the calculations for showing that the bandwidths for each slit is:

$$b_s = \beta_s + k'_{max} \tag{6}$$

First we start with the restrictions on the set of centre point $\{c_j\}_j$ and $\{\beta_j\}_j$ from section 3.1, these constraints allow us to construct $\{c_j\}_j$ as a function of β_j by introducing a new variable that accounts for the distance between the edges of the apertures $\{\epsilon_{j'}\}_{j'} \subset \mathbb{R}^+$ where as we are considering the gaps between the apertures, we have the dummy variable $j' = j,\ \forall j > 0$ which leads us to construct our relation between c_j and β_j:

$$c_j = c_0 + \sum_{k=1}^{j} \epsilon_k + \frac{1}{2}(\beta_k + \beta_{k-1}) \tag{7}$$

which we can see satisfies the third constraint of our construction:

$$c_{j+1} - c_j = c_0 + \sum_{k=1}^{j+1} \epsilon_k + \frac{1}{2}(\beta_k + \beta_{k-1}) - \left[c_0 + \sum_{l=1}^{j} \epsilon_l + \frac{1}{2}(\beta_l + \beta_{l-1}) \right] \tag{8}$$

which when simplified leads to:

$$c_{j+1} - c_j = \epsilon_{j+1} + \frac{1}{2}(\beta_j + \beta_{j+1}) > \frac{1}{2}(\beta_j + \beta_{j+1}) \tag{9}$$

satisfying the third constraint.

In order to find the bandwidth we have to know the least upper bound (LUB) and greatest lower bound (GLB) of the frequencies involved in each of the slits, as such we need to know what frequencies are involved. Thus we pull from section 3.2.1 to get that all the spatial frequencies k' are given by the Fourier transform of the intensity:

$$\mathscr{F}(I(y))(k') = \sum_{j,m=0}^{N} \Psi_{j,m}(k') \tag{10}$$

where $\Psi_{j,m}(k')$ are defined as in equation (3.26). We can see from these equations that the limits of these functions are at $c_m - c_j \pm \frac{1}{2}(\beta_j + \beta_m)$ and thus:

$$LUB[\Psi_{j,m}(k')] = c_m - c_j + \frac{1}{2}(\beta_j + \beta_m) \tag{11}$$

and

$$GLB[\Psi_{j,m}(k')] = c_m - c_j - \frac{1}{2}(\beta_j + \beta_m) \tag{12}$$

which when you substitute the new definitions of c_i in terms of β_i we get that:

$$LUB[\Psi_{j,m}(k')] = \begin{cases} \beta_j + \sum_{l=j+1}^{m} \epsilon_l + \beta_l, & \text{if } m > j \\ \\ \beta_m, & \text{if } m = j \\ \\ -\epsilon_j - \sum_{k=m+1}^{j-1} \epsilon_k + \beta_k, & \text{if } m < j \end{cases} \tag{13}$$

and

$$GLB[\Psi_{j,m}(k')] = \begin{cases} \epsilon_m + \sum_{l=j+1}^{m-1} \epsilon_l + \beta_l, & \text{if } m > j \\ \\ -\beta_m, & \text{if } m = j \\ \\ -\beta_m - \sum_{k=m+1}^{j} \epsilon_k + \beta_k, & \text{if } m < j \end{cases} \tag{14}$$

and thus the bandwidth $b_{j,m} = [LUB - GLB](\Psi_{j,m}(k'))$ which leads to:

$$b_{j,m} = \begin{cases} \beta_j + \beta_m, & \text{if } m > j \\ 2\beta_m, & \text{if } m = j \\ \beta_j + \beta_m, & \text{if } m < j \end{cases} \tag{15}$$

which is simply $b_{j,m} = \beta_j + \beta_m$.

This result can also easily be seen from the difference between equations (11,12), so why have we gone to the effort of expanding in terms of c_i? The answer to that is to help with the case for finding b_s as is required in section 3.2.2. In that section we have that the frequencies associated with each aperture are

$$h_s(k') = \sum_{m=0}^{N} \Psi_{s,m}(k') \tag{16}$$

so to find the bandwidth of each aperture, we have to know the LUB and GLB, thus we have:

$$LUB\left(\sum_{m=0}^{N} \Psi_{s,m}(k')\right) = sup(LUB[\Psi_{s,m}(k')]) \tag{17}$$

which by substituting equation (13) in we can see that since both β and ϵ are positive (this is why we expand in terms of c_i) that the largest of these terms is always when $m > s$ and thus:

$$LUB\left(\sum_{m=0}^{N} \Psi_{s,m}(k')\right) = sup\left(\beta_s + \sum_{l=s+1}^{m} \epsilon_l + \beta_l\right) = \beta_s + \sum_{l=s+1}^{N} \epsilon_l + \beta_l \tag{18}$$

where $m = N$ as we are trying to find the supremum of this set and N represents the largest value that m can take, leading to the most terms in the sum. A similar line of logic can be applied to find $GLB\left(\sum_{m=0}^{N}\Psi_{s,m}(k')\right)$ leading to:

$$GLB\left(\sum_{m=0}^{N}\Psi_{s,m}(k')\right) = inf(GLB[\Psi_{s,m}(k')]) \tag{19}$$

Thus substituting equation (14):

$$GLB\left(\sum_{m=0}^{N}\Psi_{s,m}(k')\right) = inf\left(-\beta_m - \sum_{k=m+1}^{s}\epsilon_k + \beta_k\right) = -\beta_0 - \sum_{k=1}^{s}\epsilon_k + \beta_k \tag{20}$$

where we use the value of $m = 0$ as we once again want to maximise the number of terms in the summation to find the infinum and 0 is the smallest value that m can take. Thus we now have enough information to find b_s:

$$b_s = [LUB - GLB]\left(\sum_{m=0}^{N}\Psi_{s,m}(k')\right) = \beta_s + \beta_0 + \sum_{l=1}^{N}\epsilon_l + \beta_l \tag{21}$$

which if we expand equation (3.46) in terms of c_i we get:

$$k'_{max} = \beta_0 + \sum_{l=1}^{N}\epsilon_l + \beta_l \tag{22}$$

which directly leads to the result stated at the top of this appendix:

$$b_s = \beta_s + k'_{max} \tag{23}$$

Appendix C

Early Design Apertures

Denomination	Aperture Size / μm	Positions	f_{max} / MHz	f_{loc} / MHz	SO?	SO Location / μm	g
EDD1 (Annuli)	Radius Difference 5.0	Outer Radii / μm $\{44.72,\ 63.25,$ $77.46,\ 89.44,\ 100.0\}$	Unk.	Unk.	Unk.	N/A	Unk.
EDD2 (Slit)	Width 4.0 5.0	Centre / μm $\{\pm 74.64,\ \pm 108.38\}$ $\{\pm 88.25,\ \pm 141.78\}$	4.03	5.15	Yes	$\{5.13, 5.74\}$	1.28
EDD3 (Circle)	Diameter 4.0 5.0	r / μm, θ/rad $\{125.1, 140.3\}$, $\{0, \pi\}$ $\{121.7, 106.0\}$, $\{\frac{\pi}{4}[1, 3, 5, 7]\}$	Unk.	Unk.	Unk.	N/A	Unk.

Slit Design Apertures

Denomination	Slit Width / μm	Central Positions / μm	f_{max} / MHz	f_{loc} / MHz	SO?	SO Location / μm	g
SDD1	3.375 3.5 3.75 4.0	$\{-13.625, 13.625\}$ $\{-3.625,\ 3.625\}$ $\{-8.625,\ 8.625\}$ $\{-18.25,\ 18.25\}$	0.57	0.93	Yes	$\{22.9, 26.3\}$	1.63
SDD2	3.5	$\{-3.625,\ 3.625\}$	0.15	0.24	Yes	$\{64.3, 67.6\}$	1.6
SDD3	4.0	$\{-18.25,\ 18.25\}$	0.57	1.34	Yes	$\{56.2, 58.6\}$	2.35
IDD1	5.375	$\{-7.375,\ 0.0,\ 7.5\}$	0.28	1.22	Yes	$\{81.3, 83.7\}$	4.36
IDD2	2.625 5.375	$\{0.0\}$ $\{-7.375,\ 7.5\}$	0.28	0.28	No	{N/A, N/A}	1
IDD3	2.625 5.375	$\{-7.375,\ 7.5\}$ $\{0.0\}$	0.24	0.58	Yes	$\{13.0, 18.4\}$	2.41
IDD4	2.625	$\{-7.375,\ 0.0,\ 7.5\}$	0.24	0.66	Yes	$\{81.0, 85.7\}$	2.75

Bibliography

[1] G Toraldo Di Francia. Super-gain antennas and optical resolving power. *Il Nuovo Cimento (1943-1954)*, 9(3):426–438, 1952.

[2] Robin S Matoza and Diana C Roman. One hundred years of advances in volcano seismology and acoustics. *Bulletin of Volcanology*, 84(9):86, 2022.

[3] Lisa Taylor and David Claringbold. Acoustics of the sydney opera house concert hall. In *Proceedings of the International Congress on Acoustics, Sydney, NSW, Australia*, pages 23–27, 2010.

[4] Mazharuddin Mohammed, Anne S Verhulst, Devin Verreck, Maarten L Van de Put, Wim Magnus, Bart Sorée, and Guido Groeseneken. Phonon-assisted tunneling in direct-bandgap semiconductors. *Journal of Applied Physics*, 125(1), 2019.

[5] Shoji Yamamoto and Takashi Inoue. Magnon confinement on the two-dimensional penrose lattice: Perpendicular-space analysis of the dynamic structure factor. *Crystals*, 14(8):702, 2024.

[6] H Peter Myers. *Introductory solid state physics.* CRC press, 1997.

[7] M Giehler, T Ruf, M Cardona, and KH Ploog. Standing acoustic waves in gaas/alas mirror-plane superlattices and cavity structures studied by raman spectroscopy. *Physica B: Condensed Matter*, 263:489–491, 1999.

[8] Gerard McCaul, Peisong Peng, Monica Ortiz Martinez, Dustin R Lindberg, Di-

yar Talbayev, and Denys I Bondar. Superoscillations deliver superspectroscopy. *Physical Review Letters*, 131(15):153803, 2023.

[9] Michael Berry, Nikolay Zheludev, Yakir Aharonov, Fabrizio Colombo, Irene Sabadini, Daniele C Struppa, Jeff Tollaksen, Edward TF Rogers, Fei Qin, Minghui Hong, et al. Roadmap on superoscillations. *Journal of Optics*, 21(5):053002, 2019.

[10] Y Aharonov, S Popescu, and D Rohrlich. How can an infra-red photon behave as a gamma ray. *Tel-Aviv University Preprint TAUP*, pages 1847–1890, 1990.

[11] MV Berry and MR Dennis. Natural superoscillations in monochromatic waves in d dimensions. *Journal of Physics A: Mathematical and Theoretical*, 42(2):022003, 2008.

[12] Gang Chen, Zhong-Quan Wen, and Cheng-Wei Qiu. Superoscillation: from physics to optical applications. *Light: Science & Applications*, 8(1):56, 2019.

[13] DG Baranov, AP Vinogradov, and AA Lisyansky. Non-resonant excitation of a two-level atom driven by a superoscillating field. *arXiv preprint arXiv:1312.6020*, 2013.

[14] Andrea Addazi and Qingyu Gan. Superoscillations in high energy physics and gravity. *The European Physical Journal C*, 84(6):644, 2024.

[15] Kun Huang, Huapeng Ye, Jinghua Teng, Swee Ping Yeo, Boris Luk'yanchuk, and Cheng-Wei Qiu. Optimization-free superoscillatory lens using phase and amplitude masks. *Laser & Photonics Reviews*, 8(1):152–157, 2014.

[16] Edward TF Rogers, Jari Lindberg, Tapashree Roy, Salvatore Savo, John E Chad, Mark R Dennis, and Nikolay I Zheludev. A super-oscillatory lens optical microscope for subwavelength imaging. *Nature materials*, 11(5):432–435, 2012.

[17] Zhu Li, Tao Zhang, Yanqin Wang, Weijie Kong, Jian Zhang, Yijia Huang,

Changtao Wang, Xiong Li, Mingbo Pu, and Xiangang Luo. Achromatic broadband super-resolution imaging by super-oscillatory metasurface. *Laser & Photonics Reviews*, 12(10):1800064, 2018.

[18] Alex MH Wong and George V Eleftheriades. An optical super-microscope for far-field, real-time imaging beyond the diffraction limit. *Scientific reports*, 3(1):1715, 2013.

[19] Katrine S Rogers and Edward TF Rogers. Realising superoscillations: A review of mathematical tools and their application. *Journal of Physics: Photonics*, 2(4):042004, 2020.

[20] Yakir Aharonov, Fabrizio Colombo, Irene Sabadini, Tomer Shushi, Daniele C Struppa, and Jeff Tollaksen. A new method to generate superoscillating functions and supershifts. *Proceedings of the Royal Society A*, 477(2249):20210020, 2021.

[21] J. P. (James Philip) Wolfe. *Imaging phonons : acoustic wave propagation in solids / James P. Wolfe.* Cambridge University Press, Cambridge, 1998.

[22] Yuri A Melnikov and Max Y Melnikov. *Green's functions: construction and applications*, volume 42. Walter de Gruyter, 2012.

[23] Ibtisam F Al Maaitah. Sound velocity, mechanical properties, and phonon frequencies of gaas semiconductor material under the effect of temperature. *MRS Advances*, 7(31):929–932, 2022.

[24] Thomas Konrad and Filippus S Roux. Superoscillations: a scale physics perspective. *Journal of Physics A: Mathematical and Theoretical*, 52(46):465202, 2019.

[25] Eric W Weisstein. Uniform convergence. *https://mathworld. wolfram. com/*, 2005.

[26] Weisstein, Eric W. "Convolution." From MathWorld–A Wolfram Web Resource. https://mathworld.wolfram.com/Convolution.html.

[27] Y Ben Ezra, Boris I Lembrikov, Moshe Schwartz, Segev Zarkovsky, and S Radhakrishnan. Applications of wavelet transforms to the analysis of superoscillations. *Wavelet theory and its applications*, 195, 2018.

[28] Part of "A Pragmatic Introduction to Signal Processing", created and maintained by Prof. Tom O'Haver , Department of Chemistry and Biochemistry, The University of Maryland at College Park. https://www.grace.umd.edu/ toh/spectrum/Deconvolution.html.

[29] Eric W Weisstein. Nyquist frequency. *From MathWorld—A Wolfram Web Resource*, 2022.